Dissertations in Forestry and Natural Sciences

RAHUL YADAV

NEURAL NETWORK AND BAYESIAN INVERSION METHODS FOR INDUSTRIAL PROCESS IMAGING USING MICROWAVE TOMOGRAPHY

Rahul Yadav

NEURAL NETWORK AND BAYESIAN INVERSION METHODS FOR INDUSTRIAL PROCESS IMAGING USING MICROWAVE TOMOGRAPHY

ACADEMIC DISSERTATION

To be presented by the permission of the Faculty of Science and Forestry for public examination in the Auditorium SN200 in Snellmania Building at the University of Eastern Finland, Kuopio, on December 21st, 2022, at 12 o'clock.

Author's address: University of Eastern Finland
                     Department of Applied Physics
                     P.O. Box 1627
                     70211 KUOPIO
                     FINLAND
                     email: rahuly@uef.fi

Supervisors: Docent Timo Lähivaara
                     University of Eastern Finland
                     Department of Applied Physics
                     P.O. Box 1627
                     70211 KUOPIO
                     FINLAND
                     email: timo.lahivaara@uef.fi

                     Professor Marko Vauhkonen
                     University of Eastern Finland
                     Department of Applied Physics
                     P.O. Box 1627
                     70211 KUOPIO
                     FINLAND
                     email: marko.vauhkonen@uef.fi

                     Dr. Guido Link
                     Karlsruhe Institute of Technology
                     Institute for Pulsed Power and Microwave Technology
                     Hermann von Helmholtz Square 1
                     76344 Eggenstein-Leopoldshafen, KARLSRUHE
                     GERMANY
                     email: guido.link@kit.edu

Reviewers: Professor Xudong Chen
                     National University of Singapore
                     Department of Electrical and Computer Engineering
                     SINGAPORE 117583
                     SINGAPORE
                     email: elechenx@nus.edu.sg

                     Associate Professor Puyan Mojabi
                     University of Manitoba
                     Department of Electrical and Computer Engineering
                     Winnipeg, MANITOBA, R3T 5V6
                     CANADA
                     email: Puyan.Mojabi@UManitoba.ca

Opponent: Professor Uwe Hampel
                     Helmholtz-Zentrum Dresden-Rossendorf
                     Institute of Fluid Dynamics
                     01328 DRESDEN
                     GERMANY
                     email: u.hampel@hzdr.de

ABSTRACT

Microwave imaging or tomography (MWT) has profound applications in through-wall imaging, ultra-wideband ground-penetrating radar, biomedical imaging, and industrial process imaging. It is due to the relatively high penetration depth of microwave radiation and its non-ionizing properties. This thesis discusses industrial process imaging with a focus on developing fast and efficient reconstruction schemes. In industrial process imaging, an array of microwave sensors with a low number of sensors is a preferred choice as it supports fast data acquisition. In such a scenario, the inverse problems related to MWT become severely ill-posed. Therefore, image reconstruction in MWT in such situations becomes challenging.

In this work, the inversion technique based on neural network methodology for real-time parameter estimation in MWT for its application in the industrial drying system is studied. The imaging modality is applied to estimate the moisture content distribution in a porous material such as polymer foam. For database generation, moisture distribution is realized using a parametric model derived from the experimentally available dielectric characterization data of the polymer foam. Then, for each moisture realization corresponding scattered fields are calculated using the two-dimensional method of moments based forward electromagnetic scattering model. The methodology is tested with numerical and experimental data under static conditions from the developed MWT prototype system. Results show that the neural network strategy gives good estimation accuracy and can be a potential candidate towards industrial process imaging with MWT.

In addition, inversion schemes based on the statistical inversion framework using sample-based prior for the joint parameter estimation of the real and imaginary parts of the dielectric constant are developed and tested. Secondly, a structural prior model based on the diffraction tomography algorithm is also developed. The structural prior model improves the accuracy of the statistical inversion framework under different pragmatic moisture distribution scenarios. Developed methods are evaluated with numerical experiments and with the real data from the developed MWT experimental sensor prototype.

ACKNOWLEDGEMENTS

Finally, I owe my deepest gratitude to my beloved wife Soumya for her unconditional love and selfless support over the years. I am lucky to have you in my life.

Kuopio, December 21, 2022

Rahul Yadav

LIST OF PUBLICATIONS

This thesis consists of the present review of the author's work in the field of microwave imaging and the following selection of the author's publications:

I R. Yadav, A. Omrani, G. Link, M. Vauhkonen and T. Lähivaara, "Microwave Tomography Using Neural Networks for Its Application in an Industrial Microwave Drying System", *Sensors 2021*, 21, 6919.

II R. Yadav, A. Omrani, G. Link, M. Vauhkonen and T. Lähivaara, "Correlated Sample-based Prior in Bayesian Inversion Framework for Microwave Tomography," in *IEEE Transactions on Antennas and Propagation*, July 2022, vol. 70, no. 7, pp. 5860-5872.

III A. Omrani, R.Yadav, G. Link, T. Lähivaara, M. Vauhkonen, and J. Jelonnek, "Multistatic Uniform Diffraction Tomography Derived Structural-Prior in Bayesian Inversion Framework for Microwave Tomography," *IEEE Transactions in Computational Imaging,* 2022, vol. 8, pp. 986-995.

Throughout the overview, these papers will be referred to by Roman numerals. Articles **I** and **II** are open-access articles and Article **III** has been reproduced with permission from IEEE, 2022.

AUTHOR'S CONTRIBUTION

The publications selected in this dissertation are results of joint work with the co-author, Adel Omrani, and the supervisors. The MWT measurement system was designed by the co-author at the Karlsruhe Institute of Technology and all the measurements reported in this thesis were done jointly. In the publications **I** and **II**, the author developed the numerical algorithms and performed the computations of the simulation studies, tested the developed algorithms with the experimental data, and prepared the manuscript with the co-authors. In the publication **III**, the author wrote the manuscript together with the co-authors and contributed to deriving the structural prior model for the Bayesian inversion framework using the multistatic uniform diffraction tomography algorithm. In addition, the author computed the results of the Bayesian inversion with simulated and experimental data.

TABLE OF CONTENTS

1 Introduction

Microwave tomography (MWT) is a form of imaging technique in which one aims to determine the dielectric properties or characterize an unknown object through electromagnetic wave-field measurements [1, 2]. Due to relatively high penetration depth of microwave radiation and its non-ionizing nature, it is widely applied in areas of through-wall imaging [3, 4], ultra wideband ground penetrating radar (GPR) [5, 6], biomedical imaging [7, 8], and industrial process tomography [9–12]. In MWT, the measurement procedure involves illuminating the target with electromagnetic waves (with an operating frequency in the range of 300 MHz to 300 GHz) and collecting the electromagnetic fields for each such illumination. The presence of inhomogeneities in the dielectric properties of the object affects the propagation patterns of the microwave signal by altering its amplitude, phase or polarization. Subsequently, using the electric/magnetic field data and related reconstruction technique the object's shape, location, and material properties (permittivity, conductivity) can be estimated.

Reconstruction in MWT can be addressed by several inversion methods depending on the imaging object and measurement configuration. Loosely, the inversion methods are categorized into qualitative and quantitative reconstruction methods. The mainstay of both the reconstruction techniques depends on the physical model of the electromagnetic (EM) wave-phenomena. The EM wave phenomena are governed by a set of equations known as Maxwell's equations [13,14].

Quantitative methods are aimed at retrieving the shape and location of the scatterer (or inhomogeneities) inside the imaging domain through a linear approximation of the electromagnetic wave-propagation model such as Born [15, 16] or Rytov [17] approximation. Some examples of the qualitative methods are the linear sampling method [18,19], diffraction tomography [20,21], and time-reversal [22–24]. On the other hand, if the values of the electrical properties of the scatterer are desired then quantitative methods with an *exact* EM scattering model are the preferred choice. In these methods, the MWT problem is cast into an optimization problem over parameters representing the unknown electrical properties which are to be estimated. The reason is that the MWT problem is ill-posed in the sense of Hadamard [25–28]. Therefore, solution to the problem is not guaranteed to be unique to the acquired measurement data. The ill-posedness can be treated by employing different regularization techniques in the optimization framework. Some examples of these reconstruction techniques include distorted Born iterative method [29], contrast source inversion method [30], and subspace based optimization method [31] or deep-learning based techniques [32, 33]. The general implementation of the optimization based methods in two-dimensional (2-D) and three-dimensional (3-D) cases of MWT can be traced from [34,35].

Microwave tomography for industrial process imaging has different requirements from that for medical imaging. The use of MWT in industrial process imaging and its applications is detailed in [10]. In addition to spatial resolution, high temporal resolution and/or real-time imaging is also imperative. Some examples of the industrial applications of MWT include imaging of solid or granule flows in a

Figure 1.1: External view of the HEPHAISTOS microwave oven system. Main modules of the oven that contains high power microwave waveguide antenna are represented by numbers tags 1, 2, and 3. Tag 4 is the conveyor belt used for continuous processing of material. Tag 5 represents the microwave filter which is used for blocking leakage power. Picture courtesy of Weiss Technik Gmbh, Germany.

pipeline, multi-phase flow imaging [36]. This thesis concerns application of MWT in industrial imaging in specific to determining process parameters (such as moisture content) connected with microwave heating application which is described next.

1.1 PROCESS IMAGING FOR MICROWAVE HEATING TECHNOLOGY

Microwave heating is a process of heating an object having moisture with high-frequency EM energy. The heat inside the object is produced due to a complex thermodynamic process post the interaction of EM energy with the object. Any industrial microwave heating system consists of at least one microwave power source (magnetron), waveguide antenna to couple power, microwave cavity where the sample is processed, and a control system. The microwave power P absorbed in an object of volume V due to an electric field of strength E is given by [37]

$$P = \frac{1}{2}\omega\epsilon_0\epsilon_r'' |E|^2 V, \tag{1.1}$$

where ω is the angular frequency, ϵ_0 is the free space permittivity, and ϵ_r'' is the relative dielectric loss of the object that governs the heating behaviour.

For the large scale batch or continuous processing at an industrial scale, the cavity has distributed sources and its length is made much larger than the wavelength of the microwaves used. One such technology for an industrial scale heating operations, is HEPHAISTOS (short for high electromagnetic power heated automated injected structure oven system), as shown in Figure 1.1 [38–40]. The system has 3 modules and is characterized by hexagonal geometry [41]. Each module is equipped with 6 magnetrons delivering a total power of 12 kW at 2.45 GHz. In addition, it is equipped with a conveyor belt for continuous processing. Applications of this microwave heating technology are in the areas of drying porous and non-porous

materials, sintering of ceramics and curing of carbon fibers. With this unique hexagonal design for the cavity, the HEPHAISTOS is able to cater to a homogeneous EM field distribution. Although a HEPHAISTOS microwave oven provides a rather homogeneous EM field distribution, the resulting temperature distribution is not necessarily homogeneous while processing the material. This is due to the dielectric and thermal properties of the material and standing waves within the cavity. As a consequence, the microwave heating is not always uniform thereby forming several spatially distributed hot spots and cold spots inside the object.

Generally, in this system, feedback control allows the manipulation of the temperature distribution in the material to prevent over-heating and thermal-runaway situation [42]. However, temperature based feedback control (using infrared temperature sensors) may not provide sufficient and stable control in drying applications as the loss factor of the material is also dependent on moisture content [43] which may result in uneven levelling and undesired moisture levels at the output. In drying applications, the goal is generally to maintain a stable product output moisture level. More so, in cases of non-uniform moisture distribution, the situation of uneven drying may aggravate [44]. The infrared temperature sensors integrated with the microwave heating systems are capable of giving information about the temperature only on the surface of the material. That is not sufficient to provide the efficient control of microwave sources and therefore the process efficiency can be improved by the use of the volumetric moisture distribution as measured and controlled variable in the intelligent controller design [45, 46].

The genesis of controlling the drying process with respect to volumetric spatial moisture distribution stems from the TOMOCON project [47]. In this project, integration of microwave tomography imaging modality with HEPHAISTOS was proposed for the estimation of the moisture content in a polymer foam with large cross-section size and infinite length. Based on the estimated spatial moisture information in the foam from MWT, the control unit can tune the power of the distributed microwave sources and pulse duration and achieve the desired uniform moisture level. Moisture measurement systems explicitly based on microwave radiation have been utilized for the determination of moisture content in a sample during in-situ or ex-situ measurements [48–54]. However, the techniques reported are limited to providing small sample sizes only. Therefore, the development of the MWT sensor array system with a low number of antennas and relevant reconstruction techniques for estimating the spatial moisture variation (in terms of dielectric constant) are needed. From the inverse problems point of view, the present problem is severely ill-posed and challenging due to the limited independent data and the large cross-section size of the object (under-determined problem).

In this thesis, the focus is on the development of reconstruction schemes for MWT to accurately estimate the moisture content distribution in a polymer foam. For the studied microwave drying system employing a conveyor belt and large sample size, the speed by which the moisture distribution information will be available from the MWT is a challenge. Being a non-linear problem, image reconstruction in the MWT is a time-consuming task since it requires solving the forward model multiple times. The popular choices of such iterative inversion algorithms applied in microwave tomography are, for example, Levenberg-Marquardt [34], contrast source inversion [55], and subspace-based optimization method [56]. However, due to the evaluation of the forward model multiple times, these methods may fail to provide estimates for real-time for online control [57, 58]. To achieve this goal, we have developed a reconstruction method relying on a data-driven approach such as neural

network following the feasibility study reported in [59]. Recent developments in the use of neural networks for solving general microwave imaging problem are detailed in [60–67].

Although, neural network framework is fast in providing reconstruction, any changes for example, in (i) the size of the imaging domain, (ii) the roughness of the top surface or high randomness (iii) possible values appearing in real cases outside the simulated range of values of dielectric constant may lead to erroneous reconstruction. Therefore, in this thesis, as an alternative, the feasibility of the Bayesian inversion framework is also studied. Under this framework, to obtain accurate reconstructions for various moisture scenarios, correlated prior model and structural prior model are proposed, respectively. Most parts of this thesis consist of a summary of the results from the developed methods published in different journals. The main contents of the reported publications are described next.

Contents of this thesis

The thesis consists of three publications and their contents are as follows.

1. In the publication **I**, neural network based reconstruction framework was tested on the experimental data from the MWT system. The key feature of the publication **I** is the parametric modelling of moisture distribution using the experimentally available dielectric characterization data of the polymer foam. Using the parametric model, different moisture distribution scenarios were generated. Then, for each moisture realization the corresponding scattered field was calculated using 2-D method of moment based forward electromagnetic scattering model. In this way, a numerical dataset was built for training the neural network.

2. In the publication **II**, a statistical inversion framework was applied to estimate the spatial moisture content accurately especially the imaginary part of the dielectric constant which governs the heating behaviour of the material. Towards this, a correlated sample-based prior model was presented to incorporate the correlation of the real part with the imaginary part of the dielectric constant.

3. A coupled reconstruction scheme based on combining the qualitative and quantitative Bayesian inversion framework was also developed and reported in the publication **III**. In this work, the prior information was modified using high-resolution complementary structural information on the imaging domain given by the qualitative approach multi-static uniform diffraction tomography (MUDT) utilizing broadband frequency-domain data.

This thesis is organized as follows: Chapter 2 describes the electromagnetic scattering and inverse problem of microwave tomography. In Chapter 3, neural network based framework and parametric modelling for moisture distribution is described and the results of the approach are discussed. In Chapter 4, an overview of the Bayesian inversion framework is described and correlated prior model results are presented. Finally, Chapter 5 gives the discussion about the results and final conclusions.

2 Fundamentals of electromagnetic scattering

In this chapter, the fundamental equations of electromagnetic field theory are sum-
marised. Using the fundamental laws, differential and integral equations that pro-
vide the basis for the electromagnetic scattering are derived. Thereafter, a distinction
between the forward problem and inverse problem is given and the MWT imaging
problem addressed in this thesis is briefly introduced.

2.1 GOVERNING EQUATIONS

The theoretical background of electromagnetic radiation and scattering phenom-
ena are based on the mathematical equations proposed by Maxwell in 1873. These
equations are coupled equations involving interrelation between the electric and
magnetic fields. Assuming time-harmonic representation of $e^{+j\omega t}$ where ω is the
angular frequncy, t is time, and $j = \sqrt{-1}$, the Maxwell's equations are expressed
as [14]

$$\nabla \times \vec{E} = -j\omega\mu\vec{H} \qquad \text{Faraday's law of induction} \qquad (2.1)$$

$$\nabla \times \vec{H} = j\omega\epsilon\vec{E} + \vec{J}_s \qquad \text{Ampere's circuital law} \qquad (2.2)$$

$$\nabla \cdot (\epsilon\vec{E}) = \rho_s \qquad \text{Gauss's Law} \qquad (2.3)$$

$$\nabla \cdot (\mu\vec{H}) = 0. \qquad \text{Gauss's law for magnetism} \qquad (2.4)$$

In Equations (2.1) - (2.4), the corresponding vector fields are

$$\vec{E} = \text{electric field in V/m}$$

$$\vec{H} = \text{magnetic field in A/m}$$

$$\vec{J}_s = \text{current density in A/m}^2$$

and the scalar charge ρ_s is the electric charge density in C/m^3. More precisely,
the electric and magnetic field vectors are the complex-valued phasors represent-
ing magnitude and phasor angle of the time-harmonic fields. Note that the term
J_s may represent the electromagnetic sources, for example, transmitting antenna.
The mathematical operators $\nabla\cdot$ and $\nabla\times$ are the divergence and curl operations,
respectively.

The parameters ϵ and μ are the complex dielectric constant/permittivity (F/m)
and permeability (H/m), respectively. For most materials and the material consid-
ered in this work, the permeability μ is equal to free space value. In free space, the
dielectric constant is $\epsilon_0 = 8.845 \times 10^{-12}$ F/m and the permeability is $\mu_0 = 4\pi \times 10^{-7}$
H/m. Generally, the complex quantity ϵ is normalised with respect to free space
dielectric constant term, termed as relative dielectric constant ϵ_r, and given as

$$\epsilon_r = \frac{\epsilon}{\epsilon_0} = \epsilon'_r - j\epsilon''_r. \qquad (2.5)$$

This is a dimensionless quantity. Similar normalisation is applicable to the perme-
ability term which is termed here as μ_r. In general, the constitutive parameters
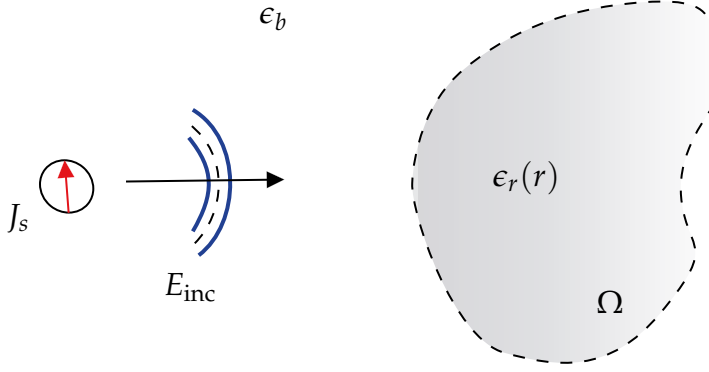
Figure 2.1: A current source radiating in the vicinity of a general inhomogeneity.

ϵ_r and μ_r of a medium can be a function of position (homogeneous or inhomogeneous medium), applied electric field (linear or non-linear medium) or may vary as a function of frequency (dispersive or non-dispersive medium) [14].

By combining Equations (2.1) and (2.2) and eliminating the H-fields, the vector Helmholtz equation

$$\nabla \times \left(\frac{1}{\mu_r} \nabla \times \vec{E} \right) - k_0^2 \epsilon_r \vec{E} = -j\omega\mu_0 \vec{J}_s, \tag{2.6}$$

is obtained. In (2.6), $k_0 = w\sqrt{\mu_0\epsilon_0} = 2\pi/\lambda_0$ is the wavenumber and λ_0 is the wavelength in free space. To derive a unique solution of the vector wave equation, boundary conditions are needed. A detailed account on boundary conditions in electromagnetics can be found in [68, 69]. Using the vector wave equation and the necessary boundary conditions, fields inside and outside a specific domain can be determined.

Consider an object which in this thesis is referred to as target or scatterer is placed in a homogeneous background medium with ϵ_b that is illuminated by a wave produced by the source $\vec{J}_s$, for example, a transmitting antenna. The scheme is shown in Figure 2.1. Due to the inhomogeneities $\epsilon_r(r)$ present inside the object, the electric fields emitted by the source are affected. The affected field which is the field measured in the presence of the object is indicated by $\vec{E}_{total}$. This is different from the field generated by the source in the absence of the object which is known as the incident field and termed here as $\vec{E}_{inc}$. By subtracting the incident field from the total field, the field scattered around the object can be determined. Thus, the scattered field $\vec{E}_{sct}$ can be expressed as

$$\vec{E}_{sct} = \vec{E}_{total} - \vec{E}_{inc}. \tag{2.7}$$

Under the assumption that the background medium has a homogeneous relative permittivty of ϵ_b, the incident field can be expressed as

$$\nabla \times \nabla \times \vec{E}_{inc} - k_0^2 \epsilon_b \vec{E}_{inc} = -j\omega\mu_0 \vec{J}_s. \tag{2.8}$$

Similarly, the total electric field in the presence of non-magnetic scatterer with relative dielectric constant ϵ_r can be solved from

$$\nabla \times \nabla \times \vec{E}_{total} - k_0^2 \epsilon_r(r) \vec{E}_{total} = -j\omega\mu_0 \vec{J}_s. \tag{2.9}$$

Upon substitution of Equation (2.7) in Equation (2.9) and using the incident field expression, the vector wave equation for the scattered electric field can be solved from

$$\nabla \times \nabla \times \vec{E}_{\text{sct}} - k_0^2 \epsilon_b \vec{E}_{\text{sct}} = k_0^2 (\epsilon_r(r) - \epsilon_b) \vec{E}_{\text{total}}. \tag{2.10}$$

From the preceding equation it can interpreted that the scattered field is generated by a secondary current source in the scatter domain that is induced inside it through the influence of primary current source $\vec{J}_s$. This interpretation follows from *volume equivalence principle* for electromagnetic scattering [14]. Solving for the scattered electric field in an unbounded medium requires the field to satisfy at distance r the *Silver-Müller* radiation condition for time-harmonic electromagnetic fields is given as [70]

$$\lim_{|r| \to \infty} \left[\sqrt{\epsilon_0} \vec{E}(r) \times r + |r| \sqrt{\mu_0} \vec{H}(r) \right] = 0. \tag{2.11}$$

2.1.1 Volume integral equation

For an arbitrary electric current distribution J_s placed in free space, it is convenient to evaluate the field by using the concept of dyadic Green's function [71,72] which satisfies

$$\nabla \times \nabla \times \bar{\bar{G}}(r,r') - k_0^2 \bar{\bar{G}}(r,r') = \mathbb{I}\delta(r - r'), \tag{2.12}$$

where $\mathbb{I}$ is a unit dyad that is represented by a unit diagonal matrix. The observation and source points are denoted by the position vectors $r \mapsto (x, y, z)$ and $r' \mapsto (x', y', z')$, respectively. Through the superposition principle, the fields produced by the current distribution $\vec{J}_s$ can be formulated as

$$E(r) = j\omega\mu_0 \int_\Gamma \bar{\bar{G}}(r,r') \cdot \vec{J}_s(r') \, dr', \tag{2.13}$$

for a known domain $\Gamma \subset \mathbb{R}^3$. In the above integral equation, the explicit expression of the dyadic Green's function is given by

$$\bar{\bar{G}} = \left[\bar{\bar{\mathbb{I}}} + \frac{1}{k_0^2} \nabla\nabla \right] G_0(r,r'), \tag{2.14}$$

where $G_0(r,r')$ is the scalar Green's function of free space whose expression is given as

$$G_0(r,r') = \frac{\exp\{-ik_0|r - r'|\}}{4\pi|r - r'|}. \tag{2.15}$$

The dyadic's Green's function can be represented in matrix form as

$$\bar{\bar{G}}(r,r') = \begin{pmatrix} k_0^2 + \frac{\partial^2}{\partial x^2} & \frac{\partial^2}{\partial x \partial y} & \frac{\partial^2}{\partial x \partial z} \\ \frac{\partial^2}{\partial y \partial x} & k_0^2 + \frac{\partial^2}{\partial y^2} & \frac{\partial^2}{\partial y \partial z} \\ \frac{\partial^2}{\partial z \partial x} & \frac{\partial^2}{\partial z \partial y} & k_0^2 + \frac{\partial^2}{\partial z^2} \end{pmatrix} G_0(r,r'). \tag{2.16}$$

Now using the integral representation in Equation (2.13), the vector-wave equation can be expressed in an integral form. Let's consider the scattering scenario shown in Figure 2.2 where a scatterer denoted by Ω_1 with inhomogenous relative
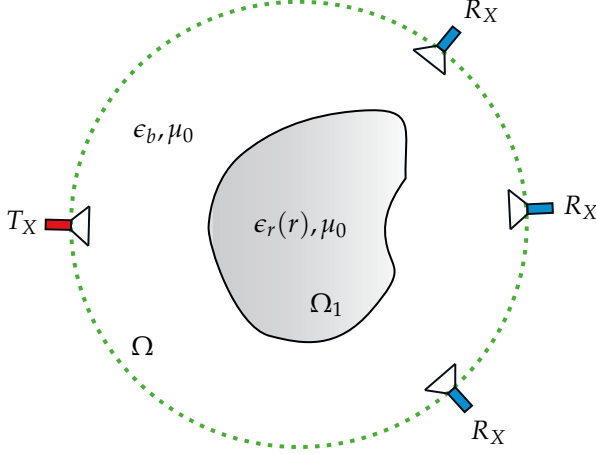
Figure 2.2: Schematic of the scattering problem. The domain Ω_1 embeds the scatterer which is denoted here as $\epsilon_r(r)$ and is placed in homogeneous background medium ϵ_b

.

dielectric constant $\epsilon_r(r)$ is placed in homogeneous domain Ω. The scatterer is illuminated by the transmitter (Tx) and the response field is collected by the receivers (Rx). The scattered electric field for each illumination can be expressed as

$$\vec{E}_{\text{sct}}(r) = k_0^2 \int_{\Omega_1} \bar{\bar{G}}(r,r') \cdot \chi(r')\vec{E}_{\text{total}}(r') \, dr', \quad \forall \, r \in \Omega, \, r' \in \Omega_1 \qquad (2.17)$$

where $\chi(r) = (\epsilon_r(r') - \epsilon_b)$ is the contrast or object function representing the contrast between the background domain and scatterer domain, respectively. This is known as a volume integral equation (VIE) that establishes a relationship between the secondary induced current in the scatter domain and the scattered electric field. Using the above expression, the total field can also be expressed as

$$\vec{E}_{\text{total}}(r) = \vec{E}_{\text{inc}}(r) + k_0^2 \int_{\Omega_1} dr' \bar{\bar{G}}(r,r') \cdot \chi(r')\vec{E}_{\text{total}}(r') \, dr', \, \forall \, r,r' \in \Omega_1 \qquad (2.18)$$

where E_{inc} is known *a priori* since the source is known. Notice that the unknown quantity $\vec{E}_{\text{total}}$ is both inside and outside of the integral that classifies the integral equation as a Fredholm 2nd kind integral equation. In engineering literature, it is also known as the Lippmann-Schwinger equation owing to its origin in quantum mechanics.

2.1.2 Two-dimensional formulation

In some electromagnetic scattering problems if the scatterer geometry is independent of one coordinate axis, the formulation of the problem can be made somewhat simpler. Without the loss of generality let us assume that the scatterer geometry is independent of z. Since there is no variation with respect to z, all field quantities take the z dependence of the excitation. It is usually convenient to decompose the fields into transverse electric (TE) and transverse magnetic (TM) parts. Afterwards, the solutions from TM and TE can be combined to complete the overall solution.

Whether a field is a TE or TM case depends on whether an electric or magnetic field is transverse to a chosen reference. The reference chosen here is the z-axis, and consequently the TE case means that the electric field is transverse to the z-axis, that is, the z component of the electric field is absent, whereas the TM case means that the magnetic field is transverse to the z-axis.

When the geometry is independent of z-coordinates, the scattering problem can be solved by employing free space 2-D scalar Green's function given as [73–75]

$$G_0(r,r') = -\frac{j}{4} H_0^2 (k_0 |r - r'|),$$ (2.19)

where H_0^2 is a Hankel function of second kind and zero order. Therefore, the 2-D dyadic Green's function can be written as

$$\bar{\bar{G}}(r,r') = -\frac{j}{4k_0^2} \begin{pmatrix} k_0^2 + \frac{\partial^2}{\partial x^2} & \frac{\partial^2}{\partial x \partial y} & 0 \\ \frac{\partial^2}{\partial y \partial x} & k_0^2 + \frac{\partial^2}{\partial y^2} & 0 \\ 0 & 0 & k_0^2 \end{pmatrix} H_0^2 (k_0 |r - r'|).$$ (2.20)

Practically, the measurement of different polarizations requires sophisticated experimental systems that can differentiate between measured signal polarizations [76]. Therefore, our attention is focused on studying 2-D TM mode configuration only. In this case, the scattered electric field can be written as [29,77–80]

$$E_{\text{sct}}(r) = k_0^2 \int_{\Omega_1} G_{zz}(r,r') \chi(r') E_{\text{total}_z}(r') \, dr' \quad \forall \, r \in \Omega, r' \in \Omega_1,$$ (2.21)

where G_{zz} is the z-component of the dyadic Green's function. In this work, numerical treatment of the 2-D TM integral equation is provided using the method of moment (MoM). It is apparent from the preceding equation that the scattered field is a non-linear functional of the contrast function because the total field itself is a functional of the object function. In the text to follow, the z notations are dropped.

2.2 FORWARD MODEL FOR MWT

To derive for the forward model, we cast the scattered field equation in the operator form. In operator form, the scattered electric field on the measurement domain Ω can be written as

$$E_{\text{sct}}(r) = \mathcal{G}_o [\chi E_{\text{total}}].$$ (2.22)

On the other hand, the total electric field inside the scattering domain Ω_1 can be represented as

$$E_{\text{total}}(r) = E_{\text{inc}}(r) + \mathcal{G}_{in} [\chi E_{\text{total}}].$$ (2.23)

In the above two equations, the terms $\mathcal{G}_o$ and $\mathcal{G}_{in}$ are the external and internal radiation operators, respectively. Equations (2.22) and (2.23) are also known as data and domain equations, respectively. Note that the domain equation governs the wave interaction within the imaging domain Ω_1 whereas the data equation gives the scattered field on Ω for a given contrast function and total field inside Ω_1. After the discretization using MoM, the domain equation using the expression of data equation can be written as

$$E_{\text{sct}}(r) = \mathcal{G}_o \left[\chi \cdot (I - \mathcal{G}_{in} \cdot \chi)^{-1} E_{\text{inc}} \right],$$ (2.24)

9

where I is a unit matrix.

On a separate note, as mentioned in Chapter 1, the MWT problem is a severely ill-posed inverse problem. A part of the ill-posedness is due to the properties of the forward operator defined in Equation (2.24) [81]. Thus, writing it in a more compact form leads to

$$E_{\mathrm{sct}}(r) = \mathcal{F}(\epsilon_r). \tag{2.25}$$

The mapping $\mathcal{F} : \epsilon_r \longrightarrow E_{\mathrm{sct}}$ is known as a forward operator which maps the dielectric constant to scattered electric field. The scattered field data can come from real experiment or may be simulated data while the right side denotes the approximate physical nature of the problem. Using this forward model, we solve our inverse problem related to MWT that is discussed in the next two chapters.

3 Neural network based approach for parameter estimation

In this chapter, the methodology and results of the neural network approach based on direct learning as reported in the publication I, are reviewed. In the publication I, an MWT configuration with antennas located only on top was chosen as a setup to support fast data acquisition for process tomography. Using ideas from our reported studies [59,82–84], we built a comprehensive synthetic dataset consisting of different moisture content distribution scenarios and the corresponding scattered electric field responses to train the convolutional neural network (CNN).

3.1 DIRECT LEARNING APPROACH FOR MWT

3.1.1 Numerical setup

In Figure 3.1, the 2-D scattering model used for simulating the scattered electric field data is shown. The 2-D configuration was chosen instead of a 3-D model as to decrease the overall computational load for generating the dataset especially when higher frequency and large imaging domain size are considered. In the setup, we considered a two-dimensional foam domain $\Omega_{\text{foam}} = [-15,\ 15] \times [0,\ 7.6]$ cm with inhomogenous relative dielectric constant $\epsilon_r = \epsilon_r' - j\epsilon_r''$ and surrounded by background domain Ω consisting of air with $\epsilon_r = 1 - j0$. The foam was placed on the metal plate (as the conveyor belt in the heating system resides on it) and modelled as a perfect electric conductor (PEC) plane. For this 2-D numerical study, the antenna sensors are modeled as a z-oriented electric line source [14]; $N = 7$ such line sources are placed in a transceiver mode at a distance of $d_0 = 5$ cm from the top
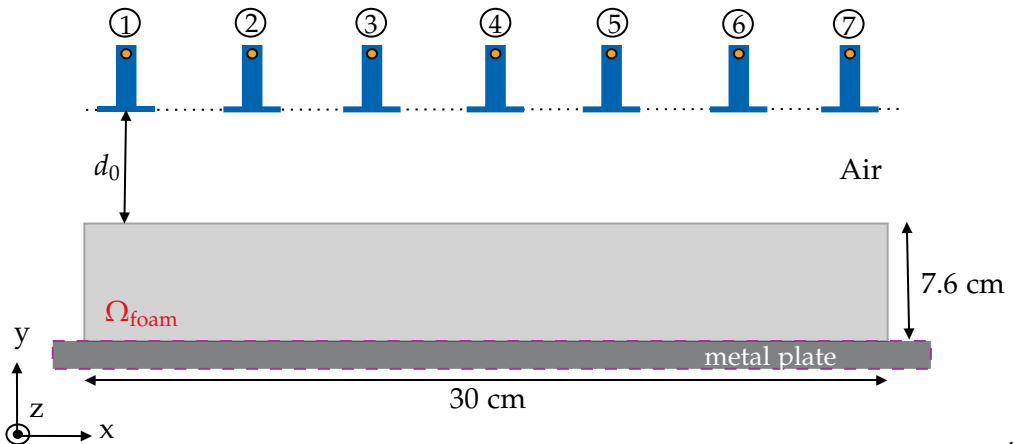
Figure 3.1: Schematic of the MWT setup with antennas denoted by numbers from 1,2,…,7.

surface of the foam. Therefore, the maximum number of measurements that can be acquired is $N \times N$. Note that the rationale behind the choice of the antenna type and the number of antennas for this MWT problem are detailed in [85, 86] and not repeated here to maintain brevity.

The complex-valued scattered electric field under the illumination of TM z-polarized incident field is governed by the scalar volume integral equations (VIEs) given in Equation (2.21). The effects of the conducting plane can be included in the 2-D free space Green's function of the VIEs by the use of half-space Green's function [87]. It is defined using image theory principle [68] where an image source is introduced to account for the reflections from the surface of the conducting plane and thus the conducting plane can be removed during the numerical computation. The image source point (denoted here as x_{im} and y_{im}) must have the same magnitude as the actual source, its phase must be 180 degrees out of phase from the actual source and it must be placed below the conducting plane at a depth $y_{im} = -y$. Such a system configuration does lead to zero tangential electric field along the x-direction [13]. The half-space Green's function includes both the primary contribution $G_T(r, r')$, which is the free space Green's function, and the secondary contribution $G_R(r_{im}, r')$ due to the image source and can be written as

$$\mathsf{G}(r, r') = \mathsf{G}_\mathsf{T}(r, r') + \mathsf{G}_\mathsf{R}(r_{im}, r'). \tag{3.1}$$

Therefore, the scattered electric field above the conducting plane (i.e., upper half-space $y > 0$) is equal to

$$E_{sct}(r) = k_0^2 \int_{\Omega_{foam}} \left[\mathsf{G}_\mathsf{T}(r, r') + \mathsf{G}_\mathsf{R}(r_{im}, r')\right] \chi(r') E(r') \, dr', \; \forall r \in \Omega, \; r' \in \Omega_{foam}. \tag{3.2}$$

Assuming that the foam is discretized to $m \times n$ cells and given the integral equation for the scattered electric field, we resorted to method-of-moments (MoM) with pulse basis and point matching technique for its numerical solution [88].

3.1.2 Parametric model for moisture distribution

The dielectric values in relation to different moisture content are based on the dielectric characterization of the polymer foam in a laboratory environment [89]. From the characterization measurement, a relationship between the wet-basis moisture content M_C and its corresponding real part and the imaginary part of the dielectric value is obtained and given as

$$\theta = \bar{a}_\theta \exp\left(\bar{b}_\theta M_C\right), \tag{3.3}$$

where $\theta = \{\epsilon_r', \epsilon_r''\}$ denotes the material parameters. Numerical values for $\bar{a}_\theta$ and $\bar{b}_\theta$ are given in Table 3.1 where the error bounds for the fitted coefficients are defined by δ_{a_θ} and δ_{b_θ}. The moisture content based on the wet-basis can be expressed as

$$M_C = \frac{W_{t_m} - W_{t_d}}{W_{t_m}} \times 100, \tag{3.4}$$

where W_{t_m} is the weight of the foam sample after adding the water, and W_{t_d} is the weight of the dry sample. Thus, the real part of relative dielectric constant vary in the range of 1.164 - 3.255 and imaginary part vary between 0.017 - 0.276 for wet-basis moisture content from 0% to 90%.

Table 3.1: Material model parameters.

	$\bar{a}_\theta$	δ_{a_θ}	$\bar{b}_\theta$	δ_{b_θ}
ϵ'_r	1.085	0.01591	0.01256	0.00062
ϵ''_r	0.03021	0.0025	0.02249	0.0009

Further, it is assumed that the moisture field variation M in the foam is smooth. To generate such a random field, we utilised an anisotropic covariance structure C with its elements calculated as [90]

$$C_{ij} = \exp\left\{ -\frac{1}{2}\left(\frac{\|x_i - x_j\|^2}{l_x^2} + \frac{\|y_i - y_j\|^2}{l_y^2} \right) \right\}. \tag{3.5}$$

Here, $i,j = 1,\dots,N_n$ and l_x, l_y are the characteristic length components. $N_n = m \times n$ denotes the number of pixels in the x and y directions, respectively. In practice, the characteristic lengths affect the moisture distribution in x and y directions. To generate simulated moisture samples, the uncertainties in the dielectric characterization is also considered, and hence Equation (3.3) is replaced by

$$\theta = a_\theta \exp(b_\theta M), \tag{3.6}$$

where a_θ, b_θ are random variables such that $a_\theta \sim \mathcal{U}(\bar{a}_\theta - \delta_{a_\theta}, \bar{a}_\theta + \delta_{a_\theta})$ and $b_\theta \sim \mathcal{U}(\bar{b}_\theta - \delta_{b_\theta}, \bar{b}_\theta + \delta_{b_\theta})$, where $\mathcal{U}$ denotes the uniform distribution. Numerical values for δ_{a_θ} and δ_{b_θ} are given in Table 3.1. The moisture content distribution in each sample M can be expressed as

$$M = M^* \mathbb{1} + \delta_M L Z, \tag{3.7}$$

where $\mathbb{1}$ is an all-ones vector, L is the lower triangular matrix of the Cholesky factorization of the covariance C, Z is a standard normal random vector, M^* and δ_M are the mean and standard deviation of the moisture content field, respectively. Two realizations of moisture variation for different characteristics lengths are shown in Fig. 3.3.

3.1.3 Choice of frequency and dataset generation

Since the antenna sensors can operate between 8 GHz to 12 GHz, a proper choice of frequency is necessary for estimation. The frequency of the incident field contributes to the degree of non-linearity of the problem (i.e., the higher the frequency of the incident field, the shorter the wavelength that may lead to multiple scattering) [91, 92]. The degree of non-linearity of the inverse scattering problems can be analysed by expanding the inverse term in Equation (2.24) using the Neumann series as

$$[I - \mathcal{G}_{\text{in}}\chi]^{-1} = I + (\mathcal{G}_{\text{in}}\chi) + (\mathcal{G}_{\text{in}}\chi)^2 + \cdots + (\mathcal{G}_{\text{in}}\chi)^k. \tag{3.8}$$

The larger the norm of $\|\mathcal{G}_{\text{in}}\chi\|$, the higher order terms in the series have more influence. This leads to strong non-linearity and consequently to multiple scattering effects. To asses the degree of non-linearity of inverse scattering problem with respect to the frequency of incident field, the behavior of the norm of the factor $\mathcal{G}_{\text{in}}\chi$ is to be evaluated i.e., $\|\mathcal{G}_{\text{in}}\chi\|$. Applying Cauchy-Schwarz's inequality to $\|\mathcal{G}_{\text{in}}\chi\|$ one obtains the upper bound as

$$\|\mathcal{G}_{\text{in}}\chi\| \leq \|\mathcal{G}_{\text{in}}\| \, \|\chi\|. \tag{3.9}$$
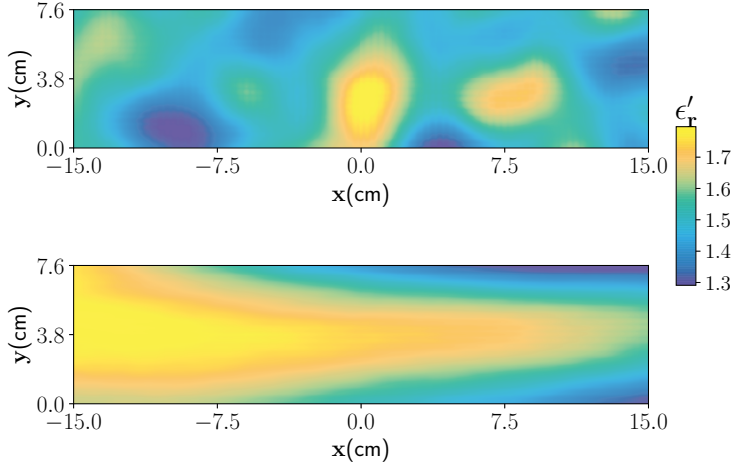
Figure 3.2: Two realisations of the moisture distribution with different characteristic lengths. For top figure ($l_x = 3\,$cm, and $l_y = 3\,$cm) and for bottom figure ($l_x = 30\,$cm, $l_y = 7\,$cm), respectively.

Assuming that χ is fixed in the imaging domain, it can be deduced that the degree of non-linearity of current inverse problem is proportional to $\|\mathcal{G}_{in}\|$. It should be noted that the internal radiation operator is given as [88]

$$
\mathcal{G}_{in} = \begin{cases} \frac{j}{2}\left[\pi k_0 a H_1^2(k_0 a) - 2j\right], & \forall\ m = n \\ \frac{j\pi ka}{2} J_1(k_0 a) H_0^2\left(k\sqrt{(x_m - x_n)^2 + (y_m - y_n)^2}\right), & \forall\ m \neq n \end{cases}
$$

where H_1^2 is the Hankel function of second kind and first order, a is the radius of equivalent circular region having same area of the discretized cell, and J_1 is the Bessel function of the first kind. It can be deduced from the above expression that with an increase in frequency (the factor $k_0 a$ will increase), the behaviour of factor $\|\mathcal{G}_{in}\chi\|$ should be of an increasing function as shown in Figure 3.3. Hence, the non-linearity is proportional to the operating frequency and for this reason, we have chosen 8.3 GHz frequency for inversion (the electric field response in the experimental MWT scenario at 8.3 GHz was found slightly better than at 8 GHz).

For the scattered field computation using the MoM technique, the foam was given a moisture distribution realized using the parametric model discussed in the previous section and it is discretized to $m \times n = 80 \times 20$ cells in x and y directions, respectively. An initial noise-free dataset of 10,000 samples containing complex scattered electric field response and corresponding moisture distribution was then created. Furthermore, five copies of the dataset are created by adding noise between 1% to 3% of the maximum scattered field data to the scattering data. Noise was added following [93] as

$$
E_{sct_{noise}} = E_{sct} + \max(E_{sct})\frac{\mathbb{N}}{\sqrt{2}}(v_1 + jv_2), \tag{3.10}
$$

where $\max(E_{sct})$ is the maximum value of the scattered electric field, $v_1 \sim \mathcal{U}(-1,1)$ and $v_2 \sim \mathcal{U}(-1,1)$ are two real vectors whose elements are sampled from uniform
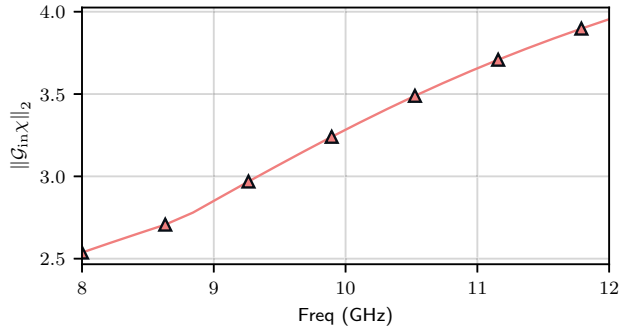
Figure 3.3: Behaviour of $\|\mathcal{G}_{\text{in}}\chi\|$ in the frequency range from 8 GHz to 12 GHz.

distribution. The term $\mathbb{N}$ denotes the noise level and sampled as $\mathbb{N} \sim \mathcal{U}(0.01, 0.03)$. In addition, 2000 samples were generated following the same procedures as a validation dataset. The noise was added to validation dataset similarly as for the training samples.

Furthermore, a test dataset with 1000 samples was generated using denser discretization in MoM computation. A different discretization was chosen to avoid "inverse crime", i.e., the use of the same computational model or same grid settings to generate both training and test datasets. Otherwise, the same grid setting or the computational model may potentially lead to a situation where severe modelling errors are ignored and hence giving a false impression on the accuracy of the estimates [94].

3.1.4 CNN architecture

In the publication **I**, a CNN with mapping $\pounds_{\Theta}^{\dagger} : E_{\text{sct}} \longrightarrow \epsilon_r'$ was trained to map from an input space $E_{\text{sct}} \in \mathbb{C}^{N \times N}$ to $\epsilon_r' \in \mathbb{R}^{\varrho \times 1}$ (vectorized real part of the dielectric constant ϵ_r'). The mapping satisfies the following *pseudo-inverse* property [95]

$$\pounds_{\Theta}^{\dagger}(E_{\text{sct}}) \approx \epsilon_r', \tag{3.11}$$

whenever scattering data is related to the true parameter of interest. Given the *training* data, the learning refers to choosing optimal values for the parameter $\Theta \in \{w, b\}$ where w is the weight and and b is the bias of the CNN architecture. These optimal values are chosen based on a certain loss-functional minimization. Note that the imaginary part of the dielectric constant was not estimated as to reduce the overall computational load of the CNN. Otherwise, the number of parameters to be estimated is doubled and in that scenario the CNN architecture might need to be changed.

The network architecture used in this work is shown in Figure 3.4 and is motivated by the work [59]. The current CNN architecture has five layers. The input layer consists of two channels where the real part (channel 1) and imaginary part (channel 2) of the complex valued scattered electric data, i.e., E_{sct} are given as an input. The convolutional layers $L = 1$ and $L = 2$ have 20 and 30 channels, respectively, with non-linear Rectified Linear Unit (ReLU) activation function. A spatial filter of size 3×3 was chosen for both convolution layers. The fully connected layer $L = 3$
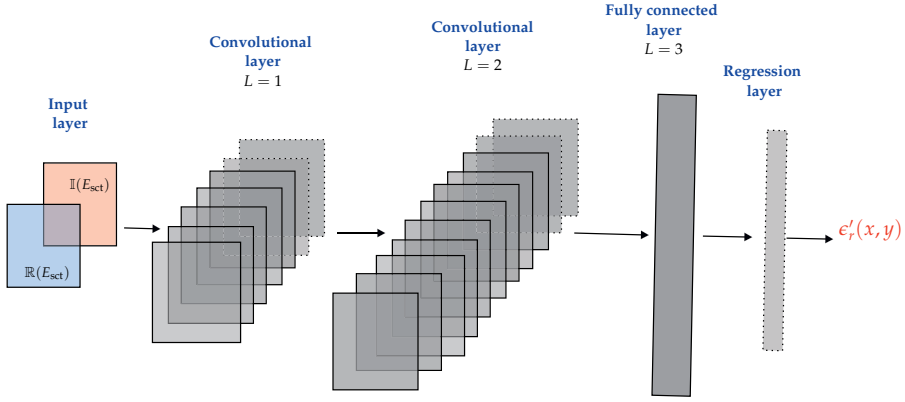
Figure 3.4: A simplified view of the architecture of the convolutional neural network used in this study.

has an output of size 340×1. As for the estimation of $\epsilon'_r(x,y)$, an adequate resolution of the moisture distribution field of around $x \times y = 1\,\text{cm} \times 0.76\,\text{cm}$ is chosen that corresponds to an image with pixels $\varrho = 30 \times 10$. Thus, the output layer has a size of 300×1.

For the network training process, the Adaptive moment estimation (Adam) optimizer [96] was chosen, with the batch size of 150 samples and epoch setting as 2000. The learning rates are set to 1×10^{-4} throughout the training. All the computations were performed in a Python library TensorFlow [97] on a local computer with the configuration of 32 GB access memory, Intel Core(TM) i7-7820HQ central processing unit, and Nvidia Quadro M2200 graphic unit. The training of the network takes about 5 h.

3.2 NUMERICAL EVALUATION OF THE CNN APPROACH

This section presents the numerical results of the publication **I**. For the considered cases, a noise with $\mathbb{N} = 0.03$ is added to the scattered electric field. Estimation accuracy was evaluated by comparing the profile similarity index, denoted here as κ and expressed as

$$\kappa = \frac{\iint_{\Omega_{\text{foam}}} \overline{\epsilon'_{r_{\text{CNN}}}}\, \overline{\epsilon'_{r_{\text{True}}}}\, dxdy}{\sqrt{\iint_{\Omega_{\text{foam}}} (\overline{\epsilon'_{r_{\text{CNN}}}})^2 dxdy}\sqrt{\iint_{\Omega_{\text{foam}}} (\overline{\epsilon'_{r_{\text{True}}}})^2 dxdy}}. \tag{3.12}$$

The term $\overline{\epsilon'_{r_{\text{CNN}}}} = \epsilon'_{r_{\text{CNN}}} - \left\langle \epsilon'_{r_{\text{CNN}}} \right\rangle$, and $\overline{\epsilon'_{r_{\text{True}}}} = \epsilon'_{r_{\text{True}}} - \left\langle \epsilon'_{r_{\text{True}}} \right\rangle$. The operator $\langle \cdot \rangle$ is the mean operator. For the κ, its values vary between 0 and 1. As it gets closer to 1, the estimated profile is closer to the ground truth.

Case 1: Low, and moderate moisture content

As a first case, we considered test samples with low (0–25%), and moderate (25–50%) wet-basis moisture contents. Results of the CNN estimations along with the

16
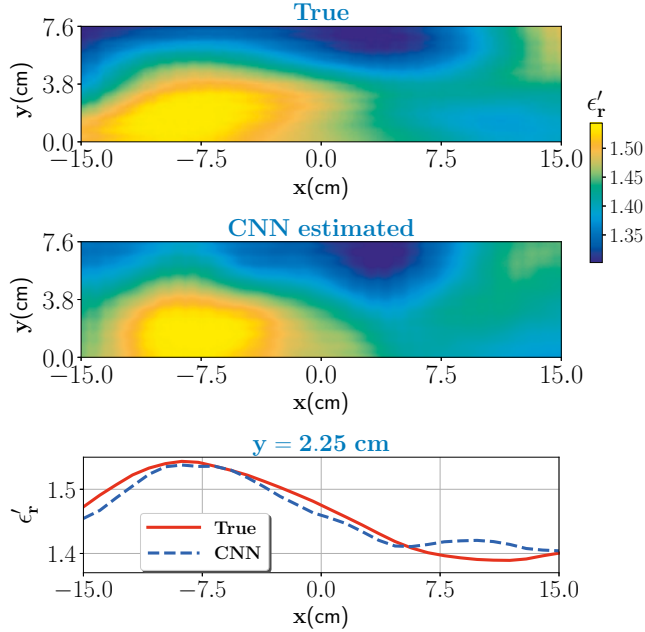
Figure 3.5: Low moisture case: top figure shows the true profile and middle figure is the estimate from the CNN. Bottom figure compares the pixel values for the true and estimated profile at $y = 2.25$ cm data line.

true cases are shown in Figure 3.5 and Figure 3.6. In addition, in the respective cases plotted are the pixel values on data line $y = 2.25$ cm for low moisture case and pixel values on data line $y = 3.8$ cm for moderate moisture. In both cases, the CNN estimated output closely matches the ground truth. The κ values for low and moderate moisture cases are found to be 0.9558 and 0.9331, respectively. For both cases, κ values indicate that estimated profiles are similar to the ground truth. Note that we interpolated the number of pixels in the true profile to correspond with the pixels in the estimated profile to calculate κ.

Case 2: High moisture distribution

It is very likely that the moisture variation at the inlet of the drying operation has high moisture levels. Considering this scenario, two special cases of moisture distribution with moisture variation between 50% to 70% are considered. The true test samples and estimated outputs are shown in Figure 3.7 and Figure 3.8. Pixel values, as similar in the previous case, are compared against the true case and shown in bottom for respective cases. For both cases, the estimated output is close to the ground truth. The κ values are found to 0.923 and 0.883 for the respective cases and values indicate that estimated output is fairly close to the ground truth.

Error estimates

Relative estimation error for the whole test data is shown pixel-wise in Figure 3.9 in the form of a histogram.

Figure 3.6: Moderate moisture case: top figure shows the true profile and middle figure is the estimate from the CNN. Bottom figure compares the pixel values for the true and estimated profile at $y = 3.8$ cm data line.
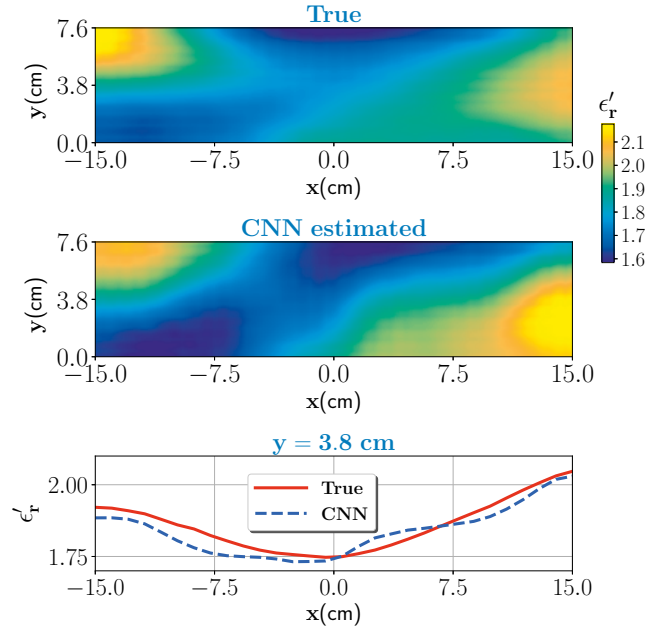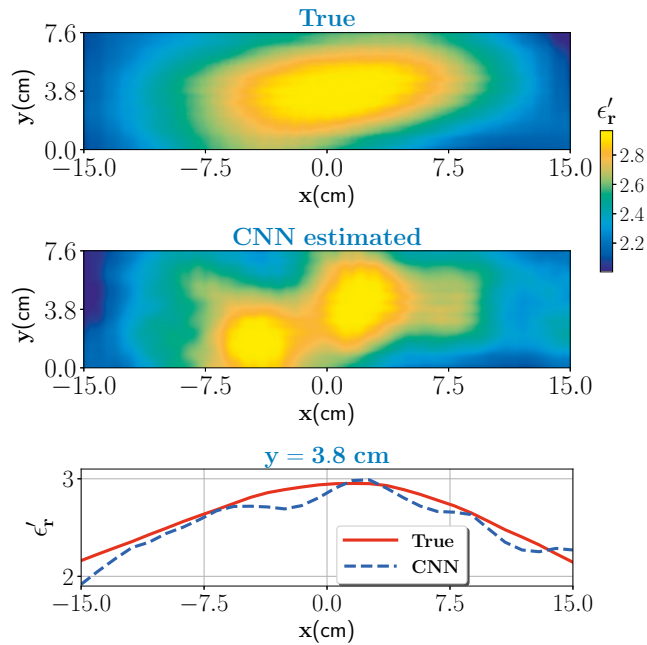

Figure 3.7: High moisture case. Otherwise same caption as in Figure 3.6.
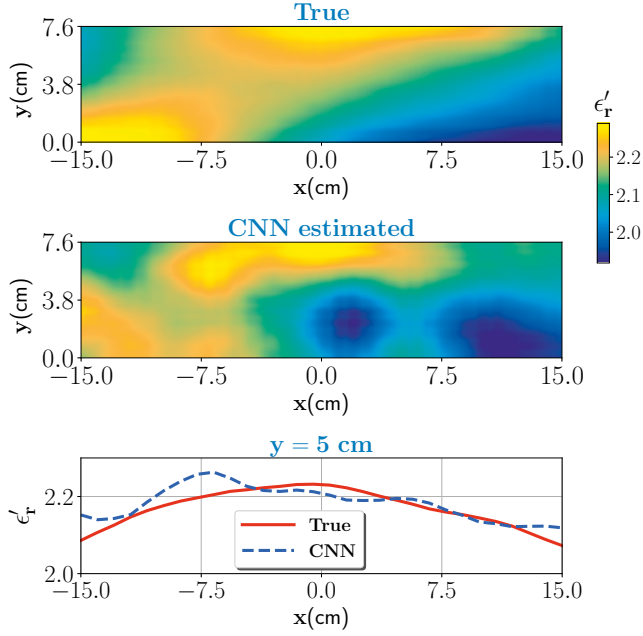
Figure 3.8: Nearly homogeneous high moisture case: same caption except for the bottom figure where pixel values are compared for data line $y = 5\,\text{cm}$.
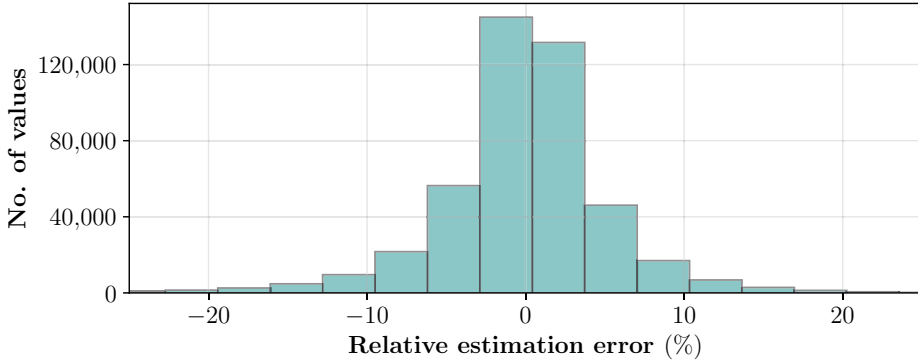
Figure 3.9: Difference between the estimated and true values (relative estimation error) of the real part of the dielectric constant for the total number of 1000 test samples.

3.3 MEASUREMENT SETUP

The MWT experimental prototype consist of seven WR90 open-ended waveguide antennas, placed over the foam of width = 50 cm, height = 7.6 cm, and length = 75 cm. The distance of the antenna to the top surface of the polymer foam is 5 cm, and the center to center distance between two adjacent antennas is 5 cm. Antennas are fixed and placed in free space from −15 cm to 15 cm along the x-axis. The block diagram of the data acquisition scheme and the MWT system are shown in Fig-
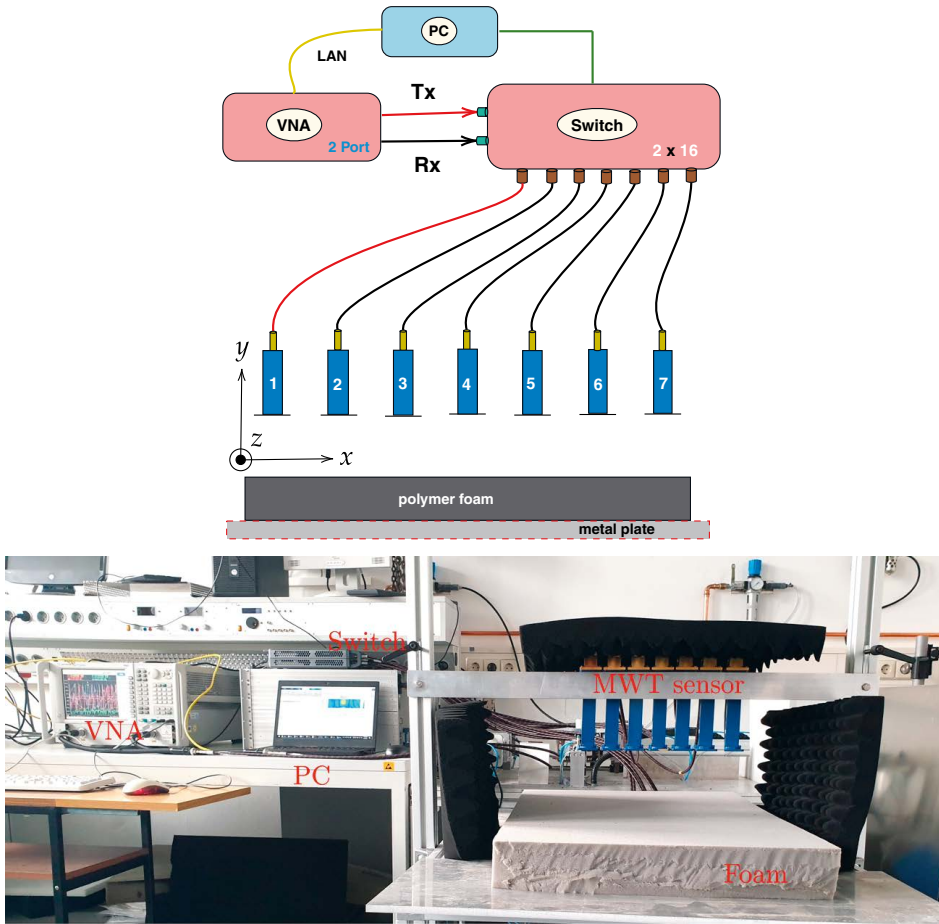
Figure 3.10: Top: data acquisition scheme for the MWT measurement from the sensor array with X-band open waveguide antennas. Bottom: prototype of MWT sensor array used in this study to generate measurement data. This system is developed at Karlsruhe Institute of Technology, Germany.

ure 3.10. The data acquisition process and image reconstruction process (<1 sec) are entirely automated using MATLAB. The measured scattered electric field data are acquired at 8.3 GHz frequency at cross-section of $z = 0$ cm and takes around 20 s. Since the CNN network is trained on electric field data instead of scattering parameter (voltages), calibration scheme in [98] is employed for its conversion. Note that the foam size considered for calibration and later for estimation purposes is the total length of sensor array geometry in this controlled experimental study.

CNN performance

In the publication **I**, two experimental test cases are considered. The first target was a solid PTFE Teflon cylinder with known electrical properties and the second one was the moisture wet-spot case. While the second choice is obvious the rationale for choosing the first target material was to test if the estimated dielectric values by the
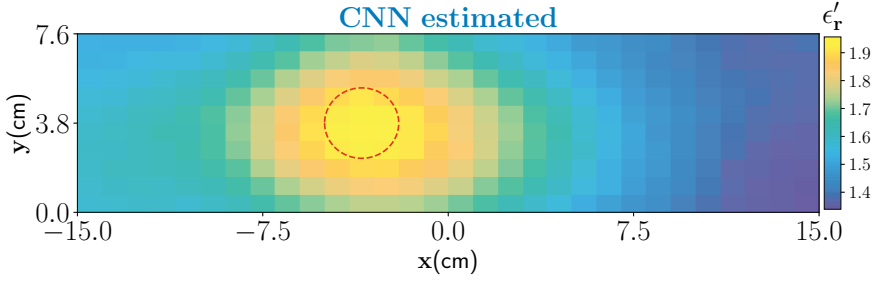
Figure 3.11: CNN estimation of cylindrical Teflon sample placed inside the foam. The true location of the target is marked by red-dashed circle.

CNN are correct as the true value is well in the range of our interest. Moreover, it was also chosen to test the overall generalization capabilities of the trained architecture for identifying targets not seen as a ground truth while its training. The two cases are described as follows.

- *Case 1: PTFE Teflon cylinder.* As a first example, we have considered a PTFE Teflon ($\epsilon'_r \approx 2.1$) material as a benchmark target. The target has a cylindrical shape (diameter of 2.25 cm and length of approximately 20 cm) and is placed inside the foam through an incision on the top surface. An approximate location of the target inside the foam is centered at $(-4.5\,\text{cm}, 3.8\,\text{cm}, 0\,\text{cm})$. Estimated result is shown in Figure 3.11. Result shows that the target dielectric value is satisfactorily estimated by the network but it is slightly overestimated in the shape. The overestimation of the shape is predominately due to the smoothness model used in the training.

- *Case 2: Moisture wet-spot case.* To create the wet-spot moisture target, a spherical piece of foam of diameter 2.5 and with a 43% wet-basis moisture level ($\epsilon_r \approx 1.81 - j0.079$) was chosen. An approximate location of the target inside the foam is centered at $(-3.25\,\text{cm}, 1.85\,\text{cm}, 0\,\text{cm})$. The estimated output from the CNN is shown in Figure 3.12. Estimated result shows that the network can satisfactorily locate the wet-spot which is placed around the bottom of the foam. The estimated real part of the dielectric constant corresponds to the moisture levels between 37% and 39% of the wet-spot.
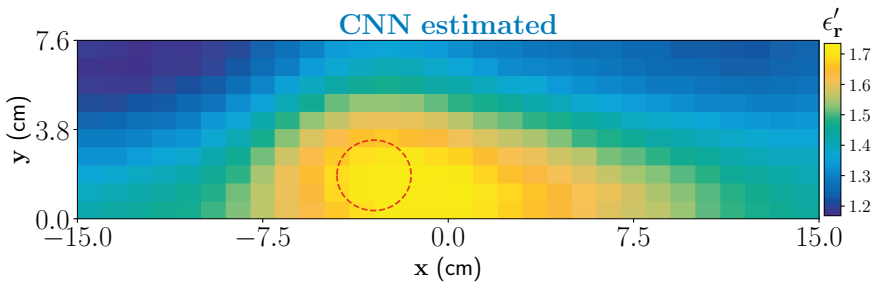
Figure 3.12: CNN estimation of one dominant wet-spot with 43% moisture inside the foam.

4 Bayesian inversion method with correlated sample-based prior and structural prior model

In this chapter, results of the publications **II** and **III** covering Bayesian inversion methodology are presented. The main motivation was to improve the overall estimation quality by exploiting Gaussian smoothness prior model.

4.1 BAYESIAN INVERSION

4.1.1 Construction of the posterior model

Consider an inverse problem of identifying an unknown parameter $\epsilon_r \in \mathbb{C}^{m \times n}$ given noisy measurement data $E_{\text{sct}} \in \mathbb{C}^{N \times N}$ according to the observation model

$$E_{\text{sct}} = \mathcal{F}(\epsilon_r) + \xi, \tag{4.1}$$

where ξ denotes the additive Gaussian measurement noise component. In publications **II** and **III**, the inverse problem was formulated as a real-valued optimization problem. Therefore, the complex quantities are treated separately into real and imaginary parts and concatenated in vector form as

$$E_{\text{sct}} = \begin{pmatrix} \mathscr{R}\{E_{\text{sct}}\} \\ \mathscr{I}\{E_{\text{sct}}\} \end{pmatrix} \in \mathbb{R}^{2S \times 1} \tag{4.2}$$

and,

$$\epsilon_r = \begin{pmatrix} \epsilon_{r'} \\ \epsilon_{r''} \end{pmatrix} \in \mathbb{R}^{2N_n \times 1}. \tag{4.3}$$

In the expressions (4.2) and (4.3), the term $S = N \times N$ is the total number of measurement points and $N_n = m \times n$ total number of unknowns.

In the Bayesian inversion framework, the unknown parameters are treated as random variables, and information about them is expressed in terms of probability densities. Specifically, the inverse problem can be expressed as given the measurement data, the task is to find the conditional probability density $p(\epsilon_r \mid E_{\text{sct}})$ for the unknown ϵ_r. The conditional probability density is constructed using the Bayes' theorem as

$$p(\epsilon_r \mid E_{\text{sct}}) = \frac{p(E_{\text{sct}} \mid \epsilon_r) p(\epsilon_r)}{p(E_{\text{sct}})},$$
$$\propto p(E_{\text{sct}} \mid \epsilon_r) p(\epsilon_r), \tag{4.4}$$

where $p(\epsilon_r \mid E_{\text{sct}})$ is the posterior density, $p(E_{\text{sct}} \mid \epsilon_r)$ is the likelihood density which represents the distribution of the measured data if ϵ_r is known, and $p(\epsilon_r)$ is the prior density which contains the prior information available for unknown ϵ_r. The denominator is the marginal density of the measured data and plays the role of normalization constant. It is often ignored since it requires integration over all possible ϵ_r space.

Furthermore, if the noise is assumed to be additive Gaussian with zero mean and covariance matrix Γ_{ξ}, the likelihood density can be written as

$$p(E_{\text{sct}} \mid \epsilon_r) \propto \exp\left\{-\frac{1}{2}\left\|L_{\xi}(E_{\text{sct}} - \mathscr{F}(\epsilon_r))\right\|^2\right\}, \tag{4.5}$$

where L_{ξ} is the Cholesky factor of the inverse of the noise covariance matrix. As a prior information, it is first assumed that the moisture variation is smooth inside the foam. Such an assumption can be encoded using a Gaussian density with mean η_{ϵ_r} and covariance Γ_{ϵ_r} as

$$p(\epsilon_r) \propto \exp\left\{-\frac{1}{2}\left\|L_{\epsilon_r}(\epsilon_r - \eta_{\epsilon_r})\right\|^2\right\}. \tag{4.6}$$

Here, L_{ϵ_r} is the Cholesky factor of the inverse of the prior covariance matrix Γ_{ϵ_r}. The prior covariance matrix encodes the spatial smoothness knowledge of the unknowns. After multiplying the expressions in (4.5) and (4.6), posterior density is obtained.

The posterior density contains the complete solution of the inverse problem in the Bayesian framework and it has a closed form solution only when an observation model is linear and noise and prior are Gaussian distributed [99]. In case of non-linear/non-Gaussian densities, posterior density can be explored by employing sampling methods such as Markov Chain Monte Carlo technique. Albeit, it is computationally expensive technique for high-dimensional problems. Therefore, point estimates of the posterior density are usually computed and one of the most common point estimates in tomographic imaging problems is the *maximum a posteriori* (MAP) estimate. The MAP estimate can be computed from the posterior as

$$\widehat{\epsilon}_{r_{\text{MAP}}} = \arg\max_{\epsilon_r} p(\epsilon_r \mid E_{\text{sct}}). \tag{4.7}$$

Under the assumption of Gaussian densities for likelihood and prior term, the MAP estimate can be evaluated by an equivalent minimization problem given as

$$\widehat{\epsilon}_{r_{\text{MAP}}} = \arg\min_{\epsilon_r}\left\{\left\|L_{\xi}(E_{\text{sct}} - \mathcal{F}(\epsilon_r))\right\|^2 + \left\|L_{\epsilon_r}(\epsilon_r - \eta_{\epsilon_r})\right\|^2\right\}. \tag{4.8}$$

The expression in (4.8) is a regularized non-linear least-square (LS) problem where the prior norm term acts as a regularization term and it shares close links to generalized Tikhonov regularization [100]. This minimization problem can be formally solved using the gradient-based optimization method such as Gauss-Newton. In the Newton type method the minimum point is found iteratively by linearizing the forward model; resulting in a linear LS solution in each iteration as

$$\epsilon_{r_{\ell+1}} = \epsilon_{r_{\ell}} + \alpha_{\ell}A^{-1}B, \tag{4.9}$$

where,

$$A = \left[J_{\ell}^{\top}\Gamma_{\xi}^{-1}J_{\ell} + \Gamma_{\epsilon_r}^{-1}\right],$$

$$B = \left[J_{\ell}^{\top}\Gamma_{\xi}^{-1}(E_{\text{sct}} - \mathcal{F}(\epsilon_{r_{\ell}})) - \Gamma_{\epsilon_r}^{-1}(\epsilon_{r_{\ell}} - \eta_{\epsilon_r})\right].$$

The term α_{ℓ} is the step length parameter, index ℓ is the iteration number and J_{ℓ} is a Jacobian matrix (its derivation can be found in [34]) which can be decomposed

in real and imaginary parts as

$$J = \begin{pmatrix} \mathscr{R}\{J\} & \mathscr{I}\{J\} \\ -\mathscr{I}\{J\} & \mathscr{R}\{J\} \end{pmatrix} \in \mathbb{R}^{2S \times 2N_n}.$$

The approximate covariance of the posterior density Γ_{post} is given as [99]

$$\Gamma_{\text{post}} = \left[J_\ell^T \Gamma_\xi^{-1} J_\ell + \Gamma_{\epsilon_r}^{-1} \right]^{-1}, \tag{4.10}$$

and it indicates the uncertainty associated with the ill-posedness of the solution.

4.1.2 Noise model

Let us denote the noise standard deviations of the real and imaginary parts of the complex-valued scattered electric field data to be $\sigma_{\mathscr{R}}$ and $\sigma_{\mathscr{I}}$, respectively. Under the assumption that noise between measurement points are independent and not correlated, the noise covariance can be expressed as

$$\Gamma_\xi = \begin{pmatrix} \sigma_{\mathscr{R}}^2 \mathbb{I}_S & \mathbf{0}_S \\ \mathbf{0}_S & \sigma_{\mathscr{I}}^2 \mathbb{I}_S \end{pmatrix} \in \mathbb{R}^{S \times S}, \tag{4.11}$$

where $\mathbb{I}_S$ is an $S \times S$ identity matrix and $\mathbf{0}_S$ is an $S \times S$ zero matrix.

4.1.3 Prior modelling

Since the unknown complex-valued dielectric constant was treated as a real-valued random variable, the Gaussian prior density can be further expressed as [101, 102]

$$\pi\left(\begin{bmatrix} \epsilon_r' \\ \epsilon_r'' \end{bmatrix} \right) \propto \exp\left\{ -\frac{1}{2} \begin{pmatrix} \epsilon_r' - \eta_{\epsilon_r'} \\ \epsilon_r'' - \eta_{\epsilon_r''} \end{pmatrix}^\top \begin{pmatrix} \Gamma_{\epsilon_r'} & \Gamma_{\epsilon_r'\epsilon_r''} \\ \Gamma_{\epsilon_r''\epsilon_r'} & \Gamma_{\epsilon_r''} \end{pmatrix}^{-1} \begin{pmatrix} \epsilon_r' - \eta_{\epsilon_r'} \\ \epsilon_r'' - \eta_{\epsilon_r''} \end{pmatrix} \right\}. \tag{4.12}$$

The terms $\eta_{\epsilon_r'}$ and $\eta_{\epsilon_r''}$ denote the mean values of the real and imaginary parts of the dielectric constant, respectively. The matrices $\Gamma_{\epsilon_r'} \in \mathbb{R}^{N_n \times N_n}$ and $\Gamma_{\epsilon_r''} \in \mathbb{R}^{N_n \times N_n}$ are the marginal covariance matrices of real and imaginary parts of dielectric constant, respectively. $\Gamma_{\epsilon_r'\epsilon_r''} \in \mathbb{R}^{N_n \times N_n}$ and $\Gamma_{\epsilon_r''\epsilon_r'} \in \mathbb{R}^{N_n \times N_n}$ are the cross-covariance matrices which embed the correlation between the real and imaginary parts of the complex dielectric constant parameter.

Uncorrelated real and imaginary parts

If real and imaginary parts of the dielectric constant are treated as statistically un-correlated i.e., $\Gamma_{\epsilon_r'\epsilon_r''} = \Gamma_{\epsilon_r''\epsilon_r'} = 0$, then the prior covariance matrix can be written as

$$\Gamma_{\epsilon_r} = \begin{pmatrix} \Gamma_{\epsilon_r'} & \mathbf{0}_{N_n} \\ \mathbf{0}_{N_n} & \Gamma_{\epsilon_r''} \end{pmatrix} \in \mathbb{R}^{2N_n \times 2N_n}. \tag{4.13}$$

As a prior information, we assumed that moisture field variation inside the foam is smooth and its dielectric values are based on the dielectric characterization data discussed in Section 3.1.2. Recall that such a random field can be generated using

squared-exponential (SE) covariance function defined in Equation (3.5) and denoted as C. Thus, Equation (4.13) can further be expressed as

$$\Gamma_{\epsilon_r} = \begin{pmatrix} \sigma_{\epsilon_r'}^2 C & \mathbf{0}_{N_n} \\ \mathbf{0}_{N_n} & \sigma_{\epsilon_r''}^2 C \end{pmatrix}, \tag{4.14}$$

where $\sigma_{\epsilon_r'}$ and $\sigma_{\epsilon_r''}$ are the standard deviations for the real and imaginary parts of dielectric constant, respectively. These standard deviation values are multiplied with the SE covariance function so to control its overall amplitude variation of the random field.

4.2 SAMPLE-BASED PRIOR MODEL

The assumption of uncorrelated real and imaginary parts in the prior model may result in inaccurate parameter estimates [103,104]. Since the imaginary part governs the heating behaviour, its correct estimation becomes imperative for the present study. Therefore, to achieve accurate MAP estimates, the key is to construct a joint-prior model which favors correlation between the real and imaginary parts.

In [105,106], similar problem is addressed using expectation-maximization (EM) algorithm [107], albeit, it may not be a suitable approach for our high-dimensional problem with a non-linear observation model. On the other hand, joint reconstructions in the deterministic inversion methods have been addressed in (i) [108] where the complex-permittivity in the imaging domain is expressed as a weighted sum of a few pre-selected permittivities, close to the range of the expected values, and permittivity weights are obtained using Gauss-Newton inversion (GNI) algorithm; however the method is mostly valid for practical biomedical applications with linearized inverse scattering model; and (ii) in [109, 110] an approximate ratio is obtained between the real part and imaginary part of the complex permittivity based on the dielectric characterisation of the material(s) under test and this approximate ratio served as the prior information in GNI algorithm with total variation multiplicative regularizer term. Moreover, the results show improvement by adjusting the approximate average ratio. However, in our work, the moisture to dielectric relationship is non-linear thus a single average factor for all moisture points may lead to inaccurate reconstructions.

In the publication **II**, a sample-based prior model was presented to construct the prior covariance structure. When the real and imaginary parts of the dielectric constant are assumed statistically correlated this implies that the cross-covariance terms $\Gamma_{\epsilon_r'\epsilon_r''} \neq 0$ and $\Gamma_{\epsilon_r''\epsilon_r'} \neq 0$. To find cross-variances matrices, dependency between the two random variables should be known. Herein, to establish the correlation between the random variables and to form the prior covariance structure we used sample-based densities.

Assume that $p = p(\epsilon_r)$ is the Gaussian density of a random variable ϵ_r, and that we have a database $\mathbb{X}$ that contains the realizations of ϵ_r as

$$\mathbb{X} = \left\{ \begin{pmatrix} \epsilon_r' \\ \epsilon_r'' \end{pmatrix}_1, \begin{pmatrix} \epsilon_r' \\ \epsilon_r'' \end{pmatrix}_2, \begin{pmatrix} \epsilon_r' \\ \epsilon_r'' \end{pmatrix}_3, \cdots, \begin{pmatrix} \epsilon_r' \\ \epsilon_r'' \end{pmatrix}_K \right\}, \tag{4.15}$$

where K is the total number of samples. The aim is to approximate $p(\epsilon_r)$ based on
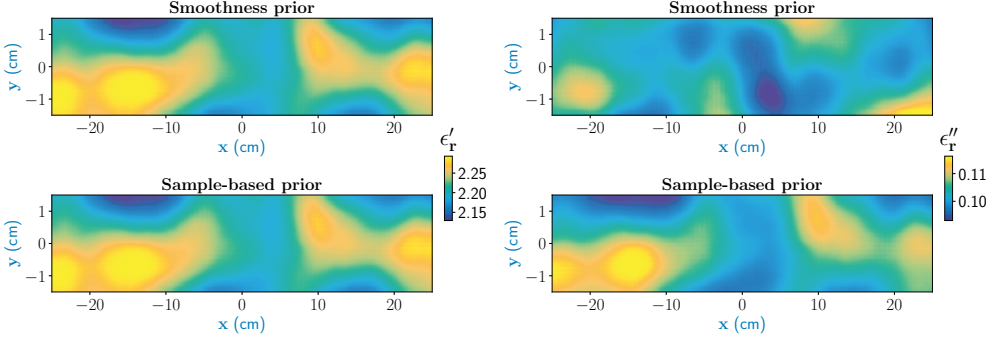
Figure 4.1: Real (left) and imaginary (right) parts of the dielectric constant for samples drawn from uncorrelated smoothness and sample-based prior models.

the $\mathbb{X}$. For this we calculated the sample mean

$$\eta_{\epsilon_r} = \begin{pmatrix} \eta_{\epsilon_r'} \\ \eta_{\epsilon_r''} \end{pmatrix} \approx \frac{1}{K} \sum_{j=1}^{K} \begin{pmatrix} \epsilon_r' \\ \epsilon_r'' \end{pmatrix}_j, \tag{4.16}$$

and sample covariance

$$\Gamma_{\epsilon_r} \approx \frac{1}{K} \sum_{j=1}^{K} \begin{pmatrix} \epsilon_r' \\ \epsilon_r'' \end{pmatrix}_j \begin{pmatrix} \epsilon_r' \\ \epsilon_r'' \end{pmatrix}_j^\top - \begin{pmatrix} \eta_{\epsilon_r'} \\ \eta_{\epsilon_r''} \end{pmatrix} \begin{pmatrix} \eta_{\epsilon_r'} \\ \eta_{\epsilon_r''} \end{pmatrix}^\top. \tag{4.17}$$

In order to create the dataset $\mathbb{X}$ containing different moisture content realizations, the experimentally obtained mapping as given by Equation (3.6) is applied. A dataset $\mathbb{X}$ with $K = 5000$ random moisture samples was created. For each sample, moisture mean and standard deviation were randomized. Also, the characteristic lengths in each sample were randomized. Using the dataset, prior mean and co-variance were computed. The samples (or realizations) from the sample-based prior density can be generated as

$$\epsilon_r = \eta_{\epsilon_r} + L_{\epsilon_r} Z, \tag{4.18}$$

where Z is a standard normal random vector. A randomized draw from the sample-based prior model is shown in Fig. 4.1 (left). Also, the same sample when we ignore the cross-covariance terms is shown in Fig. 4.1 (right). It is evident that with the sample-based prior model, similar spatial variations are seen in the real and imaginary parts. However, with the neglected cross-covariance matrices, real and imaginary parts show different variations. In the next section, we present numerical examples that show how the choice of two priors affects the MAP estimates and overall estimation accuracy.

4.2.1 Numerical evaluation

We considered a two-dimensional imaging domain $\Omega_{\text{foam}} = [-25,\ 25] \times [-1.5,\ 1.5]$ cm. The 2-D MWT setup is shown in Fig. 4.2 where the sources are represented by number tags $N = 1,2,\cdots,12$. To generate the numerical measurement data, a finite element method (FEM) based COMSOL simulation tool was chosen. Also, we
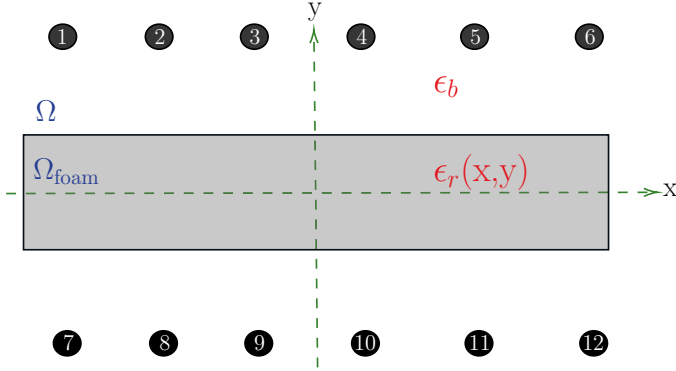
Figure 4.2: Schematic of the 2-D MWT setup used in the study.

added a noise of 3% of the peak value of the the numerical scattered field to the data generated at 8.3 GHz.

In publication **II**, two moisture scenarios to evaluate the estimation quality for the proposed sample-based prior model are considered. To calculate the MAP estimates with the smoothness prior, we set prior $\sigma_{\epsilon_r'} = 1$, and $\sigma_{\epsilon_r''} = 0.1$. The mean value η_{ϵ_r} in the prior was set to dielectric constant of the dry foam, i.e., $1.16 - j0.01$. As for the observation model $\mathscr{F}(\epsilon_r)$, we choose the MoM computation with a pulse basis and point-matching testing function. For the MoM computation at 8.3 GHz, we assume that the imaging domain Ω_{foam} was discretized into 80×20 uniform rectangular pixels. Other computational details are provided in the publication **II**. Furthermore, the profile similarity index, κ (see Equation (3.12)) and root mean square error (RMSE) metrics were calculated to asses the quantitative estimation performance. As a special case, a foam with top surface as rough was also evaluated. The details of the three cases are as follows.

- *Case 1:* In this case, a high moisture scenario was considered and its MAP estimation with smoothness prior model and sample-based prior model is shown in Fig. 4.3 (real part) and Fig. 4.4 (imaginary part). It can be seen that with both the priors the real part is estimated fairly well. But the estimation of the imaginary part is much more accurate with the sample-based prior model with certain moisture regions being clearly indicated. The MAP estimate and true values for a fixed value $y = 0$ cm along the cross-section of the foam with ± 3 posterior standard deviation are plotted in Fig. 4.5. As can be seen from the graph, for the imaginary part the uncertainty was higher when using just smoothness prior than with sample-based prior. Furthermore, the improvement in estimation accuracy using sample-based prior model is more evident from κ and RMSE values shown in Table 4.1.

Table 4.1: RMSE and κ values for the high moisture case.

Prior	Smoothness		Sample-based	
Dielectric	ϵ_r'	ϵ_r''	ϵ_r'	ϵ_r''
RMSE (%)	1.84	31.91	1.79	8.21
κ	0.9752	0.3490	0.9771	0.9610
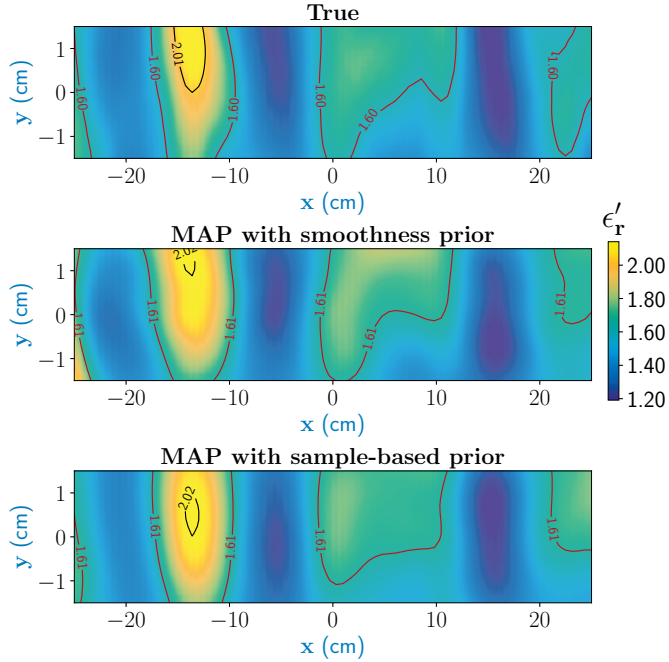
Figure 4.3: High moisture case: MAP estimates with smoothness prior and sample-based prior model for real part of the dielectric constant. Contour is added to highlight the dielectric constant values.

- *Case 2:* In this case, the piece-wise homogeneous moisture distribution in the foam was assumed. This special case was chosen considering practical interest where the moisture is sometimes located in bulk in one portion of the foam. Also, this case was considered to test the generalization capabilities of the algorithm. As it breaks the smoothness assumption which is otherwise present in the dataset of samples used to build the sample-based prior covariance structure. The MAP estimates from the sample-based prior model are shown in Fig. 4.6 along with the true moisture distribution. The estimation accuracy can be evaluated from the κ and RMSE values from Table 4.2 and it favours the sample-based prior model. Note that for this case the MAP with smoothness prior is not shown here to maintain the brevity of the text.

Table 4.2: RMSE and κ values for the piece-wise homogeneous case.

Prior	Smoothness		Sample-based	
Dielectric	ϵ_r'	ϵ_r''	ϵ_r'	ϵ_r''
RMSE (%)	5.2	67.82	4.0582	22.83
κ	0.9017	0.5637	0.9398	0.9362

- *Case 3:* In practise, the top surface of the foam can be rough that means it may have some uncertainty on the surface. In order to investigate the effect of the roughness of the surface, we considered a dielectric foam with a randomly rough surface (RRS) at the top. The random roughness was modeled as follows
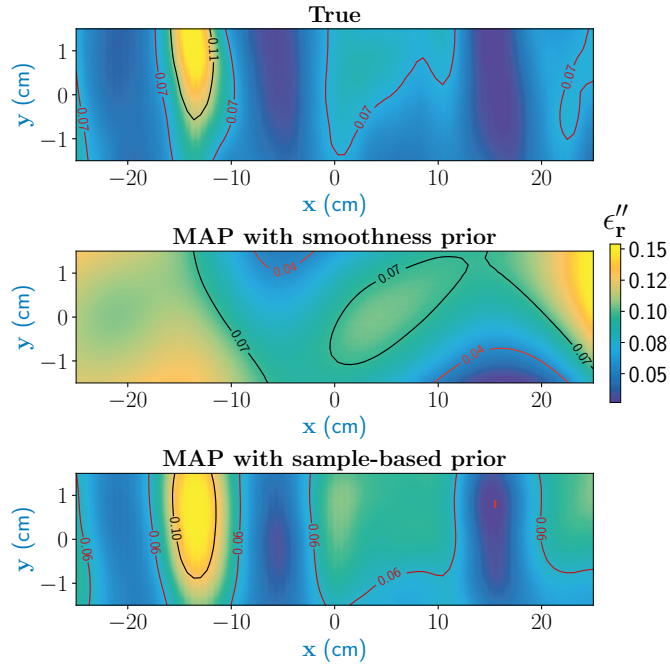
Figure 4.4: High moisture case: MAP estimates for imaginary part of the dielectric constant.
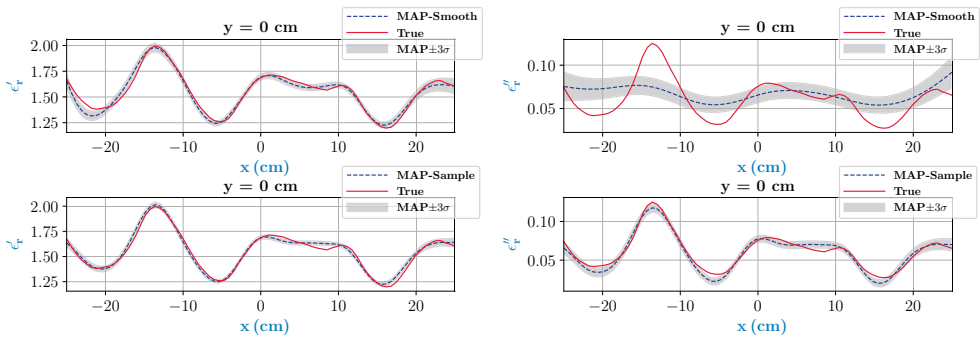
Figure 4.5: Comparison between the true profile and MAP estimate for a high moisture case along the cross-section of the foam y = 0 cm. The light gray color denotes ±3 posterior standard deviation, denoted as σ.
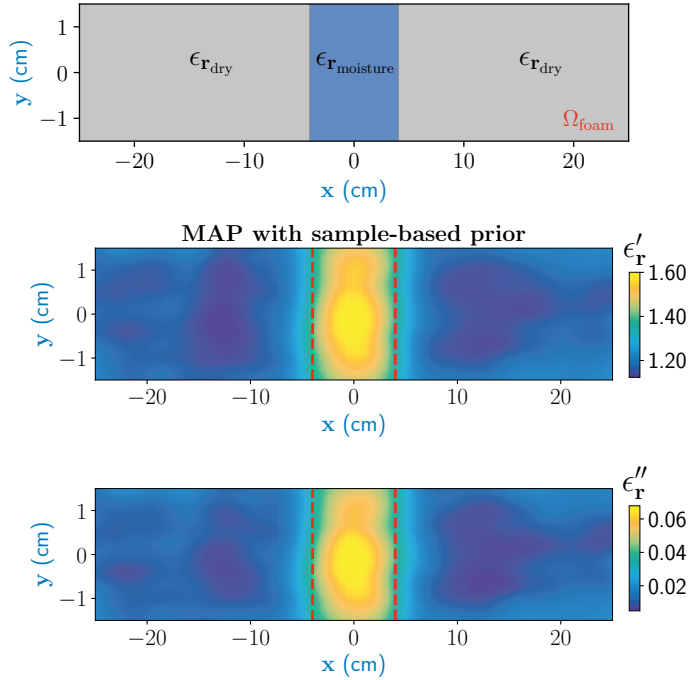
Figure 4.6: MAP estimates for the piece-wise homogeneous moisture scenario (top) with sample-based prior with real (middle) and imaginary parts (bottom) of the dielectric constant. The red dashed lines indicate the true boundary of the moisture profile.
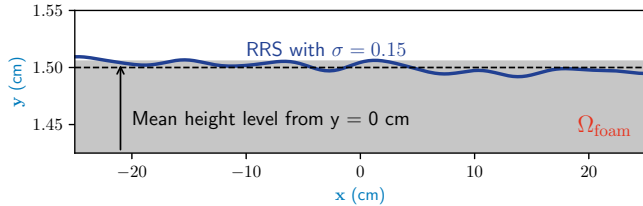
Figure 4.7: Figure shows the top surface of the foam with considered roughness and its mean height.

[111]

$$y(x) = \sum_{m=-M}^{M} m^{-\beta} G_m \cos\left(2\pi m x + U_m\right), \tag{4.19}$$

where m is the integer number representing the spatial frequency and β denotes the spectral exponent, G_m is sampled from a Gaussian distribution $\sim \mathcal{N}(0, \sigma)$, and $U_m \sim \mathcal{U}(0, 2\pi)$ is sampled from the uniform distribution. The random rough surface was characterized by the following parameters: $\sigma = 0.15$, and $\beta = 0.8$. To obtain the scattered field, a hot-spot with 40% moisture $\epsilon_r = 1.3785 - j0.0432$ with radius $1\,\text{cm}$ at position $(15\,\text{cm}, 0\,\text{cm})$ was considered. In the smoothness prior-based MAP estimate, shown in Fig. 4.9 (top),
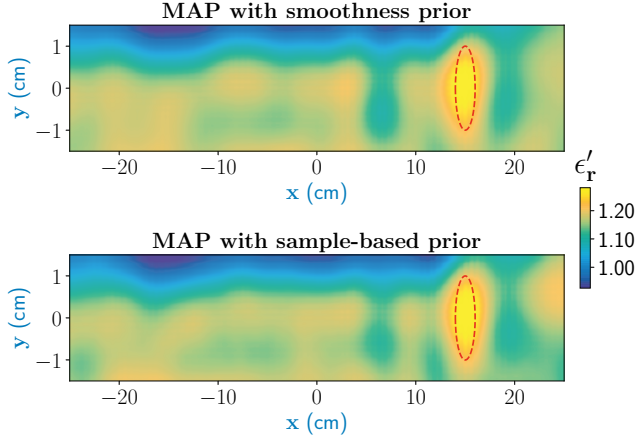
Figure 4.8: MAP estimate of the real part with smoothness prior and sample-based prior of a hot-spot area embedded inside the foam with an assumed rough top surface with $\sigma = 0.15$.
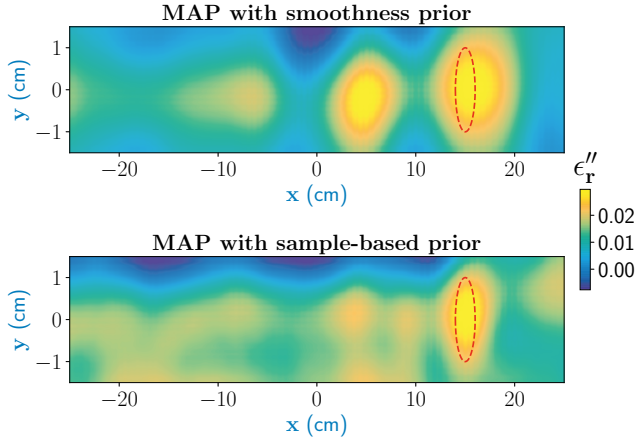
Figure 4.9: MAP estimate of the imaginary part. Otherwise same caption as in Figure 4.8.

the imaginary part indicates the presence of strong artifacts. On the other hand, with the sample-based prior the accuracy is clearly improved. But, with both prior models, the shadow images are also visible due to the modelling errors as the MoM forward model assumes mean height of the top surface only, and not the actual roughness.

4.2.2 Experimental results

In this section, the sample-based prior model is tested on the scattered electric field data from the experimental MWT data for a wet-spot moisture case in a planar foam of size $50 \times 7.6 \times 75$ cm. To create the wet-spot moisture target, a spherical piece of foam of diameter 2.5 ± 0.1 cm and with 46% wet-basis moisture level ($\epsilon_r \approx$
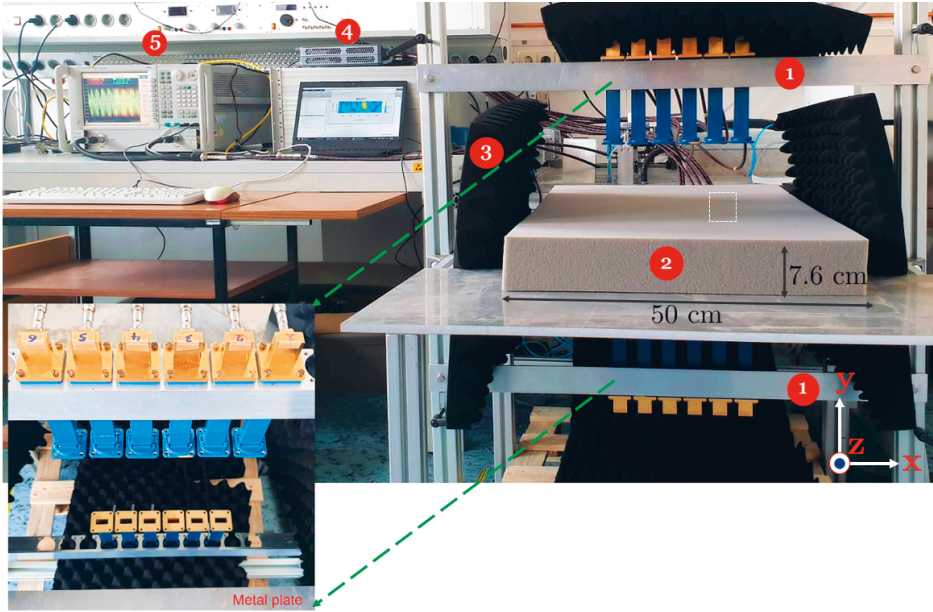
Figure 4.10: Experimental setup of the MWT system with sensors placed on both sides of the foam. The alignments of the top and bottom antennas are shown on the bottom left by a green arrow and a portion of the metal plate is removed to enable wave propagation between the top and bottom antennas.

2.0 − j0.085) was chosen. An approximate location of the target inside the foam is centered at (−9 cm, 1.55 cm, 0 cm). The MWT experimental prototype is similar to that was shown in Chapter 3 but with antennas placed also in the bottom side and with no metal plate in between. The setup is shown in Fig. 4.10 with the sensor array represented by number Tag 1 and the polymer foam is shown by number Tag 2 which is surrounded by absorbers as shown by number Tag 3. The measurement data acquisition setup consists of the solid state switch and VNA which are denoted by the number Tags 4 and 5, respectively. The location plane of the test target is shown in right by white dashed lines.

For MAP computation, the standard deviations of the measurement noise was calculated for 8.3 GHz frequency following the approach used in [112]. The MAP estimate with the smoothness prior and sample-based prior are shown in Fig. 4.12 for the selected x-y plane at $z = 0$ cm. With the smoothness prior, the location of the target and its value are satisfactorily estimated in the real part. However, the imaginary part shows a completely different spatial variation of the moisture distribution in the foam. With the sample-based prior, a significant improvement in the MAP estimate is observed. It is clear that with the sample-based prior approach, the obtained MAP estimates offer a good reconstruction accuracy in comparison to the smoothness prior model.

4.3 STRUCTURAL PRIOR MODEL

Often, in MWT, the structural prior knowledge is also used to improve the estimation accuracy. In frequency-domain MWT, ideas on using structural prior knowl-
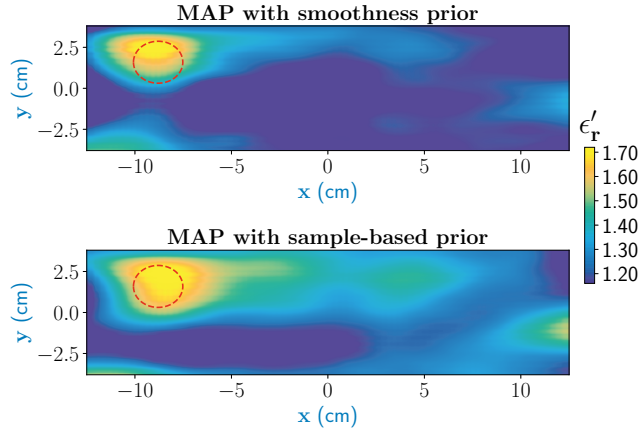
Figure 4.11: MAP estimate of the real part with smoothness prior and sample-based prior of a wet-spot area embedded inside the foam in the experimental study. The red-dashed line indicate the true mean location of the target.
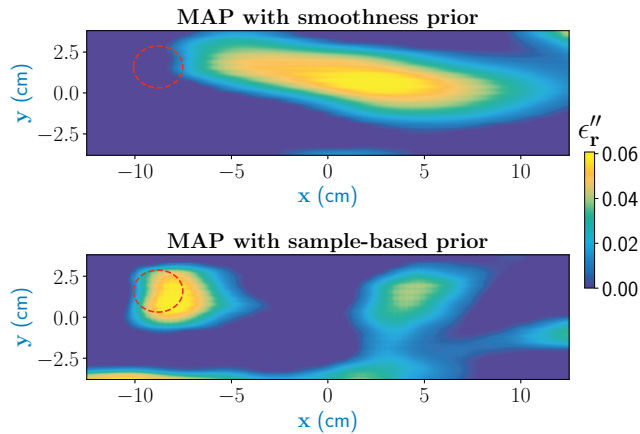
Figure 4.12: MAP estimate of the imaginary part. Otherwise same caption as in Fig. 4.11.

edge to improve the reconstruction accuracy are reported in biomedical applications in [113–115]. In these articles, the structural prior information is extracted from other imaging modalities such as ultrasound or MRI and used in the construction of prior. However, considering overall system cost, employing a dual-imaging modality can be critical in industrial applications. To avoid dual imaging setup, alternative strategies based on radar-based regional imaging [116–118] have been studied and have proven very effective in improving the image quality. However, the aforementioned technique utilises mono-static scanning configuration for data acquisition which is again time-consuming. Using the available electromagnetic measurements (i.e., the same setup) to form structural prior information is gaining pace and has been tested with algorithms in time-domain [119, 120] and frequency-domain [121].

In the publication **III**, we proposed to use the structural knowledge about the domain from multistatic uniform diffraction tomography (MUDT) algorithm that conveys the location of the wet-spots and dry part regions inside the foam. In MUDT, the location of an object inside the imaging domain is determined by the linear relationship between the relative complex permittivity function and the received signal in the spectral domain [122]. In comparison to UDT [123, 124], the MUDT approach i) eliminates the need for mechanical scanning of the sensor, ii) provides aliasing-free images by following Nyquist sampling criteria, and can resolve multiple targets with significant improvement in the spatial resolution. Using the support information from the MUDT, varying degree of smoothness was applied in different regions i.e. in the dry part and inside the wet-spots in the modelling of prior. The overall inversion strategy is shown in Fig. 4.13. Overall, the objective is to relax the smoothing constraints in the dry areas along the tangential and normal directions with respect to the support domain of the targets. To achieve different degree of smoothness, characteristic length (CL) components and standard deviations terms are chosen separately for dry and wet-spots regions. Specifically, the prior covariance matrix was modified as

$$C_{ij} = \begin{cases} C_{ij}(c_{x_1}, c_{y_1}) \ \forall \ i,j \in \Omega_d \\ C_{ij}(c_{x_2}, c_{y_2}) \ \forall \ i,j \in \Omega_h, \end{cases} \tag{4.20}$$

where Ω_d and Ω_h represent the approximated dry part and wet-spot support regions, respectively. The terms c_{x_1}, c_{y_1} and c_{x_2}, c_{y_2} are the CL components in wet-spot and dry regions, respectively. Large CL along with small amplitude (standard deviation) in the dry part will constrain the estimate to have constant neighbourhood structure in the domain. This is equivalent to assuming that pixel elements are more correlated in the dry regions.
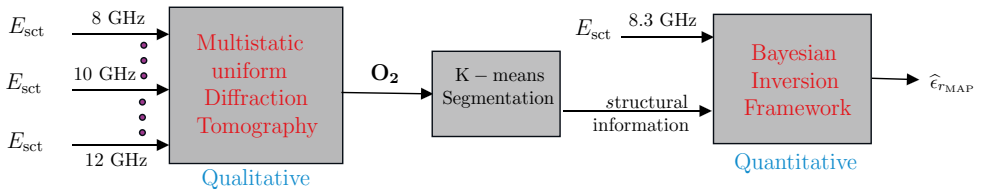
Figure 4.13: General framework of the proposed method. © 2022 IEEE.

4.3.1 Numerical evaluation

In the publication **III**, 3-D model with waveguide antennas with similar configuration as in Fig. 4.2 was used to generate the synthetic measurement data. The model was built in the commercial software CST Studio Suite with time-domain solver. In the modelling part, the computational domain consisted of a porous foam $\Omega_{\text{foam}} = [0, 25] \times [-15, 15] \times [-4, 4]$ cm are surrounded by air. Antennas were positioned with their open-ended center points located at -15 cm to 15 cm with 5 cm center to center distance along the y-axis. The data was generated in X-band frequency range (from 8 GHz to 12 GHz) with a frequency step of 5 MHz and stored in terms of a scattering matrix of size 14×14 ($N = 14$). We considered two test examples to evaluate the estimation accuracy with structural smoothness prior. The size of the targets were considered in terms of wavelength of center frequency ($\lambda_c = 3$ cm) of X-band range. Implementation details of the MUDT are discussed in [122] and only the main results are shown here. For the MAP estimation, we followed the same calculation strategy as presented in Section 4.2. Results of this approach are discussed with the following cases.

Case 1: Two spherical moisture wet-spots

In this case, different moisture levels with radii of $0.67\lambda_c$ are assumed. The first wet-spot with 35% moisture level is centered at $(12.5\,\text{cm}, 0\,\text{cm}, 0\,\text{cm})$ and the second wet-spot with 25% moisture level ($\epsilon_r \approx 1.48 - j0.056$) is centered at $(12.5\,\text{cm}, 10\,\text{cm}, 0\,\text{cm})$. In Figure 4.15, localisation information from MUDT is shown. Results show that the dominant wet-spot is clearly detected, while the drier wet-spot is also visible but not as strong as the other one as represented by the red dashed circle in top of the Fig. 4.14 (top).

   To calculate the MAP estimate, information from MUDT with K-means segmentation was used in the structural smoothness prior model. In the structural prior, the CL are set to $c_{x_1} = 30$ cm, and $c_{y_1} = 8$ cm for the dry part (with very small standard deviation values set for $\sigma_{\epsilon_{r'}}$ and $\sigma_{\epsilon_{r''}}$) and for the supported domain of wet-spots, CL of $c_{x_2} = 3$ cm, and $c_{y_2} = 3$ cm (with standard deviation values set for $\sigma_{\epsilon_{r'}} = 1$, and $\sigma_{\epsilon_{r''}} = 0.075$) are chosen. The sigma values in the wet-spots regions are selected based on the dielectric characterisation data and $\pm 3\sigma$ can account for 99% of the dielectric values in the prior from the set mean value of $\eta_{\epsilon_r} = 1.16 - j0.01$. Also, we calculated the MAP estimate with smoothness prior model with a CL of $c_x = 8$ cm, and $c_y = 4$ cm. In the smoothness prior, we set $\sigma_{\epsilon_{r'}} = 1$, $\sigma_{\epsilon_{r''}} = 0.075$ and $\eta_{\epsilon_r} = 1.16 - j0.01$. The MAP estimates with smoothness prior model and structural prior model are shown in Fig. 4.14.

   With the smoothness prior, the location of wet-spot is somewhat enlarged and real part of its dielectric value is underestimated. However, with the structural smoothness prior, MAP estimate for the real part of the dielectric constant is very close to true case and also the wet-spot is recovered within the correct domain. Further, for easier quantitative comparison, pixel values at data line $y = 0$ cm are compared against the true case and shown in the bottom row of Fig. 4.15. The structural prior follows the discontinuities and aligns closer to the real value than the smoothness prior case.
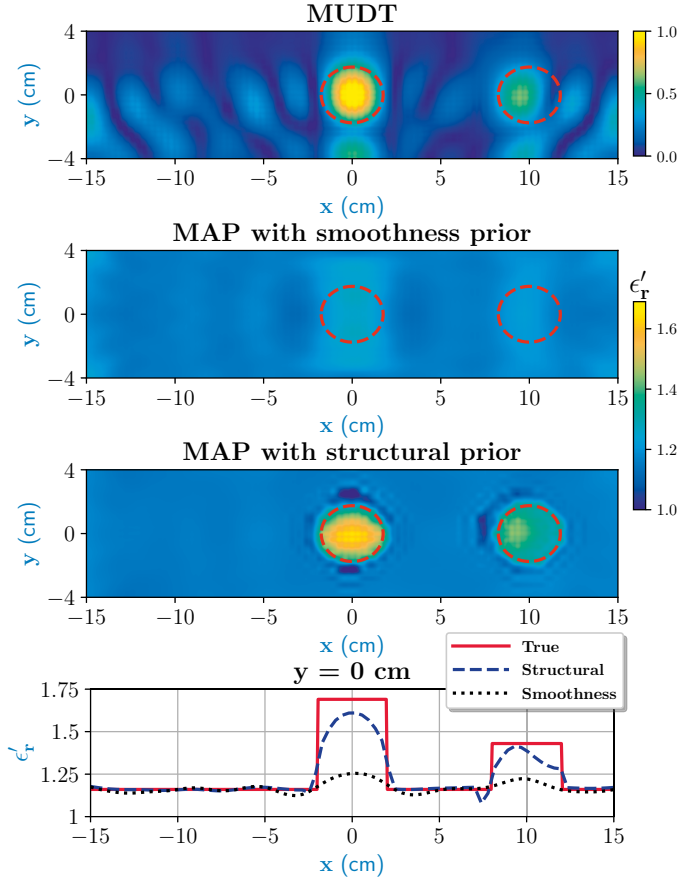
Figure 4.14: MUDT and MAP estimates for the two wet-spots with different moisture case. The bottom figure shows the comparison of MAP with structural and smoothness prior model with the true case for the pixel values located at data line $y = 0$ cm.© 2022 IEEE.

Case 2: Rectangular case

In this scenario, a rectangular distribution for the wet-spot was considered with a moisture content of 30% ($\epsilon_r \approx 1.58 - 0.06j$) and dimension $2.6\lambda_c \times 1.3\lambda_c \times 6.5\lambda_c$ located at the center of the foam.

The reconstructed image using MUDT is shown in Fig. 4.15 (top). As can be seen from this figure, the exact boundary of the distribution is not reconstructed. Although, the K-means segmentation has resulted in covering a slightly larger domain.

The MAP estimates are calculated based on the parameter set in the previous case. The results are shown in Fig. 4.15. The corners/discontinuities are difficult to estimate with the smoothness prior and more so the estimation shows an irregularity with stretched boundaries and incorrect level of moisture. As can be seen, the structural prior detects the irregularity and locates it more accurately than the smoothness prior. Overall, its performance is more accurate as evident from line
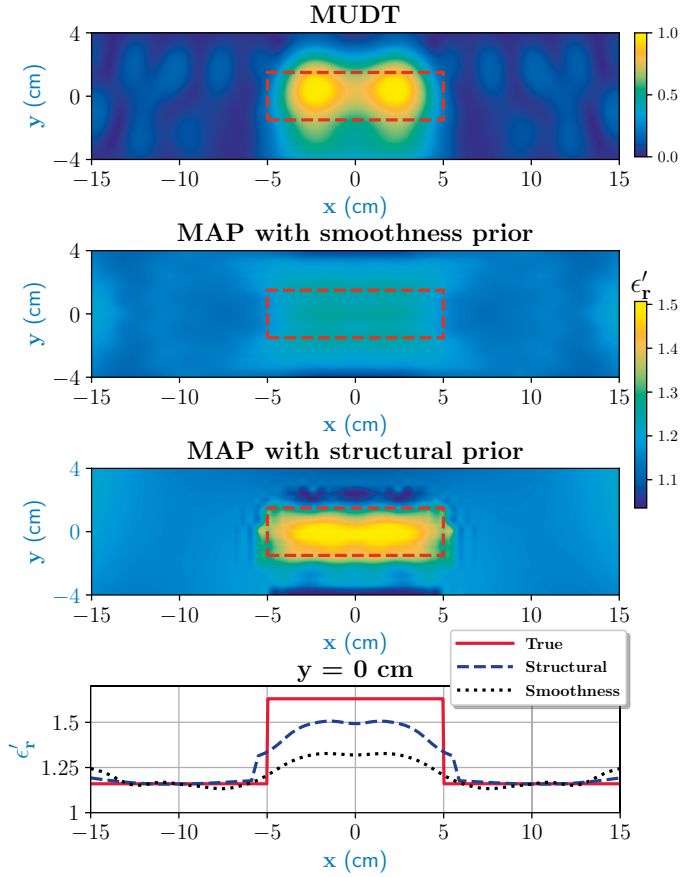
Figure 4.15: MUDT and MAP estimates for the rectangular distribution case. Otherwise the same caption as in Fig. 4.14.© 2022 IEEE.

graph in the Fig. 4.15 (bottom). Note that even though the CL in the structural prior are set to the previous case, which does not match with the actual changes, the estimate is still good.

4.3.2 Experimental results

Three moisture scenarios were considered in the experimental study. Their respective scattered field data collected from the setup shown in Fig 4.10.

In the first case, a spherical wet-spot with diameter 2.5 ± 0.1 cm and with 45% wet-basis moisture level ($\epsilon_r \approx 2.0 - 0.092j$) was considered. An approximate location of the irregularity inside the foam is centered at $(0\,\text{cm}, -9\,\text{cm}, 1.55\,\text{cm})$.

From the MUDT image, the structural information is extracted using K-means segmentation (not shown here) and utilised to form the structural prior model in which the CL of $c_{x_1} = 25$ cm, and $c_{y_1} = 7$ cm for the dry part and for the supported domain of wet-spot, CL of $c_{x_2} = 3$ cm, and $c_{y_2} = 3$ cm are chosen. Also, we calculated the MAP estimates with smoothness prior model with a CL of $c_x = 8$ cm, and $c_y = 4$ cm. The MAP estimates are shown in middle and last row of Fig. 4.16 (i). Although
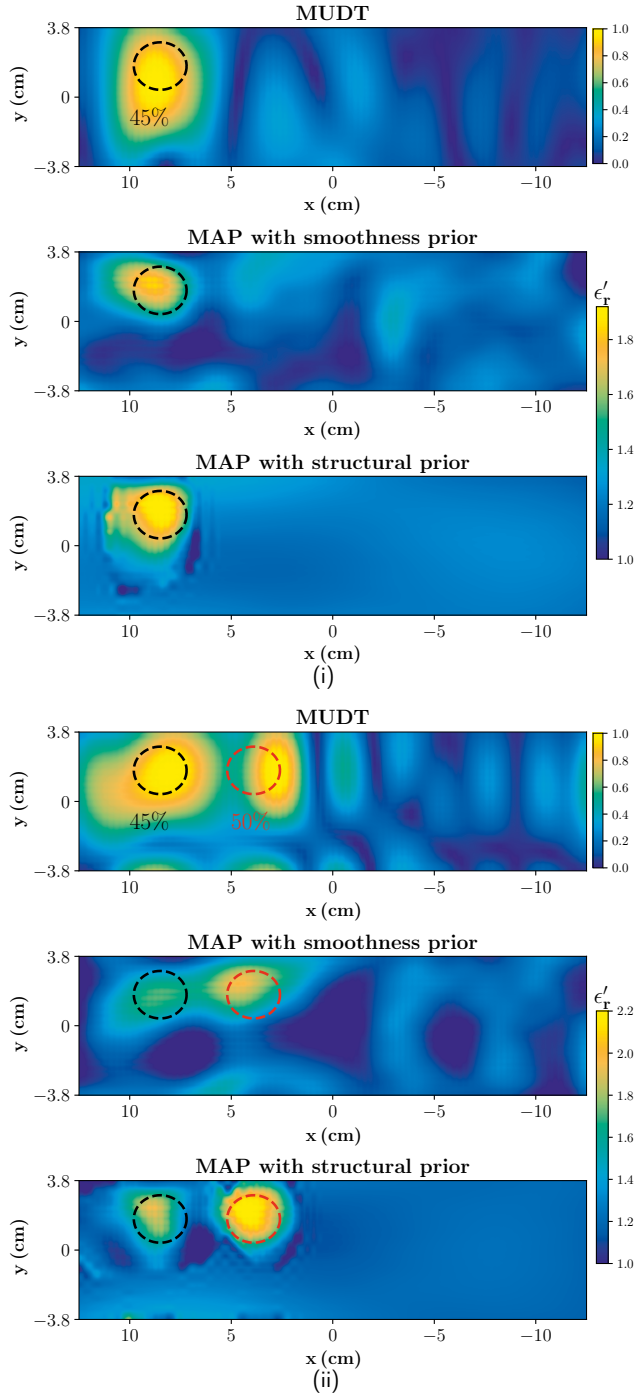
Figure 4.16: MUDT and MAP estimates for cases (i) one wet-spot with 45% moisture and (ii) two wet-spots with 45% moisture and 50% moisture, respectively. The dashed circles indicate the true positions of the wet-spots.© 2022 IEEE
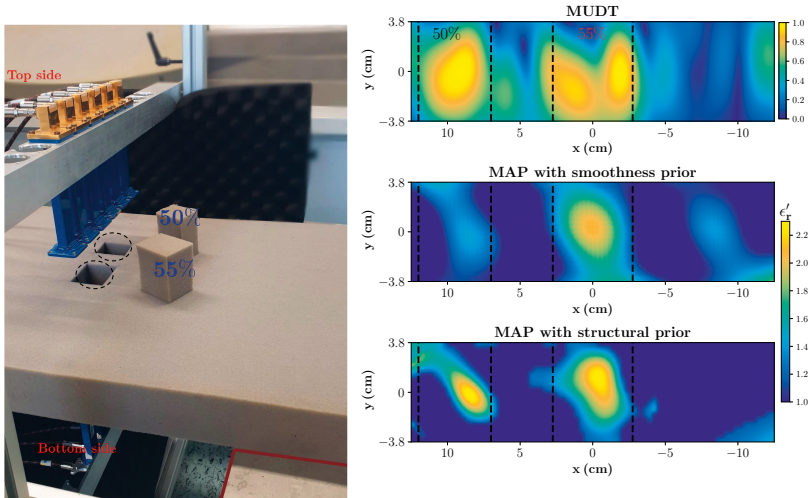
Figure 4.17: Left: two cubic moisture case: moisture levels of 50% and 55% are impregnated in the incised foam, respectively. Right: MUDT and MAP estimates for the two cubic case. The dashed lines indicate the true positions of the inclusions. © 2022 IEEE.

the wet-spot is somewhat correctly located with both the priors, the estimate with the structural prior is more accurate than the smoothness prior solution. In addition, artifacts are also visible in the MAP solution with smoothness prior. Improvement in the image quality with structural prior can be speculated to be due to suppression of smooth variations in the background (i.e. the dry part).

In the second experiment, we inserted two wet-spots with moisture percentage of 50% ($\epsilon_r \approx 2.2 - 0.1j$) and 45% ($\epsilon_r \approx 1.98 - 0.076j$), respectively. The location of the wet-spot with 50% is centered at $(0\,\text{cm}, -3.6\,\text{cm}, 1.55\,\text{cm})$ and location of the wet-spot with 45% is the same as in the previous case. In the K-mean segmentation of the MUDT image, the two regions got merged as the two irregularities are close and share the same neighbourhood; it then results in forming a nearly ellipsoid region which is then used in the structural prior. To evaluate the MAP estimate the CL parameters are kept the same as in the previous case. From the MAP estimates in Fig. 4.16 (ii), it can be seen that the two wet-spots are retrieved more accurately than with the smoothness prior even though the structural information from segmentation indicated a wider domain and CL are set to smaller dimension.

In the third case, two cubic shape pieces are cut out from the foam and infused with moisture levels of 50% ($\epsilon_r \approx 2.2 - 0.1j$) and 55% ($\epsilon_r \approx 2.4 - 0.16j$) in its full volume, respectively as shown in Fig. 4.17 (left). For this case, the localization information from the MUDT was improper mainly due to limited independent data. This resulted in incomplete structural knowledge of the targets. In the structural prior, we have set the same CL in both regions similar to the first case. From the MAP estimations shown in Fig. 4.17 (right), a clear presence of higher moisture is still indicated, though not in full volume, with structural prior model in comparison to the smoothness based solution that can only locate moisture presence in the middle inclusion. The false solution in the smoothness prior model can be speculated to be due to over-regularisation or smoothing effect. Overall, incorporating struc-

40

tural prior model has improved the accuracy of estimated moisture location and its dielectric properties. We also noticed that even with change in CL to larger values the results show no significant changes.

5 Discussions and conclusions

In this thesis, application of microwave tomography (MWT) towards process imaging in the industrial drying system is presented. The imaging modality was applied to estimate the moisture content in a porous polymer foam in terms of relative dielectric constant. For the inversion of MWT, the neural network approach and Bayesian inversion framework with correlated sample-based prior and structural prior was employed. Both the approaches were tested under the static case conditions with numerical and experimental data from the developed MWT system. The estimation results are compared against the respective true cases by error metrics RMSE and profile similarity index and comparison indicates good estimation results.

In the publication **I**, we applied a reconstruction scheme based on a convolutional neural network (CNN) to estimate the moisture content in a polymer foam. For the training of the network, a numerical database which consists of different moisture samples with smooth distribution and corresponding electric field responses computed using the 2-D method of moment computational technique was used. The moisture samples were generated using a parametric model derived from the laboratory-based dielectric characterization of the foam. The CNN architecture was selected empirically which implies that there may exist some other network architecture that can give relatively better performance. However, our rationale was to choose a network with fewer layers instead of deep layer networks, for example, *U-Net*, that needs extra computational load to give very high accuracy or super-resolution as needed in microwave medical imaging applications [125,126]. Although our achieved results with numerical data had good accuracy, uncertainties in the estimations were still pertinent. This was caused mainly due to underlying uncertainties associated with the dielectric characterization data and higher noise levels considered in the simulations. Meanwhile, with the experimental data, the estimated values are found underestimated which are caused due to modeling errors, i.e., 3-D measurements and 2-D forward model. Furthermore, we also observe that in the estimates the background information, i.e., the dry part is not well distinguishable. This is mainly due to the Gaussian based covariance structure used for generating moisture distribution. One solution is to use covariance structure models with a scaling factor such as Matérn class [90]. Overall, results showed promising accuracy with less than $\pm 10\%$ relative estimation error and the method's potential to be used for real-time moisture estimation purpose in the industrial drying system. For our work, the scope for improvement lies in the uncertainty quantification (UQ). In general, UQ in deep neural networks is a very active research topic and several approaches have been proposed and studied, see for example the recent reviews [127].

Although, the neural network framework is fast in providing a reconstruction, however, changes for example, in (i) the size of the imaging domain, (ii) the roughness of the top surface or high randomness (iii) possible values appearing in real cases outside the simulated range of values of dielectric constant may lead to erroneous reconstruction. Therefore, in this thesis, as an alternative, the feasibility of the

classical knowledge-driven inverse problem approach based on the Bayesian inversion framework is also tested and reported in the publications **II** and **III**. The main idea of the publications was to improve the *maximum a posteriori* (MAP) estimates by exploiting the prior model.

In the publication **II**, we proposed a sample-based prior model to favour the joint estimation of the real and imaginary parts of the dielectric constant. To construct the sample-based prior model, we used a large dataset consisting of simulated moisture samples to evaluate the prior mean and built the prior covariance structure. In each sample, moisture values are chosen based on the parametric model obtained from the dielectric characterization of the foam. The proposed approach is tested with 2-D numerical microwave tomography data at 8.3 GHz for the considered moisture scenarios. For the considered test cases, the average estimation error (RMSE) obtained using smoothness prior model for real and imaginary parts were less than 1% and 11%, respectively. Conversely, with the sample-based prior model the estimation error for the imaginary part is reduced to less than 4%. This shows that in comparison to the uncorrelated smoothness prior a significant improvement in the estimation result is achieved with the sample-based prior model. Also, the average profile similarity index for the imaginary part with the smoothness and the sample-based prior model is 0.48 and 0.9, respectively that clearly highlights the effectiveness of the sample-based prior model on the overall reconstruction accuracy. Note that average profile similarity index for the real part for both the prior cases is 0.9.

Further, the developed algorithm was tested on the MWT experimental prototype data and reconstruction results are observed to be close to the true case with the sample-based prior model. However, the overall estimation accuracy is slightly reduced in comparison to the simulated studies which may be caused due to the modeling errors. Together with the source modeling error, this discrepancy might be caused due to the 2-D vs. 3-D Green's function mismatch when the geometry of the target is no longer independent of one of the coordinates. In essence, these errors are predominant for the case when spherical geometries are assumed for the wet-spots in comparison to infinitely extended scatterer cases (where the general performance of the 2-D forward model with line sources is good). A detailed discussion was provided in [128] for medical imaging applications but is equally applicable for our application as well. Nonetheless, the source model errors remain persistent in our study. Thus, one potential way to improve the reconstructions is to use the Bayesian inversion approach in conjunction with the approximation error scheme [129] which can accommodate the statistics of these errors resulting in better estimates. Further, in the industrial drying system, the foam temperature will be higher than the room temperature at the exit. Therefore, the dielectric characterization of the foam with wet-basis moisture levels at different temperatures can be helpful in practice. The Bayesian inversion can produce effective results but its implementation for real-time process imaging may be challenging. This is mainly due to the iterative nature of the inversion algorithm and full-array sensor configuration (antennas placed on both sides of the target) that is observed to increase the data acquisition time. Therefore, for real-time implementation limited-view MWT setup with statistical inversion framework and GPU support is a way forward.

In the publication **III**, a coupled MWT imaging method was proposed for obtaining the location of the moisture and its dielectric constant values in the polymer foam. The goal was to improve the reconstruction quality of the Bayesian inversion algorithm by incorporating structural prior information derived from the qualita-

tive imaging algorithm known as the multi-static diffraction tomographic imaging algorithm (MUDT). The MUDT was employed to estimate the support domain of the target based on which the structural smoothness prior model for Bayesian inversion was derived. This way of obtaining structural prior information is effective as it utilizes the data from the same microwave sensor setup in contrast to the priors derived for other imaging modalities or radar-based techniques. The validity of the proposed approach is tested with 3-D synthetic data for pragmatic moisture cases and compared with that of solution from smoothness prior. In the final steps, the proposed imaging algorithm was verified with experimental data from the developed MWT setup and results show that there is a significant increase in accuracy and in overall image quality. It could be concluded that the proposed combined method i) eliminates the need to employ multi-frequency reconstruction, ii) unlike dual-imaging modalities, utilizes the same MWT setup for the estimation of the locations and dielectric constant levels of the hot-spots, iii) improves the reconstruction accuracy over the conventional MAP estimate based on smoothness priors. In general, the proposed method can be extended for the through-the-wall radar imaging (TWRI) applications, ground penetrating radar (GPR) applications. In this study, only isolated regions of moisture were considered during the numerical and experimental study. These situations arise especially at the outlet stage in the drying process since the foam has been partially dried due to the heating operation. Therefore, it would be beneficial to integrate MWT at the outlet rather than at the inlet to fully justify the use of structural prior knowledge. Owning to low contrast values at the outlet of the drying system, a one-shot single frequency non-linear difference imaging based on the Bayesian framework and structural prior from time-reversal imaging [130] with only reflection data (with the antennas only on top) can be utilized towards real-time imaging.

In conclusion, the research presented in this thesis develops inversion techniques based on neural networks and the Bayesian inversion framework for MWT for its application in the industrial drying system. The neural network approach is found suitable for meeting the goals of industrial process tomography such as real-time image reconstruction and supports fast data acquisition due to single-frequency operation. On the other hand, the Bayesian approach has shown good estimation accuracy for different cases considered under numerical and experimental study. Nevertheless, in general, due to the iterative nature of the algorithm and due to the full-angle setup, its implementation for real-time process imaging may be challenging especially during the continuous processing mode (target moving on a conveyor belt). Therefore, testing the Bayesian approach with e.g. limited angle setup and GPU computing is the way forward. Finally, we envisage that the proposed prior models in the Bayesian methodology are even applicable for medical applications of microwave imaging.

BIBLIOGRAPHY

[1] M. Pastorino, *Microwave Imaging* (John Wiley & Sons, 2010).

[2] X. Chen, *Computational Methods for Electromagnetic Inverse Scattering* (John Wiley & Sons, 2018).

[3] M. Dehmollaian and K. Sarabandi, "Refocusing Through Building Walls Using Synthetic Aperture Radar," *IEEE Transactions on Geoscience and Remote Sensing* **46**, 1589–1599 (2008).

[4] F. Soldovieri and R. Solimene, "Through-Wall Imaging via a Linear Inverse Scattering Algorithm," *IEEE Geoscience and Remote Sensing Letters* **4**, 513–517 (2007).

[5] L. Li, A. E.-C. Tan, K. Jhamb, and K. Rambabu, "Buried Object Characterization Using Ultra-Wideband Ground Penetrating Radar," *IEEE Transactions on Microwave Theory and Techniques* **60**, 2654–2664 (2012).

[6] F. Tosti, G. Gennarelli, L. Lantini, I. Catapano, F. Soldovieri, I. Giannakis, and A. M. Alani, "The Use of GPR and Microwave Tomography for the Assessment of the Internal Structure of Hollow Trees," *IEEE Transactions on Geoscience and Remote Sensing* **60**, 1–14 (2022).

[7] L. E. Larsen and J. H. Jacobi, "Microwave scattering parameter imagery of an isolated canine kidney," *Medical Physics* **6**, 394–403 (1979).

[8] A. Fedeli, V. Schenone, A. Randazzo, M. Pastorino, T. Henriksson, and S. Semenov, "Nonlinear S-Parameters Inversion for Stroke Imaging," *IEEE Transactions on Microwave Theory and Techniques* **69**, 1760–1771 (2021).

[9] M. S. Beck and R. A. Williams, "Process tomography: a European innovation and its applications," *Measurement Science and Technology* **7**, 215–224 (1996).

[10] Z. Wu and H. Wang, "Microwave Tomography for Industrial Process Imaging: Example Applications and Experimental Results.," *IEEE Antennas and Propagation Magazine* **59**, 61–71 (2017).

[11] Z. Akhter, A. K. Jha, and M. J. Akhtar, "Generalized RF Time-Domain Imaging Technique for Moving Objects on Conveyor Belts in Real Time," *IEEE Transactions on Microwave Theory and Techniques* **65**, 2536–2546 (2017).

[12] E. Nyfors, "Industrial Microwave Sensors—A Review," *Subsurface Sensing Technologies and Applications 1* 23-43 (2000).

[13] P. Monk, *Finite Element Methods for Maxwell's Equations* (Oxford University Press, 2003).

[14] C. Balanis, *Advanced Engineering Electromagnetics* (Wiley, 2012).

[15] M. Born, E. Wolf, A. B. Bhatia, P. C. Clemmow, D. Gabor, A. R. Stokes, A. M. Taylor, P. A. Wayman, and W. L. Wilcock, *Principles of Optics: Electromagnetic Theory of Propagation, Interference and Diffraction of Light*, 7 ed. (Cambridge University Press, 1999).

[16] A. J. Devaney, *Mathematical Foundations of Imaging, Tomography and Wavefield Inversion* (Cambridge University Press, 2012).

[17] M. Slaney, A. Kak, and L. Larsen, "Limitations of Imaging with First-Order Diffraction Tomography," *IEEE Transactions on Microwave Theory and Techniques* **32**, 860–874 (1984).

[18] D. Colton and P. Monk, "A Linear Sampling Method for the Detection of Leukemia Using Microwaves," *SIAM Journal on Applied Mathematics* **58**, 926–941 (1998).

[19] L. Crocco, I. Catapano, L. Di Donato, and T. Isernia, "The Linear Sampling Method as a Way to Quantitative Inverse Scattering," *IEEE Transactions on Antennas and Propagation* **60**, 1844–1853 (2012).

[20] J. Bolomey, A. Izadnegahdar, L. Jofre, C. Pichot, G. Peronnet, and M. Solaimani, "Microwave Diffraction Tomography for Biomedical Applications," *IEEE Transactions on Microwave Theory and Techniques* **30**, 1998–2000 (1982).

[21] T.-H. Chu and K.-Y. Lee, "Wide-band microwave diffraction tomography under Born approximation," *IEEE Transactions on Antennas and Propagation* **37**, 515–519 (1989).

[22] M. Fink, "Time reversal of ultrasonic fields. I. Basic principles," *IEEE Transactions on Ultrasonics, Ferroelectrics, and Frequency Control* **39**, 555–566 (1992).

[23] M. Yavuz and F. Teixeira, "Full time-domain DORT for ultrawideband electromagnetic fields in dispersive, random inhomogeneous media," *IEEE Transactions on Antennas and Propagation* **54**, 2305–2315 (2006).

[24] A. Omrani, M. Moghadasi, and M. Dehmollaian, "Localisation and permittivity extraction of an embedded cylinder using decomposition of the time reversal operator," *IET Microwaves, Antennas Propagation* **14**, 851–859(8) (2020).

[25] A. J. Devaney, "Nonuniqueness in the inverse scattering problem," *Journal of Mathematical Physics* **19**, 1526–1531 (1978).

[26] P. C. Hansen, "Numerical tools for analysis and solution of Fredholm integral equations of the first kind," *Inverse Problems* **8**, 849–872 (1992).

[27] A. Devaney and G. Sherman, "Nonuniqueness in inverse source and scattering problems," *IEEE Transactions on Antennas and Propagation* **30**, 1034–1037 (1982).

[28] A. Kirsch, *An Introduction to the Mathematical Theory of Inverse Problems* (Springer New York, 1996).

[29] W. Chew and Y. Wang, "Reconstruction of two-dimensional permittivity distribution using the distorted Born iterative method," *IEEE Transactions on Medical Imaging* **9**, 218–225 (1990).

[30] P. M. van den Berg and R. E. Kleinman, "A contrast source inversion method," *Inverse Problems* **13**, 1607–1620 (1997).

[31] X. Chen, "Application of signal-subspace and optimization methods in reconstructing extended scatterers," *Journal of the Optical Society of America A* **26**, 1022–1026 (2009).

[32] X. Chen, Z. Wei, M. Li, and P. Rocca, "A review of deep learning approaches for inverse scattering problems," *Progress In Electromagnetics Research* **167**, 67–81 (2020).

[33] A. Massa, D. Marcantonio, X. Chen, M. Li, and M. Salucci, "DNNs as Applied to Electromagnetics, Antennas, and Propagation—A Review," *IEEE Antennas and Wireless Propagation Letters* **18**, 2225–2229 (2019).

[34] A. Franchois and C. Pichot, "Microwave imaging-complex permittivity reconstruction with a Levenberg-Marquardt method," *IEEE Transactions on Antennas and Propagation* **45**, 203–215 (1997).

[35] N. Joachimowicz, C. Pichot, and J. Hugonin, "Inverse scattering: an iterative numerical method for electromagnetic imaging," *IEEE Transactions on Antennas and Propagation* **39**, 1742–1753 (1991).

[36] Z. Wu, "Developing a microwave tomographic system for multiphase flow imaging: advances and challenges," *Transactions of the Institute of Measurement and Control* **37**, 760–768 (2015).

[37] R. Collin, *Foundations for Microwave Engineering* (McGraw-Hill, 1992).

[38] L. E. Feher and M. K. Thumm, "Microwave innovation for industrial composite fabrication-the HEPHAISTOS technology," *IEEE Transactions on Plasma Science* **32**, 73–79 (2004).

[39] G. Link and V. Ramopoulos, "Simple analytical approach for industrial microwave applicator design," *Chemical Engineering and Processing - Process Intensification* **125**, 334–342 (2018).

[40] L. Feher, *Energy Efficient Microwave Systems: Materials Processing Technologies for Avionic, Mobility and Environmental Applications* (Springer Berlin Heidelberg, 2016).

[41] Y. V. Bykov, K. I. Rybakov, and V. E. Semenov, "High-temperature microwave processing of materials," *Journal of Physics D: Applied Physics* **34**, R55–R75 (2001).

[42] Y. Sun, *Adaptive and Intelligent Temperature Control of Microwave Heating Systems with Multiple Sources* (KIT Scientific Publishing, Karlsruhe, 2016).

[43] P. L. Jones and A. T. Rowley, "Dielectric Drying," *Drying Technology* **14**, 1063–1098 (1996).

[44] Z. Y. Li, R. F. Wang, and T. Kudra, "Uniformity Issue in Microwave Drying," *Drying Technology* **29**, 652–660 (2011).

[45] A. Martynenko and A. Bück, *Intelligent Control in Drying* (CRC Press, 2018).

[46] M. Hosseini, A. Kaasinen, G. Link, T. Lähivaara, and M. Vauhkonen, "LQR Control of Moisture Distribution in Microwave Drying Process Based on a Finite Element Model of Parabolic PDEs," *IFAC-PapersOnLine* **53**, 11470–11476 (2020), 21th IFAC World Congress.

[47] TOMOCON, "Tomography-controlled Microwave Drying of Porous Materials," `https://www.tomocon.eu/microwave-drying/` (2021), [Online; accessed 22-March-2022].

[48] S. Trabelsi, A. W. Kraszewski, and S. O. Nelson, "A microwave method for on-line determination of bulk density and moisture content of particulate materials," *IEEE Transactions on Instrumentation and Measurement* **47**, 127–132 (1998).

[49] S. Okamura, "Microwave Technology for Moisture Measurement," *Subsurface Sensing Technologies and Applications* **1**, 205–227 (2000).

[50] S. Trabelsi and S. O. Nelson, "Nondestructive sensing of physical properties of granular materials by microwave permittivity measurement," *IEEE Transactions on Instrumentation and Measurement* **55**, 953–963 (2006).

[51] S. Trabelsi, S. O. Nelson, and M. A. Lewis, "Microwave nondestructive sensing of moisture content in shelled peanuts independent of bulk density and with temperature compensation," *Sensing and Instrumentation for Food Quality and Safety* **3**, 114–121 (2009).

[52] S. Trabelsi, "New Calibration Algorithms for Dielectric-Based Microwave Moisture Sensors," *IEEE Sensors Letters* **1**, 1–4 (2017).

[53] K. Y. You, C. Y. Lee, Y. L. Then, S. H. C. Chong, L. L. You, Z. Abbas, and E. M. Cheng, "Precise Moisture Monitoring for Various Soil Types Using Handheld Microwave-Sensor Meter," *IEEE Sensors Journal* **13**, 2563–2570 (2013).

[54] N. Javed, A. Habib, Y. Amin, J. Loo, A. Akram, and H. Tenhunen, "Directly Printable Moisture Sensor Tag for Intelligent Packaging," *IEEE Sensors Journal* **16**, 6147–6148 (2016).

[55] A. Abubakar, P. M. van den Berg, and S. Y. Semenov, "TWO- AND THREE-DIMENSIONAL ALGORITHMS FOR MICROWAVE IMAGING AND INVERSE SCATTERING," *Journal of Electromagnetic Waves and Applications* **17**, 209–231 (2003).

[56] Y. Zhong, M. Lambert, D. Lesselier, and X. Chen, "A New Integral Equation Method to Solve Highly Nonlinear Inverse Scattering Problems," *IEEE Transactions on Antennas and Propagation* **64**, 1788–1799 (2016).

[57] Z. Wei and X. Chen, "Physics-Inspired Convolutional Neural Network for Solving Full-Wave Inverse Scattering Problems," *IEEE Transactions on Antennas and Propagation* **67**, 6138–6148 (2019).

[58] Y. Sun, Z. Xia, and U. S. Kamilov, "Efficient and accurate inversion of multiple scattering with deep learning," *Optics Express* **26**, 14678–14688 (2018).

[59] T. Lähivaara, R. Yadav, G. Link, and M. Vauhkonen, "Estimation of Moisture Content Distribution in Porous Foam Using Microwave Tomography With Neural Networks," *IEEE Transactions on Computational Imaging* **6**, 1351–1361 (2020).

[60] Y. Zhou, Y. Zhong, Z. Wei, T. Yin, and X. Chen, "An Improved Deep Learning Scheme for Solving 2-D and 3-D Inverse Scattering Problems," *IEEE Transactions on Antennas and Propagation* **69**, 2853–2863 (2021).

[61] Z. Ma, K. Xu, R. Song, C.-F. Wang, and X. Chen, "Learning-Based Fast Electromagnetic Scattering Solver Through Generative Adversarial Network," *IEEE Transactions on Antennas and Propagation* **69**, 2194–2208 (2021).

[62] R. Guo, T. Shan, X. Song, M. Li, F. Yang, S. Xu, and A. Abubakar, "Physics Embedded Deep Neural Network for Solving Volume Integral Equation: 2D Case," *IEEE Transactions on Antennas and Propagation* 1-1 (2021).

[63] L. Guo, G. Song, and H. Wu, "Complex-Valued Pix2pix—Deep Neural Network for Nonlinear Electromagnetic Inverse Scattering," *Electronics* **10** (2021).

[64] Y. Sanghvi, Y. N. G. B. Kalepu, and U. Khankhoje, "Embedding Deep Learning in Inverse Scattering Problems," *IEEE Transactions on Computational Imaging* (in press).

[65] Z. Lin, R. Guo, M. Li, A. Abubakar, T. Zhao, F. Yang, and S. Xu, "Low-Frequency Data Prediction With Iterative Learning for Highly Nonlinear Inverse Scattering Problems," *IEEE Transactions on Microwave Theory and Techniques* 1-1 (2021).

[66] L. Li, L. G. Wang, F. L. Teixeira, C. Liu, A. Nehorai, and T. J. Cui, "Deep-NIS: Deep Neural Network for Nonlinear Electromagnetic Inverse Scattering," *IEEE Transactions on Antennas and Propagation* **67**, 1819–1825 (2019).

[67] Z. Wei and X. Chen, "Deep-Learning Schemes for Full-Wave Nonlinear Inverse Scattering Problems," *IEEE Transactions on Geoscience and Remote Sensing* 1-12 (2018).

[68] I. V. Lindell, *Methods for Electromagnetic Field Analysis* (Wiley-IEEE Press, 1992).

[69] J. Jin, *The Finite Element Method in Electromagnetics* (Wiley, 2015).

[70] A. Kirsch and F. Hettlich, *The Mathematical Theory of Time-Harmonic Maxwell's Equations: Expansion-, Integral-, and Variational Methods* (Springer International Publishing, 2014).

[71] J. Kong, *Electromagnetic Wave Theory* (Wiley, 1986).

[72] R. Garg, *Analytical and Computational Methods in Electromagnetics* (Artech House, 2008).

[73] D. Dudley, *Mathematical Foundations for Electromagnetic Theory* (Wiley, 1994).

[74] R. Rook, *Notes on solving Maxwell equations, part 2, Green's function for stratified media* (Technische Universiteit Eindhoven, 2011).

[75] H. Eom, *Electromagnetic Wave Theory for Boundary-Value Problems: An Advanced Course on Analytical Methods* (Springer Berlin Heidelberg, 2013).

[76] M. Ostadrahimi, A. Zakaria, J. LoVetri, and L. Shafai, "A Near-Field Dual Polarized (TE–TM) Microwave Imaging System," *IEEE Transactions on Microwave Theory and Techniques* **61**, 1376–1384 (2013).

[77] W. C. Chew, *Waves and Fields in Inhomogenous Media* (IEEE Press, 1995).

[78] S. Caorsi, G. L. Gragnani, and M. Pastorino, "Two-dimensional microwave imaging by a numerical inverse scattering solution," *IEEE Transactions on Microwave Theory and Techniques* **38**, 981–980 (1990).

[79] S. Sadeghi, K. Mohammadpour-Aghdam, R. Faraji-Dana, and R. J. Burkholder, "A DORT-Uniform Diffraction Tomography Algorithm for Through-the-Wall Imaging," *IEEE Transactions on Antennas and Propagation* **68**, 3176–3183 (2020).

[80] R. C. Janalizadeh and B. Zakeri, "A Source-Type Best Approximation Method for Imaging Applications," *IEEE Antennas and Wireless Propagation Letters* **15**, 1707–1710 (2016).

[81] D. Colton and R. Kress, *Inverse Acoustic and Electromagnetic Scattering Theory* (Berlin, Germany:Springer-Verlag, 1998).

[82] R. Yadav, M. Vauhkonen, G. Link, S. Betz, and T. Lähivaara, "Microwave tomography for estimating moisture content distribution in porous foam using neural networks," in *2020 14th European Conference on Antennas and Propagation (EuCAP)* (2020), pp. 1–5.

[83] R. Yadav, A. Omrani, M. Vauhkonen, G. Link, and T. Lähivaara, "Microwave Tomography for Moisture Level Estimation Using Bayesian Framework," in *2021 15th European Conference on Antennas and Propagation (EuCAP)* (2021), pp. 1–5.

[84] A. Omrani, R. Yadav, G. Link, M. Vauhkonen, T. Lähivaara, and J. Jelonnek, "A Combined Microwave Imaging Algorithm for Localization and Moisture Level Estimation in Multilayered Media," in *2021 15th European Conference on Antennas and Propagation (EuCAP)* (2021), pp. 1–5.

[85] A. Omrani, M. Moghadasi, and M. Dehmollaian, "Localisation and permittivity extraction of an embedded cylinder using decomposition of the time reversal operator," *IET Microwaves, Antennas Propagation* **14**, 851–859(8) (2020).

[86] A. Omrani, G. Link, and J. Jelonnek, "A Multistatic Uniform Diffraction Tomographic Algorithm for Real-Time Moisture Detection," in *2020 IEEE Asia-Pacific Microwave Conference (APMC)* (2020), pp. 437–439.

[87] C.-T. Tai, *Dyadic Green functions in electromagnetic theory* (IEEE, 1994).

[88] J. Richmond, "Scattering by a dielectric cylinder of arbitrary cross section shape," *IEEE Transactions on Antennas and Propagation* **13**, 334–341 (1965).

[89] S. Soldatov, T. Kayser, G. Link, T. Seitz, S. Layer, and J. Jelonnek, "Microwave cavity perturbation technique for high-temperature dielectric measurements," in *2013 IEEE MTT-S International Microwave Symposium Digest (MTT)* (2013), pp. 1–4.

[90] C. Rasmussen and C. Williams, *Gaussian Processes for Machine Learning* (The MIT Press, 2006).

[91] O. M. Bucci, N. Cardace, L. Crocco, and T. Isernia, "Degree of nonlinearity and a new solution procedure in scalar two-dimensional inverse scattering problems," *Journal of the Optical Society of America A* **18**, 1832–1843 (2001).

[92] M. T. Bevacqua and T. Isernia, "An Effective Rewriting of the Inverse Scattering Equations via Green's Function Decomposition," *IEEE Transactions on Antennas and Propagation* **69**, 4883–4893 (2021).

[93] A. Abubakar, P. van den Berg, and S. Semenov, "A robust iterative method for Born inversion," *IEEE Transactions on Geoscience and Remote Sensing* **42**, 342–354 (2004).

[94] J. Kaipio and E. Somersalo, "Statistical inverse problems: Discretization, model reduction and inverse crimes," *Journal of Computational and Applied Mathematics* **198**, 493–504 (2007).

[95] J. Adler and O. Öktem, "Solving ill-posed inverse problems using iterative deep neural networks," *Inverse Problems* **33**, 124007 (2017).

[96] D. P. Kingma and J. Ba, "Adam: A Method for Stochastic Optimization," *ArXiv e-prints* (2014).

[97] M. Abadi, A. Agarwal, P. Barham, E. Brevdo, Z. Chen, C. Citro, G. S. Corrado, A. Davis, J. Dean, M. Devin, S. Ghemawat, I. Goodfellow, A. Harp, G. Irving, M. Isard, Y. Jia, R. Jozefowicz, L. Kaiser, M. Kudlur, J. Levenberg, D. Mané, R. Monga, S. Moore, D. Murray, C. Olah, M. Schuster, J. Shlens, B. Steiner, I. Sutskever, K. Talwar, P. Tucker, V. Vanhoucke, V. Vasudevan, F. Viégas, O. Vinyals, P. Warden, M. Wattenberg, M. Wicke, Y. Yu, and X. Zheng, "TensorFlow: Large-Scale Machine Learning on Heterogeneous Systems," (2015), Software available from tensorflow.org.

[98] M. Ostadrahimi, P. Mojabi, C. Gilmore, A. Zakaria, S. Noghanian, S. Pistorius, and J. LoVetri, "Analysis of Incident Field Modeling and Incident/Scattered Field Calibration Techniques in Microwave Tomography," *IEEE Antennas and Wireless Propagation Letters* **10**, 900–903 (2011).

[99] J. Kaipio and E. Somersalo, *Statistical and Computational Inverse Problems* (Springer-Verlag, 2005).

[100] D. Calvetti and E. Somersalo, "Inverse problems: From regularization to Bayesian inference," *WIREs Computational Statistics* **10**, e1427 (2018).

[101] S. M. Kay, *Fundamentals of Statistical Signal Processing: Estimation Theory* (Prentice-Hall, Inc., USA, 1993).

[102] B. Picinbono, "Second-order complex random vectors and normal distributions," *IEEE Transactions on Signal Processing* **44**, 2637–2640 (1996).

[103] R. Yadav, A. Omrani, M. Vauhkonen, G. Link, and T. Lähivaara, "Microwave tomography for moisture level estimation using Bayesian framework," in *2021 15th European Conference on Antennas and Propagation (EuCAP)* (2021), pp. 1–5.

[104] A. Omrani, R. Yadav, M. Vauhkonen, G. Link, T. Lähivaara, and J. Jelonnek, "A combined microwave imaging algorithm for localization and moisture level estimation in multilayered media," in *2021 15th European Conference on Antennas and Propagation (EuCAP)* (2021), pp. 1–5.

[105] G. Ferraiuolo and V. Pascazio, "The effect of modified Markov random fields on the local minima occurrence in microwave imaging," *IEEE Transactions on Geoscience and Remote Sensing* **41**, 1043–1055 (2003).

[106] R. Autieri, G. Ferraiuolo, and V. Pascazio, "Bayesian Regularization in Nonlinear Imaging: Reconstructions From Experimental Data in Nonlinearized Microwave Tomography," *IEEE Transactions on Geoscience and Remote Sensing* **49**, 801–813 (2011).

[107] A. P. Dempster, N. M. Laird, and D. B. Rubin, "Maximum Likelihood from Incomplete Data via the EM Algorithm," *Journal of the Royal Statistical Society. Series B (Methodological)* **39**, 1–38 (1977).

[108] M. A. Islam, A. Kiourti, and J. L. Volakis, "A Novel Method to Mitigate Real–Imaginary Image Imbalance in Microwave Tomography," *IEEE Transactions on Biomedical Engineering* **67**, 1328–1337 (2020).

[109] M. Ostadrahimi, P. Mojabi, A. Zakaria, J. LoVetri, and L. Shafai, "Enhancement of Gauss–Newton Inversion Method for Biological Tissue Imaging," *IEEE Transactions on Microwave Theory and Techniques* **61**, 3424–3434 (2013).

[110] P. Mojabi and J. LoVetri, "A Prescaled Multiplicative Regularized Gauss-Newton Inversion," *IEEE Transactions on Antennas and Propagation* **59**, 2954–2963 (2011).

[111] H.-O. Peitgen and D. Saupe, eds., *The Science of Fractal Images* (Springer-Verlag, Berlin, Heidelberg, 1988).

[112] C. Eyraud, A. Litman, A. Hérique, and W. Kofman, "Microwave imaging from experimental data within a Bayesian framework with realistic random noise," *Inverse Problems* **25**, 024005 (2009).

[113] P. Meaney, A. Golnabi, N. Epstein, S. Geimer, M. Fanning, J. Weaver, and K. Paulsen, "Integration of microwave tomography with magnetic resonance for improved breast imaging," *Medical physics* **40**, 103101 (2013).

[114] N. Bayat and P. Mojabi, "Incorporating Spatial Priors in Microwave Imaging via Multiplicative Regularization," *IEEE Transactions on Antennas and Propagation* **68**, 1107–1118 (2020).

[115] A. H. Golnabi, P. M. Meaney, and K. D. Paulsen, "Tomographic Microwave Imaging With Incorporated Prior Spatial Information," *IEEE Transactions on Microwave Theory and Techniques* **61**, 2129–2136 (2013).

[116] D. Kurrant, A. Baran, J. LoVetri, and E. Fear, "Integrating prior information into microwave tomography Part 1: Impact of detail on image quality," *Medical Physics* **44**, 6461–6481 (2017).

[117] D. Kurrant and E. Fear, "Defining regions of interest for microwave imaging using near-field reflection data," *IEEE Transactions on Microwave Theory and Techniques* **61**, 2137–2145 (2013).

[118] I. Catapano, L. Crocco, M. D'Urso, and T. Isernia, "On the Effect of Support Estimation and of a New Model in 2-D Inverse Scattering Problems," *IEEE Transactions on Antennas and Propagation* **55**, 1895–1899 (2007).

[119] F. M. Saraskanroud and I. Jeffrey, "A Comparison of Time-Domain and Frequency-Domain Microwave Imaging of Experimental Targets," *IEEE Transactions on Computational Imaging* **7**, 611–623 (2021).

[120] F. Mahdinezhad Saraskanroud and I. Jeffrey, "Hybrid Approaches in Microwave Imaging using Quantitative Time- and Frequency-Domain Algorithms," *IEEE Transactions on Computational Imaging* 1-1 (2022).

[121] N. Abdollahi, I. Jeffrey, and J. LoVetri, "Improved Tumor Detection via Quantitative Microwave Breast Imaging Using Eigenfunction-Based Prior," *IEEE Transactions on Computational Imaging* **6**, 1194–1202 (2020).

[122] A. Omrani, R. Yadav, G. Link, and J. Jelonnek, "A Multistatic Uniform Diffraction Tomography Algorithm for Microwave Imaging in Multilayered Media for Microwave Drying," *IEEE Transactions on Antennas and Propagation* 1-1 (2022).

[123] K. Ren and R. J. Burkholder, "A Uniform Diffraction Tomographic Imaging Algorithm for Near-Field Microwave Scanning Through Stratified Media," *IEEE Transactions on Antennas and Propagation* **64**, 5198–5207 (2016).

[124] S. Sadeghi, K. Mohammadpour-Aghdam, R. Faraji-Dana, and R. J. Burkholder, "A DORT-Uniform Diffraction Tomography Algorithm for Through-the-Wall Imaging," *IEEE Transactions on Antennas and Propagation* **68**, 3176–3183 (2020).

[125] V. Khoshdel, M. Asefi, A. Ashraf, and J. LoVetri, "Full 3D Microwave Breast Imaging Using a Deep-Learning Technique," *Journal of Imaging* **6** (2020).

[126] L. Zhang, K. Xu, R. Song, X. Ye, G. Wang, and X. Chen, "Learning-Based Quantitative Microwave Imaging With a Hybrid Input Scheme," *IEEE Sensors Journal* **20**, 15007–15013 (2020).

[127] M. Abdar, F. Pourpanah, S. Hussain, D. Rezazadegan, L. Liu, M. Ghavamzadeh, P. Fieguth, X. Cao, A. Khosravi, U. R. Acharya, V. Makarenkov, and S. Nahavandi, "A review of uncertainty quantification in deep learning: Techniques, applications and challenges," *Information Fusion* **76**, 243–297 (2021).

[128] P. Meaney, K. Paulsen, S. Geimer, S. Haider, and M. Fanning, "Quantification of 3-D field effects during 2-D microwave imaging," *IEEE Transactions on Biomedical Engineering* **49**, 708–720 (2002).

[129] J. P. Kaipio, T. Huttunen, T. Luostari, T. Lähivaara, and P. B. Monk, "A Bayesian approach to improving the Born approximation for inverse scattering with high-contrast materials," *Inverse Problems* **35**, 084001 (2019).

[130] A. Omrani, R. Yadav, G. Link, T. Lähivaara, M. Vauhkonen, and J. Jelonnek, "An Electromagnetic Time-Reversal Imaging Algorithm for Moisture Detection in Polymer Foam in an Industrial Microwave Drying System," *Sensors* **21** (2021).

Paper **I**

R. Yadav, A. Omrani, G. Link, M. Vauhkonen
and T. Lähivaara,

**"Microwave Tomography Using Neural Networks for
Its Application in an Industrial Microwave Drying
System"**

Article

Microwave Tomography Using Neural Networks for Its Application in an Industrial Microwave Drying System

Rahul Yadav [1,*] , **Adel Omrani** [2] , **Guido Link** [2] , **Marko Vauhkonen** [1] and **Timo Lähivaara** [1]

1. Department of Applied Physics, University of Eastern Finland, FI-70210 Kuopio, Finland; marko.vauhkonen@uef.fi (M.V.); timo.lahivaara@uef.fi (T.L.)
2. Institute for Pulsed Power and Microwave Technology, Karlsruhe Institute of Technology (KIT), 76133 Karlsruhe, Germany; adel.hamzekalaei@kit.edu (A.O.); guido.link@kit.edu (G.L.)
* Correspondence: rahuly@uef.fi

Abstract: The article presents an application of microwave tomography (MWT) in an industrial drying system to develop tomographic-based process control. The imaging modality is applied to estimate moisture distribution in a polymer foam undergoing drying process. Our Leading challenges are fast data acquisition from the MWT sensors and real-time image reconstruction of the process. Thus, a limited number of sensors are chosen for the MWT and are placed only on top of the polymer foam to enable fast data acquisition. For real-time estimation, we present a neural network-based reconstruction scheme to estimate moisture distribution in a polymer foam. Training data for the neural network is generated using a physics-based electromagnetic scattering model and a parametric model for moisture sample generation. Numerical data for different moisture scenarios are considered to validate and test the performance of the network. Further, the trained network performance is evaluated with data from our developed prototype of the MWT sensor array. The experimental results show that the network has good accuracy and generalization capabilities.

Keywords: microwave drying; moisture content distribution; microwave tomography; inverse problems; neural networks

1. Introduction

Controlled/localised heating in industrial microwave oven [1,2] is paramount to address hot-spot formation and thermal runaway issues [3]. As a consequence, system efficiency and processed product quality may improve. Presently, we are working on a type of microwave oven technology called HEPHAISTOS, as shown in Figure 1. The system is characterized by hexagonal geometry [4] for the cavity that supports a very high electromagnetic field homogeneity. Its principal areas of applications are in material processing such as thermal curing of fiber composites and drying of porous foams. Specifically, during drying of a porous polymer foam, thermal runaway and hot-spot formation may occur [5,6]. Such situations may lead to low-quality processing and may even damage the industrial unit in case a fire is kindled in the foam. Therefore, automatic online control of power sources (magnetrons) to obtain a selective heating rate at each stage of the drying process is one option to eliminate these problems. To apply such precise control of power sources, non-invasive in situ measurement of the unknown distribution of moisture, especially dominant wet-spots, inside the material is required. The infrared temperature sensors integrated with the microwave drying systems are capable of giving information only on the surface of the material. That is not sufficient to provide efficient control of microwave sources. Thus, integration of microwave tomography (MWT) imaging modality operating in X-band range [7] (from 8 GHz to 12 GHz) with the drying system is proposed (see number Tag 4 in Figure 1) to estimate the moisture content distribution in a polymer foam. Based on the MWT tomographic output, an intelligent control strategy for power sources can be derived. Preliminary work in this direction is reported in [8] by the authors.

Industrial process tomography based on microwave sensors for various applications are reported in [9,10]. The specific use-case of microwave sensor technology for moisture measurements in a sample are given in [11–17]; but they are limited in providing moisture information on the surface or in a small sample size but not the volumetric information as required for our purpose.
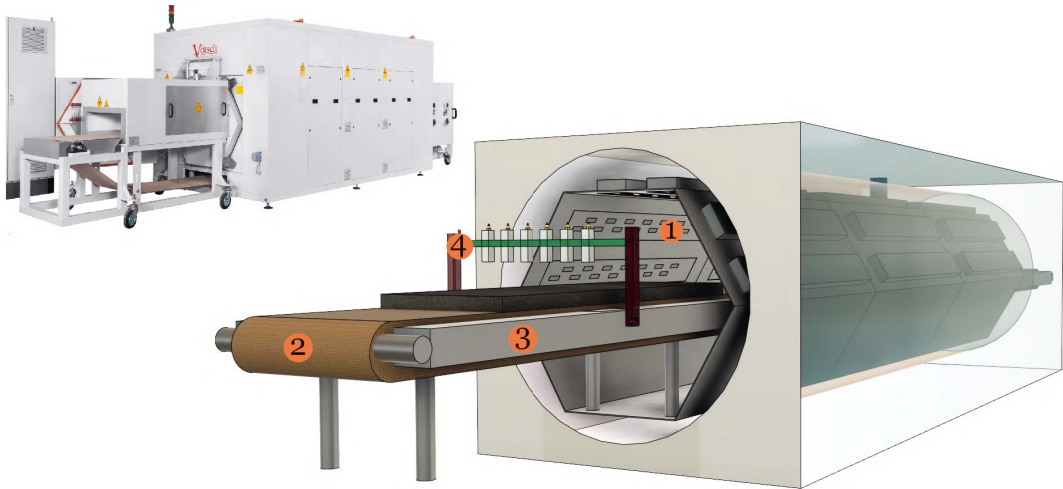
Figure 1. Left: view of the HEPHAISTOS microwave oven system. **Right**: schematic showing the main modules of the oven which are represented by numbers tag 1, 2, 3, and 4. Tag 1 is high power microwave waveguide antenna, Tag 2 is the conveyor belt, and Tag 3 is the metal plate. MWT setup with waveguide antenna is represented by Tag 4. The foam is shown as dark gray matter and placed on the conveyor belt.

For MWT, real-time image reconstruction is critical to provide a fast input response for the control system. In addition, the inverse scattering problem that we are solving is severely ill-posed due to the large object size and inhomogeneous profile. Thus, applying iterative optimization-based methods like Levenberg–Marquardt [18], contrast source inversion, and subspace-based optimization methods [19] are time-consuming. An attractive approach to fulfill the real-time estimation requirement is to use neural networks [20,21]. The first implementation of neural networks, to the best of our knowledge, in solving an inverse problem in electromagnetics where material properties of multilayered media is estimated was presented in [22]. In [23,24], artificial neural network is employed for determining the moisture content in wheat and moisture content of commercially important biomass, respectively.

Recent developments in the use of neural networks for solving general microwave imaging problem are detailed in [25–30]. In [31], a connection between the optimization framework and neural network is established and tested to solve nonlinear inverse scattering problems. However, they are limited to sparse target recovery with full-angle sensor configuration and a large number of measurements. In this work, an MWT configuration with antennas located only on top is chosen as a setup to support fast data acquisition. Secondly, our network is trained using the smoothness parameter model to represent possible moisture distribution scenarios and is capable of even generalizing sparse targets as shall be demonstrated by the experimental results. Using ideas from our preliminary studies [32–35], we build a comprehensive synthetic dataset consisting of different moisture content distribution scenarios and the corresponding scattered electric field responses using two-dimensional (2-D) method-of-moment formulation. Once the selected network architecture is trained using this dataset, it is applied to recover the moisture content distribution (in terms of dielectric constant) in real-time. The performance of trained network is

validated with the numerical MWT data for different moisture scenarios. Further, the network is tested on the experimental data from the MWT setup integrated with the drying unit. Results presented shows that neural network approach can successfully estimate the moisture content in real-time.

The paper is organized as follows: The forward model for MWT problem and its formulation is detailed in Section 2. Furthermore, Section 2 also details the parametric model for generation of moisture distribution. Section 3 details the neural network based approach in the MWT and numerical results are presented. The experimental setup of the MWT is detailed in Section 4 and performance of the neural network with the experimental data is tested. Discussion and concluding remarks are given in Section 5.

2. Problem Formulation

To generate the numerical dataset for the neural network, we begin our discussion by first unveiling the scattering model of the problem. With reference to the MWT measurement schematic shown in Figure 1, we chose to illustrate the scattering model in the context of its 2-D configuration. The 2-D configuration is chosen instead of 3-D model as to decrease the overall computational load for generating the dataset.

2.1. Forward Model

The 2-D cross-section of the MWT setup is shown in Figure 2 with multistatic measurement configuration. In the figure, we consider a two-dimensional foam domain $\Omega_{\text{foam}} = [-15, \ 15] \times [0, \ 7.6]$ cm with inhomogenous relative dielectric constant $\epsilon_r = \epsilon_r' - j\epsilon_r''$. The foam is placed on the metal plate (as shown in Tag 4 in Figure 1) which is modeled here as perfect electric conductor (PEC) plane and surrounded by background domain Ω consisting of air with $\epsilon_r = 1 - j0$. For this 2-D numerical study, the waveguide antennas are modeled as a *z*-oriented electric line source [36]; 7 such line sources are placed in a transceiver mode at a distance of 5 cm from the top surface of the foam.
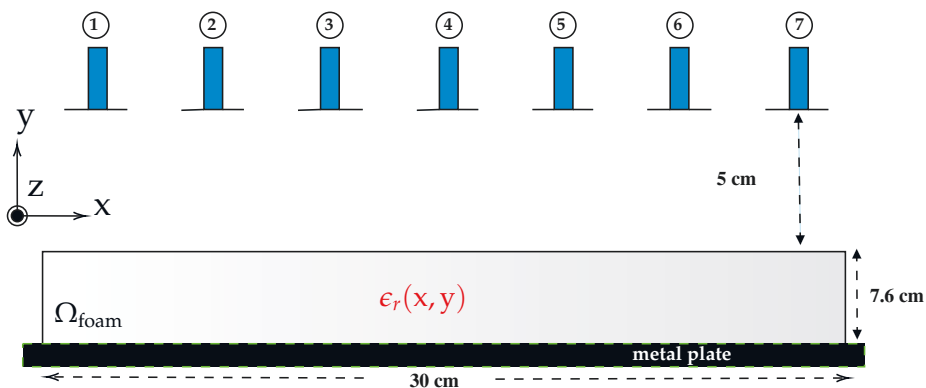
Figure 2. 2-D schematic of the MWT setup with waveguide antennas denoted by number from 1, 2, . . . 7.

In general, the scattered electric field under the illumination of time-harmonic (time convention $e^{-j\omega t}$ with angular frequency ω is used and suppressed) transverse magnetic (TM) *z*-polarized incident field is governed by the following coupled scalar volume integral Equations (VIEs) [37–41]

$$E_{\text{sct}}(r) = k^2 \int_{\Omega_{\text{foam}}} G(r, r') \big(\epsilon_r(r') - 1 \big) E(r') dr',$$

$$\forall r \in \Omega, \ r' \in \Omega_{\text{foam}}. \tag{1}$$

The term E_{sct} is the scattered electric field. The wavenumber of the background medium is denoted by k. The term $G(r, r')$ is the free-space Green's function. The source and the observation points are denoted by the position vectors $r \mapsto (x, y)$ and $r' \mapsto (x', y')$, respectively. The term E is the total electric field inside the scattering object and is given as

$$E(r) = E_{inc}(r) + k^2 \int_{\Omega_{foam}} G(r, r')(\epsilon_r(r') - 1)E(r')dr',$$

$$\forall r, r' \in \Omega_{foam},$$

(2)

where E_{inc} is the incident electric field from the line-source. The effects of the conducting plane are included in the 2-D free-space Green's function of the VIEs by the use of half-space Green's function [42]. It is defined using image theory principle [43] where an image source is introduced to account for the reflections from the surface of the conducting plane and thus the conducting plane can be removed. The image source point (denoted here as x_{im} and y_{im}) must have the same magnitude as the actual source, its phase must be 180 degree out of phase from the actual source and it must be placed below the conducting plane at a depth $y_{im} = -y$. Such a system configuration does lead to zero tangential electric field [44] along the x-direction. The half-space Green's function includes both the primary contribution $G_T(r, r')$, which is the free-space Green's function, and the secondary contribution $G_R(r, r'_{im})$ due to the image source and denoted as

$$G(r, r') = G_T(r, r') + G_R(r_{im}, r').$$

(3)

Therefore, the scattered electric field above the conducting plane (i.e., upper half-space $y > 0$) is equal to

$$E_{sct}(r) = k^2 \int_{\Omega_{foam}} G_T(r, r')(\epsilon_r(r') - 1)E(r')dr'$$

$$+ k^2 \int_{\Omega_{foam}} G_R(r_{im}, r')(\epsilon_r(r') - 1)E(r')dr'. \quad (4)$$

Given the integral equation for the scattered electric field and total electric field, we resorted to discrete dipole approximation with pulse basis and point matching technique, i.e., method-of-moments (MoM) [45] for its numerical solution. In doing so, the foam domain is discretized into n cells with dimensions denoted as Δ, so that the dielectric constant and the total electric field are essentially constant over each cell. The unknown total electric field inside the domain can be represented using sub-domain pulse-basis function with unknown weight w as

$$E(r) = \sum_{l=1}^{n} w_l E_l(r).$$

(5)

Here, the discretized electric field E_l is defined as

$$E_l(r) = \begin{cases} 1 & \forall (x, y) \in \text{cell } l \\ 0 & \text{otherwise} \end{cases}$$

(6)

Then, Equation (2) is written as

$$\sum_{l=1}^{n} w_l E_l(r) = E_{inc}(r) - \frac{jk^2}{4} \sum_{l=1}^{n} (\epsilon_{r_l} - 1)w_l E_l(r) \iint_{\Delta_l} H_0^2(r, r')dr' +$$

$$\frac{jk^2}{4} \sum_{l=1}^{n} (\epsilon_{r_l} - 1)w_l E_l(r) \iint_{\Delta_l} H_0^2(r_{im}, r')dr', \quad (7)$$

where H_0^2 is Hankel function of second kind and zero order. Further, after dot product, denoted by the operator $\langle \cdot \rangle$, of Equation (7) with the test function $E_m(r)$, we obtain

$$\sum_{l=1}^{n} w_l \langle E_m(r), E_l(r) \rangle = \langle E_m(r), E_{\mathrm{inc}}(r) \rangle - \frac{jk^2}{4} \sum_{l=1}^{n} (\epsilon_{r_l} - 1) w_l \langle E_m(r), E_l(r) \rangle \iint_{\Delta_l} H_0^2(r, r') dr'$$

$$+ \frac{jk^2}{4} \sum_{l=1}^{n} (\epsilon_{r_l} - 1) w_l \langle E_m(r), E_l(r) \rangle \iint_{\Delta_l} H_0^2(r_{\mathrm{im}}, r') dr'. \quad (8)$$

Applying point collocation, i.e., choosing the test function as $E_m(r) = \delta_m(r)$ where δ is the delta function, we obtain the following matrix equation of the form

$$\sum_{l=1}^{n} Z_{ml} w_l = E_{\mathrm{inc}_m} = \langle \delta_m(r), E_{\mathrm{inc}}(r) \rangle, \quad (9)$$

where

$$Z_{ml} = \langle \delta_m(r), E_l(r) \rangle + \frac{jk^2}{4} (\epsilon_{r_l} - 1) \langle \delta_m(r), E_l(r) \rangle \iint_{\Delta_l} H_0^2(r, r') dr'$$

$$- \frac{jk^2}{4} (\epsilon_{r_l} - 1) \langle \delta_m(r), E_l(r) \rangle \iint_{\Delta_l} H_0^2(r_{\mathrm{im}}, r') dr'.$$

The approximate solution of the surface integral in Equation (8), following [46] become

$$\frac{jk^2}{4} \iint_{\Delta_l} H_0^2(r, r') dr' = \begin{cases} \frac{j}{2} \left[\pi k a H_1^2(ka) - 2j \right], & \forall\, m = l \\ \frac{j\pi ka}{2} J_1(ka) H_0^2\left(k\sqrt{(x_m - x_l)^2 + (y_m - y_l)^2} \right), & \forall\, m \neq l \end{cases}$$

where H_1^2 is the Hankel function of second kind and first order, a is the radius of equivalent circular region having same area of the discretized cell, and J_1 is the Bessel function of first kind. To solve for the system of linear equations in Equation (9), generalized minimal residual method (GMRES) [47] is employed. Upon calculation of the unknown weights, the scattered electric field is evaluated at the transceiver points as

$$E_{\mathrm{sct}}(r) = -j \frac{\pi k}{2} \sum_{l=1}^{n} (\epsilon_{r_l} - 1) w_l a_l J_1(ka_l) \left[H_0^2\left(k\sqrt{(x - x_l)^2 + (y - y_l)^2} \right) - H_0^2\left(k\sqrt{(x_{\mathrm{im}} - x_l)^2 + (y_{\mathrm{im}} - y_l)^2} \right) \right]. \quad (10)$$

Note that in Equation (7), the term E_{inc} contains both the transmitted signal and the reflected signal from the PEC in the absence of the foam.

2.2. Parametric Model for Moisture Distribution

The dielectric values used to represent moisture variations are generated numerically, based on the dielectric characterization of the polymer foam in laboratory environment. In the characterization, cavity perturbation method was used for dry sample and measurement at different moisture levels were performed with samples that cover all the cross section of a WR340 waveguide and using transmission reflection method [48]. The moisture content is calculated based on the *wet-basis*, i.e.,

$$M = \frac{W_m - W_d}{W_m} \times 100, \quad (11)$$

where M is the moisture percentage, W_m is the weight of the foam sample after adding the water, and W_d is the weight of the dry sample. At the first step, we obtained the dielectric constant associated with the 0% moisture level. Then, a certain amount of water is added manually and the dielectric constant is recorded in each level. Thus, a relationship between the *wet-basis* moisture content M_{meas} and its corresponding real part and the imaginary part of the dielectric value is obtained and given as

$$\theta = \bar{a}_\theta \exp\left(\bar{b}_\theta M_{\text{meas}}\right), \tag{12}$$

where $\theta = \{\epsilon'_r, \, \epsilon''_r\}$ denotes the material parameters. Numerical values for $\bar{a}_\theta$ and $\bar{b}_\theta$ are given in Table 1 where the error bounds for the fitted coefficients are defined by δ_{a_θ} and δ_{b_θ}. Based on (12), the real part of relative dielectric constant vary in the range of 1.164–3.255 and imaginary part vary between 0.017–0.276 for *wet-basis* moisture content from 0% to 90%, respectively.

Table 1. Material model parameters.

	$\bar{a}_\theta$	δ_{a_θ}	$\bar{b}_\theta$	δ_{b_θ}
ϵ'_r	1.085	0.01591	0.01256	0.00062
ϵ''_r	0.03021	0.0025	0.02249	0.0009

Further, we assume that the moisture field variation M in the foam is smooth. To generate such a random field, we utilise an anisotropic covariance structure C with its elements calculated as [49]

$$C_{ij} = \exp\left\{ -\frac{1}{2} \left(\frac{\|x_i - x_j\|^2}{l_x^2} + \frac{\|y_i - y_j\|^2}{l_y^2} \right) \right\}. \tag{13}$$

Here, $i, j = 1, \ldots, N_n$ and l_x, l_y are the characteristic length components. N_n denotes the number of pixels. In practice, the characteristic lengths affect the moisture distribution in x, and y directions. To generate simulated moisture samples, the uncertainties in the dielectric characterization is also considered, and hence Equation (12) is replaced by

$$\theta = a_\theta \exp\left(b_\theta M\right), \tag{14}$$

where a_θ, b_θ are random variables such that $a_\theta \sim \mathcal{U}(\bar{a}_\theta - \delta_{a_\theta}, \bar{a}_\theta + \delta_{a_\theta})$ and $b_\theta \sim \mathcal{U}(\bar{b}_\theta - \delta_{b_\theta}, \bar{b}_\theta + \delta_{b_\theta})$, where $\mathcal{U}$ denotes the uniform distribution. Numerical values for δ_{a_θ} and δ_{b_θ} are given in Table 1. The moisture content distribution in each sample M can be expressed as

$$M = M^* \mathbb{1} + \delta_M L Z, \tag{15}$$

where $\mathbb{1}$ is an all-ones vector, L is the lower triangular matrix of the Cholesky factorization of the covariance C, Z is a standard normal random vector, M^* and δ_M are the mean and standard deviation of the moisture content field, respectively. A pseudo-code for generating a sample is given below.

In Algorithm 1, the terms $x_{\min} = 2\,\text{cm}$, $x_{\max} = 30\,\text{cm}$, $y_{\min} = 2\,\text{cm}$, and $y_{\max} = 7.6\,\text{cm}$ denote the chosen minimum and maximum dimensions in the x and y directions of the foam domain, respectively. $\mathcal{U}$ denotes the uniform distribution. Four randomized draws of moisture distribution are shown in Figure 3.

Algorithm 1 Pseudocode for generating the moisture distribution. Note that a small diagonal component is added in matrix C to ensure the positive definiteness.

1: $M^* \sim \mathcal{U}(0, 50)$ %, $\delta_M \sim \mathcal{U}(2, 20)$ %
2: $c_x \sim \mathcal{U}(x_{\min}, x_{\max})$, $c_y \sim \mathcal{U}(y_{\min}, y_{\max})$
3: $C = \text{AnisotropicCovariance}(c_x, c_y, x, y)$
4: $L = \text{Cholesky}(C)$
5: $M = M^* \text{ ones}(N_n) + \delta_M L \text{ randn}(N_n)$
6: Calculate ϵ'_r, ϵ''_r using Equation (14)
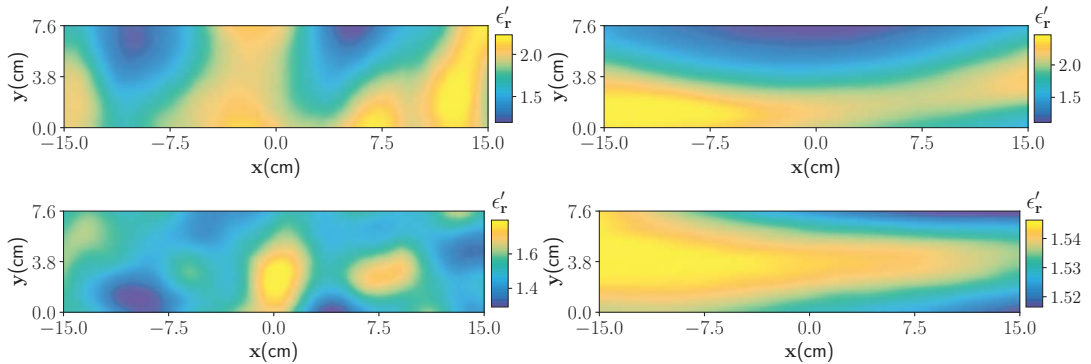
Figure 3. Four realisation of the moisture distribution with different correlation lengths, and mean and standard deviation parameters. In the top right figure the characteristic parameter are $l_x = 3$ cm and $l_y = 7$ cm, and for the top left figure characteristic parameter are $l_x = 18$ cm and $l_y = 4$ cm. Wet-spots ($l_x = 3$ cm, and $l_y = 3$ cm) and nearly homogeneous moisture distribution ($l_x = 30$ cm, $l_y = 7$ cm, and $\delta_M = 2$%) are shown in bottom left and right figures, respectively.

3. Inverse Problem: Convolutional Neural Network

In this study, a convolutional neural networks (CNN) is applied to estimate the moisture distribution of porous foam from scattered electric field data. The CNN $H_{w,b}(E_{\text{sct}})$ is trained to map from an input space $E_{\text{sct}} \in \mathbb{R}^{7 \times 7 \times 2}$ to $\Theta \in \mathbb{R}^{300 \times 1}$ (vectorized moisture content distribution in terms of real part of the dielectric constant ϵ'_r). The network architecture used in this work comprises two convolution layers and two fully connected layers. The network architecture is shown pictorially in Figure 4. The input layer consists of two channels where the real part (channel 1) and imaginary part (channel 2) of the complex valued scattered electric data, i.e., E_{sct} are given as an input. The convolutional layers $L = 1$ and $L = 2$ have 20 and 30 channels with non-linear Rectified Linear Unit (ReLU) activation function and spatial filter of size 3×3 is chosen for both the layers. The fully connected layer $L = 3$ has an output of size 340×1. As for the estimation of $\epsilon'_r(x, y)$, an adequate resolution of the moisture distribution field of around $x \times y = 1$ cm $\times$ 0.76 cm is chosen. Thus, the output layer has a size of 300×1. Note here that, moisture distribution is estimated in terms of real part of the dielectric constant only. Including the imaginary part of the dielectric constant is straightforward but it will increase the computational load.
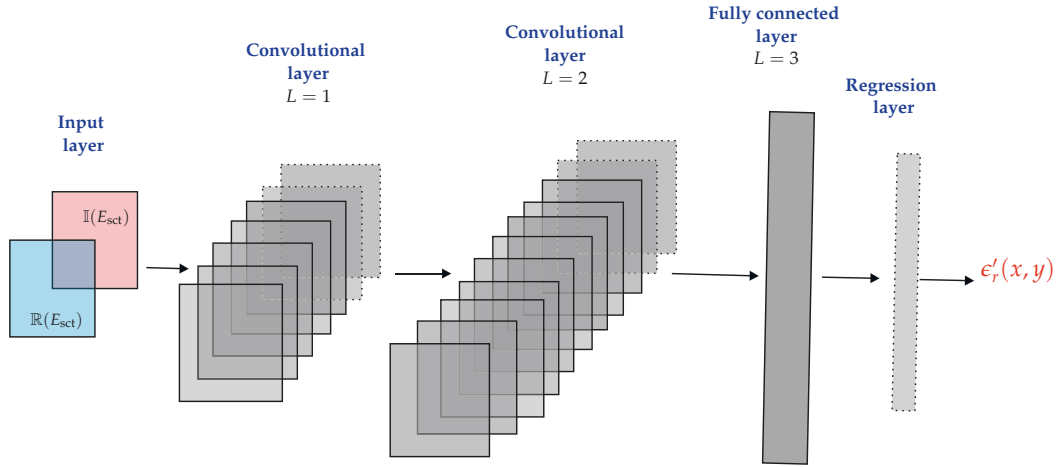
Figure 4. The architecture of the convolutional neural network used in this study.

The convolutional neural network (CNN) is trained using a dataset comprising of moisture content distribution $\{\Theta_m\}$ and corresponding scattered electric field parameters $\{E_{sct_m}\}$, $m = 1, \ldots, N_m$. N_m denotes the number of samples in the dataset. The generation of such a dataset is described below. In the training phase, the goal is to find biases b and weights w that minimize the discrepancy between $\{\Theta_\ell\}$ and the values estimated by the network $\{H_{w,b}(X_\ell)\}$. In this work, we minimize the quadratic loss function

$$f(w, b; \{E_{sct}\}_m) = \frac{1}{N_m} \sum_{m=1}^{N_m} \left\| H_{w,b}(E_{sct}) - \Theta_m \right\|^2, \tag{16}$$

to obtain the network parameters, biases, and weights of the network. For the network training process, the Adaptive moment estimation (Adam) optimizer [50] is chosen, with the batch size of 150 samples and epoch setting as 2000. The learning rates are set to 1×10^{-4} through out the training. All the computations were performed in a Python library TensorFlow [51] on a local computer with the configuration of 32 GB access memory, Intel Core(TM) i7-7820HQ central processing unit, and Nvidia Quadro M2200 graphic unit. The training of the network takes about 5 h.

3.1. Training, Validation, and Test Datasets

An initial dataset of $N_m = 10{,}000$ samples containing complex scattered electric field response and corresponding moisture distribution is built. Here, the scattered electric field data is generated using 2-D MoM with pulse basis and point matching techniques at 8.3 GHz frequency and by discretizing the foam into 100×30 pixels. Note that the lower frequency point is chosen from X-band as it offers to simulate the 2-D full-wave electromagnetic simulations with less computational load and low degree of non-linearity [52,53]. The physical parameters ϵ_r' and ϵ_r'' for each sample were drawn using the framework discussed earlier. Furthermore, five copies of the dataset are created by adding noise between 1% to 3% to the scattering data. The noise is added (following [54]) to each response of the complex electric field of the dataset as

$$E_{sct_{noise}} = E_{sct} + \max(E_{sct}) \frac{\beta}{\sqrt{2}} (\delta_1 + j\delta_2), \tag{17}$$

where $\max(E_{sct})$ is the maximum value of the scattered electric field, the coefficient $\delta_1 \sim \mathcal{U}(-1, 1)$ and $\delta_2 \sim \mathcal{U}(-1, 1)$ are two real vectors whose elements are sampled from uniform distribution. The term β denotes the noise levels and sampled as $\beta \sim \mathcal{U}(0.01, 0.03)$. Thus, leading to the total number of samples in the training dataset set to $N_m = 60,000$ where the complex electric field values are vectorised in real and imaginary parts. In addition, 2000 samples are generated following the same procedures as a validation dataset. The noise is added to validation dataset similarly as for the training samples.

Furthermore, a test dataset with 1000 samples was generated using denser discretization in MoM computation. A different discretization was chosen to ignore "inverse crime", i.e., the use of the same computational model or same grid settings to generate both training and test datasets. Otherwise, the same grid setting or the computational model may potentially lead to a situation where severe modelling errors are ignored and hence giving false impression on the accuracy of the estimates [55].

3.2. Reconstruction Results

This section gives results to evaluate the performance of the proposed neural network based estimation scheme. We applied the trained neural network to estimate the moisture field of the test datasets. The results are shown for four cases with low and moderate moisture levels, and high and nearly homogeneous moisture case.

3.2.1. Sample with Low, and Moderate Moisture Content

Two test samples with low (0–25%), and moderate (25–50%) wet-basis moisture contents are chosen as a first test case. As per the dielectric characterization, the real part of the dielectric constant value in the low moisture case varies approximately between 1.16 and 1.52 and for the moderate moisture case between 1.52 and 2.1. The corresponding scattered electric fields are measured and given as an input to the trained CNN. The noise level is set to $\beta = 0.03$, see Equation (17). The true test samples and estimated outputs from the CNN for the low moisture and for the moderate moisture are shown in Figure 5 (left column) and Figure 5 (right column), respectively. Further, to assess the closeness of the estimates, pixel values on data line $z = 2.25\,\text{cm}$ for low moisture case and pixel values on data line $z = 3.8\,\text{cm}$ for moderate moisture are visualized and shown in the bottom of Figure 5. In both cases, the CNN estimated output closely matches the ground truth. Estimation accuracy is evaluated by comparing the profile similarity index, denoted here as κ, which is evaluated as

$$\kappa = \frac{\iint_{\Omega_{\text{foam}}} \overline{\epsilon'_{r_{\text{CNN}}}}\,\overline{\epsilon'_{r_{\text{True}}}}\,dxdy}{\sqrt{\iint_{\Omega_{\text{foam}}} (\overline{\epsilon'_{r_{\text{CNN}}}})^2 dxdy}\sqrt{\iint_{\Omega_{\text{foam}}} (\overline{\epsilon'_{r_{\text{True}}}})^2 dxdy}}. \tag{18}$$

The term $\overline{\epsilon'_{r_{\text{CNN}}}} = \epsilon'_{r_{\text{CNN}}} - \langle \epsilon'_{r_{\text{CNN}}} \rangle$, and $\overline{\epsilon'_{r_{\text{True}}}} = \epsilon'_{r_{\text{True}}} - \langle \epsilon'_{r_{\text{True}}} \rangle$. The operator $\langle \cdot \rangle$ is the mean operator. For the κ, its values vary between 0 and 1. As it gets closer to 1, the estimated profile is closer to the ground truth. The performance metrics values for low and moderate moisture cases are shown in Table 2.

Table 2. κ for low and moderate moisture case.

	Low Moisture	Moderate Moisture
κ	0.9558	0.9361
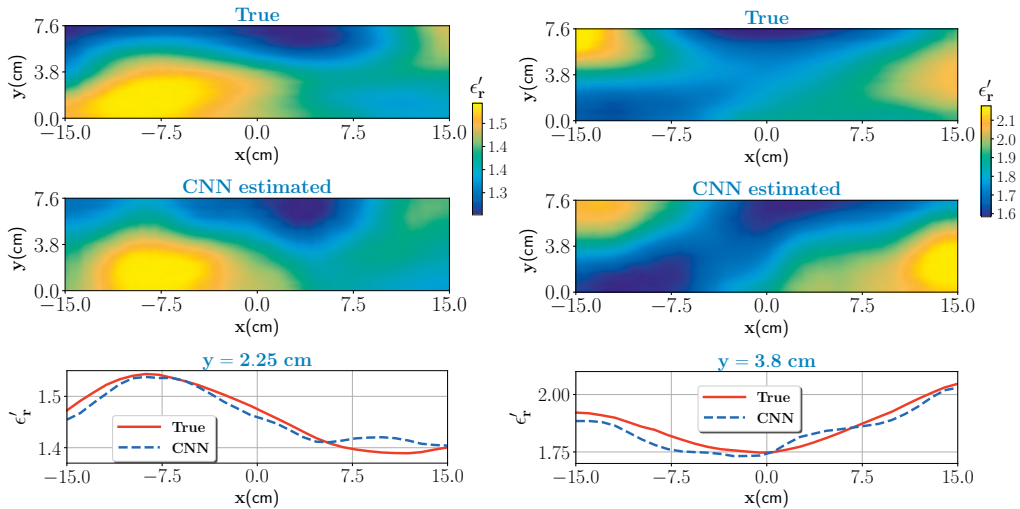
Figure 5. Low moisture case (left column): top figure shows the true profile and middle figure is the estimate from the CNN. Bottom figure compares the pixel values for the true and estimated profile at $y = 2.25$ cm data line. Moderate moisture case (right column): same caption of the low moisture case except for the bottom figure where pixel values are compared for data line $y = 3.8$ cm.

For both cases, κ values indicate that estimated profiles are similar to the ground truth. Note that we interpolated the number of pixels in the true profile to correspond with the pixels in the estimated profile to calculate κ.

3.2.2. Sample with High Moisture Distribution

In the actual drying process, it is very likely that the moisture variation at the inlet has high moisture levels. Considering this scenario, two special cases of moisture distribution are considered. In the first case, we consider the moisture levels with variation between 50% to 70% with corresponding real part of dielectric constant between 2.1–2.95. For the second case, the moisture levels are high but minor variations in the moisture, between 52% to 55%, is assumed (nearly homogeneous). The corresponding scattered electric fields are measured and given as an input to the trained CNN. The noise level is set to $\beta = 0.03$. The true test samples and estimated outputs from the CNN for the high moisture case with high variations and nearly homogeneous are shown in Figure 6 (left column) and Figure 6 (right column), respectively. Pixel values, as similar in the last section, are compared against the true case and shown in bottom for respective cases. For both cases, the estimated output is close to the ground truth. The profile similarity index, κ, values as shown in Table 3 indicate that estimated output is fairly close to the ground truth.

**Table 3.** $\mathcal{K}$ for high moisture case.

|	High Variation	Homogeneous
$\mathcal{K}$	0.923	0.883
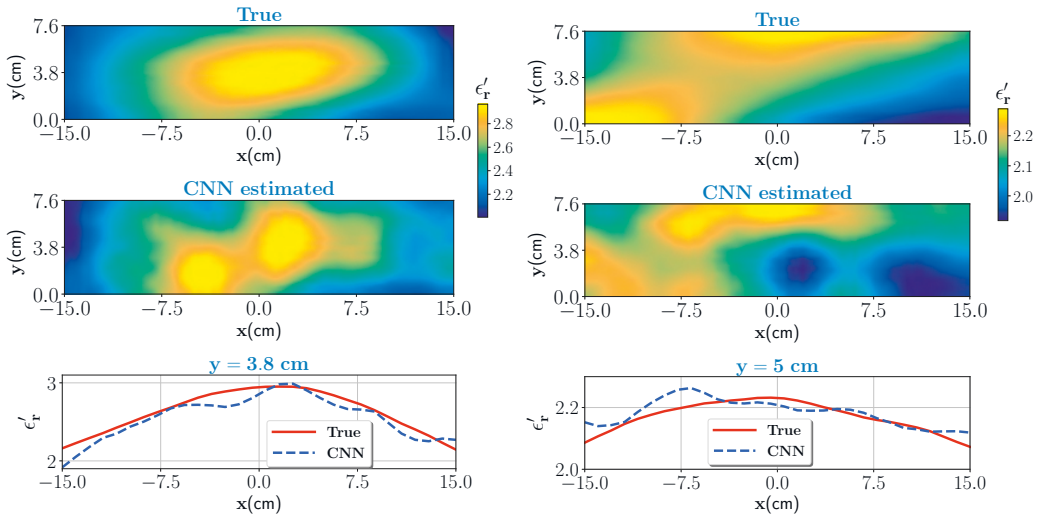
Figure 6. High moisture case with high variation (left column): top figure shows the true profile and middle figure is the estimate from the CNN. Bottom figure compares the pixel values for the true and estimated profile at $y = 3.8$ cm data line. Nearly homogeneous case (right column): same caption except for the bottom figure where pixel values are compared for data line $y = 5$ cm.

3.2.3. Error Statistics

In the test dataset, for each sample the noise is added and its level is chosen from $\beta \sim \mathcal{U}(0.01, 0.03)$. Estimates of the ϵ'_r for the whole test data are shown pixel-wise in Figure 7 (top left). Aside, the profile similarity index for each sample is compared against the respective true case and shown in Figure 7 (top right). The figure also includes a relative estimation error histogram. Uncertainties in the estimations can be seen mainly due to uncertainties in dielectric's characterization (see Table 1) and higher noise levels. Specifically, with uncertainties in dielectric characterization, samples with same moisture levels are not unique in dielectric values. Nonetheless, the overall estimation success of the trained CNN on the test dataset for most samples are fairly good.
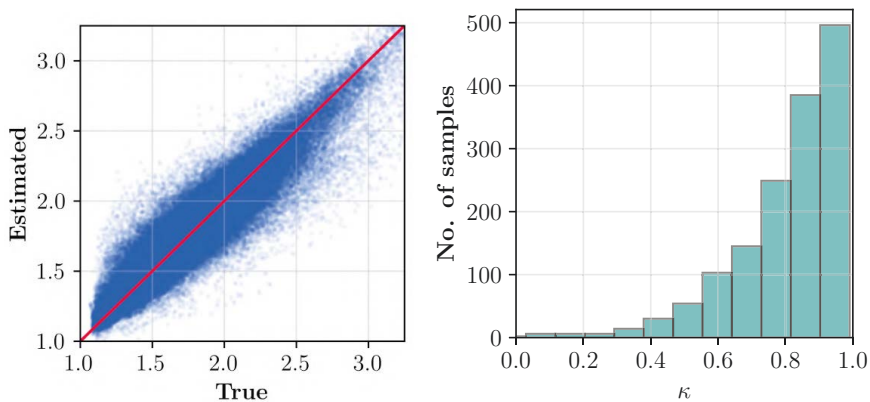

Figure 7. *Cont.*
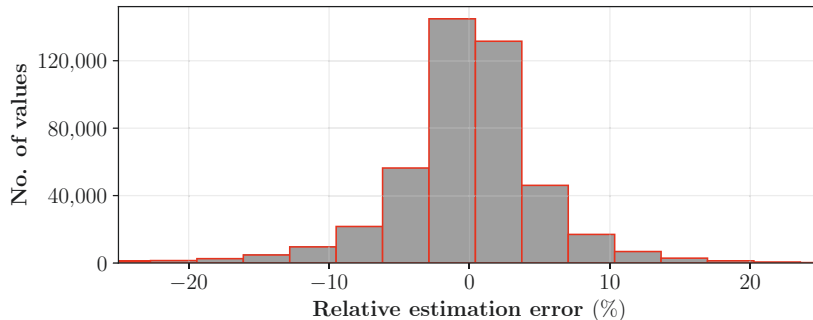
Figure 7. Top **left**: estimated pixel values of the $\epsilon_r'(x, y)$ for the test dataset with 1000 samples. Top **right**: histogram of factor κ. **Bottom**: difference between the estimated and true values (relative estimation error) of the real part of the dielectric constant for the total number of test samples.

4. Experimental Setup and Result

In this section, the trained CNN performance is tested on the data from our developed MWT experimental prototype. The MWT experimental prototype consist of 7 WR90 open-ended waveguide antennas and placed over the foam of width = 50 cm, height = 7.6 cm, and length = 75 cm, respectively. The distance of the antenna to the top surface of the polymer foam is 5 cm, and the center to center distance between two adjacent antennas is 5 cm. Antennas are fixed and placed in free-space from -15 cm to 15 cm along the x-axis. For data acquisition, antennas are connected to the Agilent N5224A vector network analyzer (VNA) via a P9164C 2×16 USB Solid state switch matrix. Phase stable cables (with phase stability of $3°$ at maximum frequency) are used for the connection. Communication between the VNA, switch, and the controlling computer is accomplished through the Ethernet cable. The block diagram of the data acquisition scheme and the S_{11} (return-loss) response of a WR-90 waveguide antenna are shown in Figure 8 top left and top right, respectively. The data acquisition process and image reconstruction process (<1 s) is entirely automated using MATLAB. The measured scattered electric field data, in terms of scattering parameter, is acquired at 8.3 GHz frequency at cross-section of $z = 0$ cm and takes around 20 s. Since the CNN network is trained on electric field data instead of scattering parameter, calibration scheme in [56] is employed for its conversion.

As a first example, we have considered a PTFE Teflon ($\epsilon_r' \approx 2.1$) material with cylindrical shape (diameter of 2.25 cm) and placed inside the foam through an incision on the top surface. The reason for choosing this target is twofold. First, it will act as a benchmark target to test if the estimated dielectric values by the CNN are correct as the true value is well in the range of our interest. An approximate location of the target inside the foam is centered at $(-4.5 \text{ cm}, 3.8 \text{ cm}, 0 \text{ cm})$. Second, to test the overall generalization capabilities of the trained architecture for identifying targets not seen as a ground truth while its training. The estimated output from the CNN is shown in Figure 9. Estimated result shows that the target is satisfactorily estimated by the network but it is slightly overestimated in the shape. The overestimation of the shape is predominately due to the smoothness model used in the training. However, note that the aim of our work is not accurate shape reconstruction and finding the locations of dominant of wet-spots is sufficient to design control strategies.
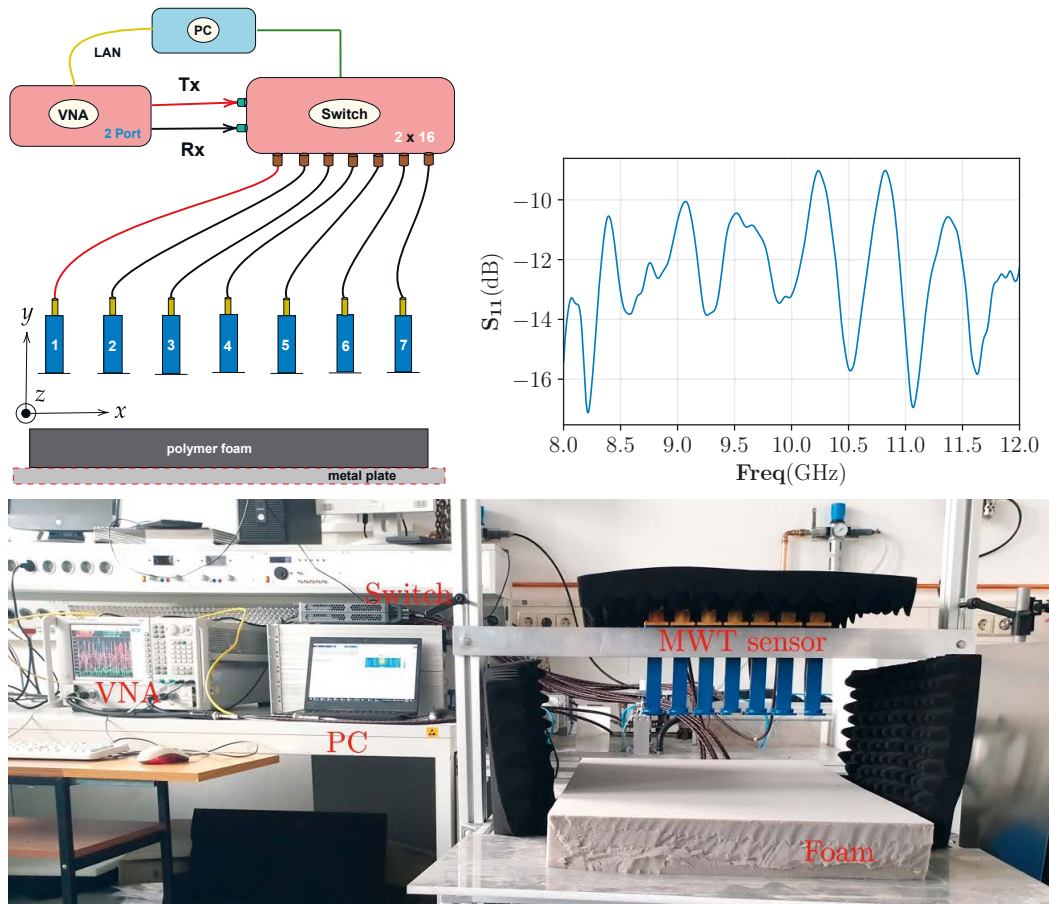
Figure 8. Top **left**: data acquisition scheme for the MWT measurement from the sensor array with X-band open waveguide antennas. Top **right**: the S_{11} response of the WR-90 waveguide antenna. **Bottom**: prototype of MWT sensor array used in this study to generate measurement data. This system is developed at KIT, Germany and has been integrated with the HEPHASITOS technology.
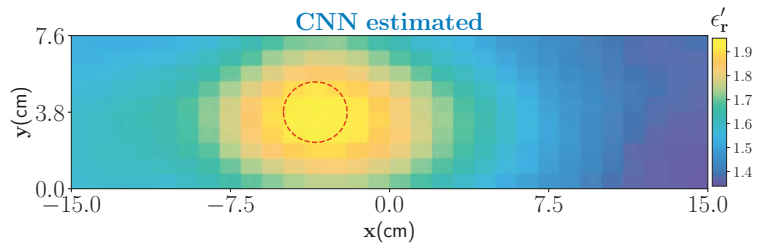
Figure 9. CNN estimation of cylindrical Teflon resin placed inside the foam. The true location of the target is marked by red-dash circle.

In the second example, we have considered a moisture wet-spot inside the foam. To create the wet-spot moisture target, a spherical foam of diameter 2.5 and with 43% wet-basis moisture level ($\epsilon_r \approx 1.81 - j0.079$) is chosen. An approximate location of the

target inside the foam is centered at $(-3.25\,\mathrm{cm}, 1.85\,\mathrm{cm}, 0\,\mathrm{cm})$. The estimated output from the CNN is shown in Figure 10. Estimated result shows that the network can satisfactorily locate the wet-spot which is placed around the bottom of the foam. The estimated real part of the dielectric constant corresponds between 37% and 39% of moisture level in the wet-spot.
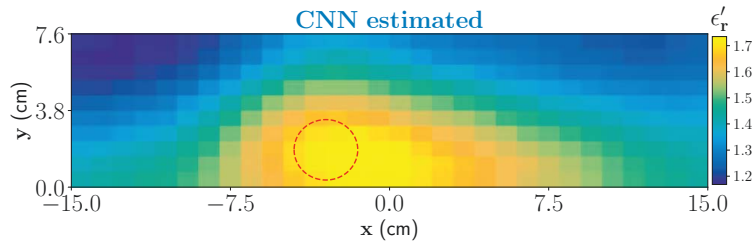
Figure 10. CNN estimation of one dominant wet-spot with 43% moisture inside the foam.

5. Conclusions

In this paper, a neural network based method for the microwave tomography is developed for real-time moisture estimation in a polymer foam. The neural network is trained with synthetic data generated using two-dimensional scattering model based on method of moment formulation. Furthermore, in the scattering model, a parametric model based on the dielectric characterization of the foam is utilized to generate moisture samples. The network performance is tested with numerical data and experimental data from the constructed MWT prototype. Results shows the capability of the present method to be used in real-time moisture estimation. Here, the studied microwave imaging modality is applied to recover moisture content distribution inside a porous foam but the framework is applicable to investigate other material types together with different physical parameters. In the final stage, the estimated moisture information will be utilized in feed-forward loop of the intelligent control block of the industrial drying system.

It was observed in the experimental results that the real part of the dielectric constant in the estimation are slightly underestimated which are caused due to modeling errors, i.e., 3D measurements and 2D forward model and small uncertainties in the dielectric characterization of the foam, respectively. Henceforth, for our work the scope for improvement lies in the uncertainty quantification (UQ). In general, UQ in deep neural networks is a very active research topic and several approaches have been proposed and studied, see, e.g., recent reviews [57,58]. Furthermore, we also observe that in the estimates the background information, i.e., the dry part is not well distinguishable. This mainly due to the Gaussian based covariance structure used for generating moisture distribution. One solution is to use covariance structure models with a scaling factor such as Matérn class [49].

Data Availability Statement: The data presented in this study are available on request from the corresponding authors.

**Conflicts of Interest:** The authors declare no conflict of interest.

References

1. Osepchuk, J. A History of Microwave Heating Applications. *IEEE Trans. Microw. Theory Tech.* **1984**, *32*, 1200–1224. [CrossRef]
2. Metaxas, A.C.; Meredith R.J. *Industrial Microwave Heating*; P. Peregrinus on behalf of the Institution of Electrical Engineers: London, UK, 1988.
3. Roussy, G.; Bennani, A.; Thiebaut, J. Temperature runaway of microwave irradiated materials. *J. Appl. Phys.* **1987**, *62*, 1167–1170. [CrossRef]
4. Bykov, Y.V.; Rybakov, K.I.; Semenov, V.E. High-temperature microwave processing of materials. *J. Phys. D Appl. Phys.* **2001**, *34*, R55–R75. [CrossRef]
5. Sun, Y. Adaptive and Intelligent Temperature Control of Microwave Heating Systems with Multiple Sources. Ph.D. Thesis, KIT Scientific Publishing, Karlsruhe, Germany, 2016.
6. Link, G.; Ramopoulos, V. Simple analytical approach for industrial microwave applicator design. *Chem. Eng. Process.-Process Intensif.* **2018**, *125*, 334–342. [CrossRef]
7. Omrani, A.; Link, G.; Jelonnek, J. A Multistatic Uniform Diffraction Tomographic Algorithm for Real-Time Moisture Detection. In Proceedings of the 2020 IEEE Asia-Pacific Microwave Conference (APMC), Hong Kong, China, 10–13 November 2020; pp. 437–439. [CrossRef]
8. Hosseini, M.; Kaasinen, A.; Link, G.; Lähivaara, T.; Vauhkonen, M. LQR Control of Moisture Distribution in Microwave Drying Process Based on a Finite Element Model of Parabolic PDEs. *IFAC-PapersOnLine* **2020**, *53*, 11470–11476. [CrossRef]
9. Wu, Z. Developing a microwave tomographic system for multiphase flow imaging: Advances and challenges. *Trans. Inst. Meas. Control* **2015**, *37*, 760–768. [CrossRef]
10. Wu, Z.; Wang, H. Microwave Tomography for Industrial Process Imaging: Example Applications and Experimental Results. *IEEE Antennas Propag. Mag.* **2017**, *59*, 61–71. [CrossRef]
11. Trabelsi, S.; Kraszewski, A.W.; Nelson, S.O. A microwave method for on-line determination of bulk density and moisture content of particulate materials. *IEEE Trans. Instrum. Meas.* **1998**, *47*, 127–132. [CrossRef]
12. Okamura, S. Microwave Technology for Moisture Measurement. *Subsurf. Sens. Technol. Appl.* **2000**, *1*, 205–227. [CrossRef]
13. Trabelsi, S.; Nelson, S.O. Nondestructive sensing of physical properties of granular materials by microwave permittivity measurement. *IEEE Trans. Instrum. Meas.* **2006**, *55*, 953–963. [CrossRef]
14. Trabelsi, S.; Nelson, S.O.; Lewis, M.A. Microwave nondestructive sensing of moisture content in shelled peanuts independent of bulk density and with temperature compensation. *Sens. Instrum. Food Qual. Saf.* **2009**, *3*, 114–121. [CrossRef]
15. Trabelsi, S. New Calibration Algorithms for Dielectric-Based Microwave Moisture Sensors. *IEEE Sens. Lett.* **2017**, *1*, 1–4. [CrossRef]
16. You, K.Y.; Lee, C.Y.; Then, Y.L.; Chong, S.H.C.; You, L.L.; Abbas, Z.; Cheng, E.M. Precise Moisture Monitoring for Various Soil Types Using Handheld Microwave-Sensor Meter. *IEEE Sens. J.* **2013**, *13*, 2563–2570. [CrossRef]
17. Javed, N.; Habib, A.; Amin, Y.; Loo, J.; Akram, A.; Tenhunen, H. Directly Printable Moisture Sensor Tag for Intelligent Packaging. *IEEE Sens. J.* **2016**, *16*, 6147–6148. [CrossRef]
18. Franchois, A.; Pichot, C. Microwave imaging-complex permittivity reconstruction with a Levenberg-Marquardt method. *IEEE Trans. Antennas Propag.* **1997**, *45*, 203–215. [CrossRef]
19. Zhong, Y.; Lambert, M.; Lesselier, D.; Chen, X. A New Integral Equation Method to Solve Highly Nonlinear Inverse Scattering Problems. *IEEE Trans. Antennas Propag.* **2016**, *64*, 1788–1799. [CrossRef]
20. Arridge, S.; Maass, P.; Öktem, O.; Schönlieb, C.B. Solving inverse problems using data-driven models. *Acta Numer.* **2019**, *28*, 1–174. [CrossRef]
21. Higham, C.F.; Higham, D.J. Deep Learning: An Introduction for Applied Mathematicians. *SIAM Rev.* **2019**, *61*, 860–891. [CrossRef]
22. Elshafiey, I.; Udpa, L.; Udpa, S.S. Application of neural networks to inverse problems in electromagnetics. *IEEE Trans. Magn.* **1994**, *30*, 3629–3632. [CrossRef]
23. Bartley, P.G.; Nelson, S.O.; McClendon, R.W.; Trabelsi, S. Determining moisture content of wheat with an artificial neural network from microwave transmission measurements. *IEEE Trans. Instrum. Meas.* **1998**, *47*, 123–126. [CrossRef]
24. Shrestha, B.L.; Wood, H.C.; Tabil, L.; Baik, O.; Sokhansanj, S. Microwave permittivity-assisted artificial neural networks for determining moisture content of chopped alfalfa forage. *IEEE Instrum. Meas. Mag.* **2017**, *20*, 37–42. [CrossRef]
25. Zhou, Y.; Zhong, Y.; Wei, Z.; Yin, T.; Chen, X. An Improved Deep Learning Scheme for Solving 2-D and 3-D Inverse Scattering Problems. *IEEE Trans. Antennas Propag.* **2021**, *69*, 2853–2863. [CrossRef]

26. Ma, Z.; Xu, K.; Song, R.; Wang, C.F.; Chen, X. Learning-Based Fast Electromagnetic Scattering Solver Through Generative Adversarial Network. *IEEE Trans. Antennas Propag.* **2021**, *69*, 2194–2208. [CrossRef]
27. Guo, R.; Shan, T.; Song, X.; Li, M.; Yang, F.; Xu, S.; Abubakar, A. Physics Embedded Deep Neural Network for Solving Volume Integral Equation: 2D Case. *IEEE Trans. Antennas Propag.* **2021**. [CrossRef]
28. Guo, L.; Song, G.; Wu, H. Complex-Valued Pix2pix—Deep Neural Network for Nonlinear Electromagnetic Inverse Scattering. *Electronics* **2021**, *10*, 752. [CrossRef]
29. Sanghvi, Y.; Kalepu, Y.N.G.B.; Khankhoje, U. Embedding Deep Learning in Inverse Scattering Problems. *IEEE Trans. Comput. Imaging* **2019**, *6*, 46–56. [CrossRef]
30. Lin, Z.; Guo, R.; Li, M.; Abubakar, A.; Zhao, T.; Yang, F.; Xu, S. Low-Frequency Data Prediction With Iterative Learning for Highly Nonlinear Inverse Scattering Problems. *IEEE Trans. Microw. Theory Tech.* **2021**. [CrossRef]
31. Li, L.; Wang, L.G.; Teixeira, F.L.; Liu, C.; Nehorai, A.; Cui, T.J. DeepNIS: Deep Neural Network for Nonlinear Electromagnetic Inverse Scattering. *IEEE Trans. Antennas Propag.* **2019**, *67*, 1819–1825. [CrossRef]
32. Lähivaara, T.; Yadav, R.; Link, G.; Vauhkonen, M. Estimation of Moisture Content Distribution in Porous Foam Using Microwave Tomography With Neural Networks. *IEEE Trans. Comput. Imaging* **2020**, *6*, 1351–1361. [CrossRef]
33. Yadav, R.; Vauhkonen, M.; Link, G.; Betz, S.; Lähivaara, T. Microwave tomography for estimating moisture content distribution in porous foam using neural networks. In Proceedings of the 2020 14th European Conference on Antennas and Propagation (EuCAP), Denmark, Sweden, 15–20 March 2020; pp. 1–5. [CrossRef]
34. Yadav, R.; Omrani, A.; Vauhkonen, M.; Link, G.; Lähivaara, T. Microwave Tomography for Moisture Level Estimation Using Bayesian Framework. In Proceedings of the 2021 15th European Conference on Antennas and Propagation (EuCAP), Düsseldorf, Germany, 22–26 March 2021; pp. 1–5. [CrossRef]
35. Omrani, A.; Yadav, R.; Link, G.; Vauhkonen, M.; Lähivaara, T.; Jelonnek, J. A Combined Microwave Imaging Algorithm for Localization and Moisture Level Estimation in Multilayered Media. In Proceedings of the 2021 15th European Conference on Antennas and Propagation (EuCAP), Düsseldorf, Germany, 22–26 March 2021; pp. 1–5. [CrossRef]
36. Balanis, C. *Advanced Engineering Electromagnetics*, 2nd ed.; Wiley: Hoboken, NJ, USA, 2012.
37. Chew, W.C. *Waves and Fields in Inhomogenous Media*; IEEE Press: New York, NY, USA, 1995.
38. Caorsi, S.; Gragnani, G.L.; Pastorino, M. Two-dimensional microwave imaging by a numerical inverse scattering solution. *IEEE Trans. Microw. Theory Tech.* **1990**, *38*, 980–981. [CrossRef]
39. Chew, W.; Wang, Y. Reconstruction of two-dimensional permittivity distribution using the distorted Born iterative method. *IEEE Trans. Med. Imaging* **1990**, *9*, 218–225. [CrossRef]
40. Sadeghi, S.; Mohammadpour-Aghdam, K.; Faraji-Dana, R.; Burkholder, R.J. A DORT-Uniform Diffraction Tomography Algorithm for Through-the-Wall Imaging. *IEEE Trans. Antennas Propag.* **2020**, *68*, 3176–3183. [CrossRef]
41. Janalizadeh, R.C.; Zakeri, B. A Source-Type Best Approximation Method for Imaging Applications. *IEEE Antennas Wirel. Propag. Lett.* **2016**, *15*, 1707–1710. [CrossRef]
42. Tai, C.T. *Dyadic Green Functions in Electromagnetic Theory*; IEEE: New York, NY, USA, 1994.
43. Lindell, I.V. *Methods for Electromagnetic Field Analysis*; Wiley-IEEE Press: Hoboken, NJ, USA, 1992.
44. Monk, P. *Finite Element Methods for Maxwell's Equations*; Oxford University Press: Oxford, UK, 2003.
45. Harrington, R. *Time-harmonic Electromagnetic Fields*; Electronics Series; McGraw-Hill: New York, NY, USA, 1961.
46. Richmond, J. Scattering by a dielectric cylinder of arbitrary cross section shape. *IEEE Trans. Antennas Propag.* **1965**, *13*, 334–341. [CrossRef]
47. Saad, Y.; Schultz, M.H. GMRES: A Generalized Minimal Residual Algorithm for Solving Nonsymmetric Linear Systems. *SIAM J. Sci. Stat. Comput.* **1986**, *7*, 856–869. [CrossRef]
48. Soldatov, S.; Kayser, T.; Link, G.; Seitz, T.; Layer, S.; Jelonnek, J. Microwave cavity perturbation technique for high-temperature dielectric measurements. In Proceedings of the 2013 IEEE MTT-S International Microwave Symposium Digest (MTT), Seattle, WA, USA, 2–7 June 2013; pp. 1–4. [CrossRef]
49. Rasmussen, C.; Williams, C. *Gaussian Processes for Machine Learning*; The MIT Press: Cambridge, MA, USA, 2006.
50. Kingma, D.P.; Ba, J. Adam: A Method for Stochastic Optimization. *arXiv* **2014**, arXiv:1412.6980.
51. Abadi, M.; Agarwal, A.; Barham, P.; Brevdo, E.; Chen, Z.; Citro, C.; Corrado, G.S.; Davis, A.; Dean, J.; Devin, M.; et al. TensorFlow: Large-Scale Machine Learning on Heterogeneous Systems. *arXiv* **2015**, arXiv:1603.04467.
52. Bucci, O.M.; Cardace, N.; Crocco, L.; Isernia, T. Degree of nonlinearity and a new solution procedure in scalar two-dimensional inverse scattering problems. *J. Opt. Soc. Am. A* **2001**, *18*, 1832–1843. [CrossRef]
53. Bevacqua, M.T.; Isernia, T. An Effective Rewriting of the Inverse Scattering Equations via Green's Function Decomposition. *IEEE Trans. Antennas Propag.* **2021**, *69*, 4883–4893. [CrossRef]
54. Abubakar, A.; van den Berg, P.; Semenov, S. A robust iterative method for Born inversion. *IEEE Trans. Geosci. Remote Sens.* **2004**, *42*, 342–354. [CrossRef]
55. Kaipio, J.; Somersalo, E. Statistical inverse problems: Discretization, model reduction and inverse crimes. *J. Comput. Appl. Math.* **2007**, *198*, 493–504. [CrossRef]
56. Ostadrahimi, M.; Mojabi, P.; Gilmore, C.; Zakaria, A.; Noghanian, S.; Pistorius, S.; LoVetri, J. Analysis of Incident Field Modeling and Incident/Scattered Field Calibration Techniques in Microwave Tomography. *IEEE Antennas Wirel. Propag. Lett.* **2011**, *10*, 900–903. [CrossRef]

57. Gawlikowski, J.; Tassi, C.R.N.; Ali, M.; Lee, J.; Humt, M.; Feng, J.; Kruspe, A.; Triebel, R.; Jung, P.; Roscher, R.; et al. A Survey of Uncertainty in Deep Neural Networks. 2021. Available online: http://xxx.lanl.gov/abs/2107.03342 (accessed on 14 October 2021).

58. Abdar, M.; Pourpanah, F.; Hussain, S.; Rezazadegan, D.; Liu, L.; Ghavamzadeh, M.; Fieguth, P.; Cao, X.; Khosravi, A.; Acharya, U.R.; et al. A review of uncertainty quantification in deep learning: Techniques, applications and challenges. *Inf. Fusion* **2021**, *76*, 243–297. [CrossRef]

Paper **II**
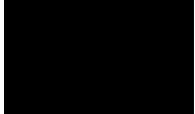
Correlated Sample-Based Prior in Bayesian Inversion Framework for Microwave Tomography

Rahul Yadav, Adel Omrani, Guido Link, Marko Vauhkonen, and Timo Lähivaara

Abstract—**When using the statistical inversion framework in microwave tomography (MWT), generally, the real and imaginary parts of the unknown dielectric constant are treated as uncorrelated and independent random variables. Thereby, in the maximum *a posteriori* estimates, the two recovered variables may show different structural changes inside the imaging domain. In this work, a correlated sample-based prior model is presented to incorporate the correlation of the real part with the imaginary part of the dielectric constant in the statistical inversion framework. The method is used to estimate the inhomogeneous moisture distribution (as dielectric constant) in a large cross section of polymer foam. The targeted application of MWT is in industrial drying to derive intelligent control methods based on tomographic inputs for selective heating purposes. One of the features of the proposed method shows how to integrate lab-based dielectric characterization, often available in MWT application cases, in the prior modeling. The method is validated with numerical and experimental MWT data for the considered moisture distributions.**

Index Terms—**Correlated sample-based prior, industrial microwave drying, maximum *a posteriori*, microwave tomography, statistical inversion method.**

I. INTRODUCTION

MICROWAVE tomography (MWT) use-cases in the industry are mostly for monitoring and inspection purposes, as reported in [1]–[3]. A new idea is to apply MWT based control in the industrial microwave heating system [4], known as HEPHAISTOS [5], to increase its heating efficiency and enhance the material processing quality. The HEPHAISTOS system has a hexagonal design [6] for the applicator (cavity) that offers a very high uniform electromagnetic field inside the cavity. Its main areas of applications

are in material processing, for example, drying, sintering, and thermal curing. Often, this system suffers from the problem of hot-spot formation and overheating (thermal runaway) specifically while drying materials with low-loss like porous polymer foam. These situations may degrade the quality of material processing or may even lead to damage to the industrial unit.

One of the solutions to eliminate the problem of thermal runaway and hot-spot formation is intelligent control of power sources (magnetrons) to obtain a selective heating rate at each stage of the drying process [7], [8]. However, to apply such a precise microwave power control *in situ* and noninvasive measurement of the unknown distribution of moisture inside the porous material is required. The infrared camera sensors integrated with the microwave drying systems for process observation are limited to providing information on the material's surface only and, hence, not adequate to provide efficient control of microwave power sources. Thus, integration of MWT imaging modality [9], [10] with the drying system was proposed to estimate the moisture content distribution in a polymer foam. Using the MWT tomographic output, strategies for intelligent control can be derived. The MWT senor setup consists of open-ended waveguide antennas operating in the X-band range. The selection of the frequency and the antenna type for the MWT sensor array are detailed in [11]. For estimating the moisture levels (in terms of dielectric constant) in a porous material with a large cross-sectional dimension, we apply a statistical inversion approach [12] based on the Bayesian framework. Some earlier efforts of using statistical inversion approaches in MWT have been proposed in [13]–[16].

In our earlier studies [17], [18] on statistical inversion in MWT, the real and imaginary parts of the unknown dielectric constant were treated as independent and uncorrelated random variables. This assumption led to independent reconstructions of the real and imaginary parts, causing conflicting and incorrect moisture level estimates by the real and imaginary parts. As the imaginary part governs the heating behavior, its correct estimation becomes imperative when deriving optimal control algorithms for the drying system. Therefore, to achieve accurate maximum *a posteriori* estimates (MAP), the key is to construct a joint-prior model that favors correlation between the real and imaginary parts. In [19] and [20], a similar problem is addressed using the expectation–maximization (EM) algorithm [21], albeit it may not be a suitable approach for our high-dimensional problem with a nonlinear observation model.

On the other hand, joint reconstructions in the deterministic inversion methods have been addressed in: 1) [22] where the complex permittivity in the imaging domain is expressed as a weighted sum of a few pre-selected permittivities, close to the range of the expected values, and permittivity weights are obtained using Gauss–Newton inversion (GNI) algorithm; however, the method is mostly valid for practical biomedical applications with linearized inverse scattering model and 2) in [23] and [24], an approximate ratio is obtained between the real and imaginary parts of the complex permittivity based on the dielectric characterization of the material(s) under test, and this approximate ratio served as the prior information in the GNI algorithm with the total variation multiplicative regularizer term. Moreover, the results show improvement by adjusting the approximate average ratio. However, in our work, the moisture-to-dielectric relationship is nonlinear; thus, a single average factor for all moisture points will lead to inaccurate reconstructions.

In this work, we present a correlated sample-based prior model, as an extension to our preliminary work [25], to construct the prior covariance structure for the joint-prior Gaussian density. The method is primarily suitable for the use-case of MWT when either structural information of the imaging domain or dielectric behavior of the material under test is available *a priori*. For example, in medical applications, the structure of the body organs and their dielectric properties are known approximately. In our MWT application, dielectric characterization of the foam with respect to different moisture levels (wet-basis) is available. To form the prior covariance structure, first, a database containing possible moisture distribution is formed with different spatial variations. The inhomogeneous profile of each sample is modeled using the squared exponential covariance function, and its dielectric values are based on the available dielectric characterization data. Next, the second-order statistics of this database are calculated to build the joint prior covariance structure. Herein, the performance of the proposed correlated sample-based prior model is first evaluated with numerical scattered field data from the 2-D MWT setup for three moisture scenarios. Furthermore, we have also evaluated the sample-based prior model on the scattered electric field data from our developed prototype of the MWT system. Results presented show the efficacy of this approach in comparison to the past approach where parameters are considered uncorrelated.

This article is organized as follows. Section II provides an overview of the MWT setup and the forward observation model. Section III details the statistical inversion framework. Prior construction and sample-based prior model approach are given in Section IV. In Section V, the results for different realistic moisture scenarios are presented using 2-D synthetic data. Experimental results are investigated in Section VI. Finally, Section VII shows the concluding remarks.

II. MICROWAVE TOMOGRAPHY: SETUP AND OBSERVATION MODEL

In this study, we consider a 2-D imaging domain $\Omega_{\text{foam}} = [-25, \ 25] \times [-1.5, \ 1.5]$ cm with inhomogenous relative dielectric constant $\epsilon_r = \epsilon_r' - j\epsilon_r''$, placed in the background

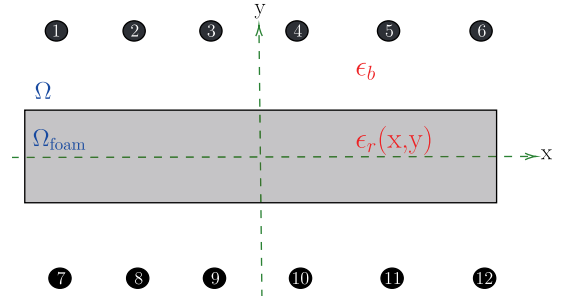

Fig. 1. Schematic of the 2-D MWT setup used in the study.

domain Ω consisting of free-space with $\epsilon_b = 1 - j0$. For this 2-D numerical study, the open-ended waveguide antennas are modeled as a line source with an excitation frequency of 8.3 GHz and are located at a distance of 15 cm from the top and bottom surfaces of the foam. The 2-D MWT setup is shown in Fig. 1 where the sources are represented by number Tags $N = 1, 2, \ldots, 12$. The scattered electric field E^{scat} under the illumination of time-harmonic (time convention $e^{-j\omega t}$ with angular frequency of ω is assumed and suppressed) TM-polarized incident field is given as [26], [27]

$$E^{\text{scat}}(r) = k^2 \int_{\Omega_{\text{foam}}} G(r, r')(\epsilon_r(r') - \epsilon_b) E_{\text{tot}}(r')dr'$$
$$\forall r \in \Omega, \quad r' \in \Omega_{\text{foam}} \quad (1)$$

where k is the wavenumber of the background medium and $G(r, r')$ is the background Green's function of 2-D line source (i.e. the Hankel function of the second kind and zeroth order). The observation and source points are denoted by the position vectors $r \mapsto (x, y)$ and $r' \mapsto (x', y')$, respectively. The term E_{tot} is the total electric field inside the domain Ω_{foam} and is calculated as

$$E_{\text{tot}}(r) = E_{\text{inc}}(r) + k^2 \int_{\Omega_{\text{foam}}} G(r, r')(\epsilon_r(r') - \epsilon_b) E_{\text{tot}}(r')dr'$$
$$\forall r, \ r' \in \Omega_{\text{foam}} \quad (2)$$

where E_{inc} is the incident electric field.

After discretization [28], [29] for all N transmitter and receiver, (1) is given as

$$E^{\text{scat}} = \mathcal{L}_{\text{o}}(\epsilon_r) E_{\text{tot}} \quad (3)$$

and (2) as

$$E_{\text{tot}} = [\text{I} - \mathcal{L}_{\text{in}}(\epsilon_r)]^{-1} E_{\text{inc}}. \quad (4)$$

Furthermore, by substituting (4) in (3), the scattered electric field can then be expressed as

$$E^{\text{scat}} = \mathcal{L}_{\text{o}}(\epsilon_r)[\text{I} - \mathcal{L}_{\text{in}}(\epsilon_r)]^{-1} E_{\text{inc}} = \mathcal{F}(\epsilon_r) \quad (5)$$

where $\mathcal{L}_0$ and $\mathcal{L}_{\text{in}}$ are short notations for the integral operators in (1) and (2), respectively. This is known as a forward observation model that maps the dielectric constant to scattered electric field where the mapping is denoted by $\mathcal{F}$. As the total electric field depends on the dielectric constant of the foam, its mapping with the scattered electric field is nonlinear.

In (5), the scattered field data can come from real experiment or may be simulated data, while the right-hand side denotes the approximate physical nature of the problem. To obtain estimates using measurement data related to S-parameters, proper calibration scheme can be used to convert the data into electric field [30], [31].

In MWT, the aim is to estimate the 2-D dielectric profile of the porous material given the measurement data E^{scat}. Generally, this is a severely ill-posed inverse problem mainly due to the fact that different profiles may map to the same measurement data. Also, part of the ill-posedness is due to the properties of the integral operator defined in (5) [32]. Under the quantitative inversion framework, the regularization term (related to the prior information) can reduce this problem to some level and improve the estimates. In our case, some prior information related to the dielectric behavior of the foam with respect to wet-basis moisture content level is available. Furthermore, we expect the moisture content distribution to have smooth distribution in the foam. In this work, to naturally encode this information in the regularization term, we apply a statistical inversion approach based on the Bayesian framework. With the Bayesian estimate, it can be quantified which parameters are more favorable to generate the measurement data rather than providing fixed estimates that are given in classical, deterministic, inversion framework.

III. Bayesian Inversion Framework

Consider an inverse problem of identifying an unknown parameter $\epsilon_r \in \mathbb{C}^{m \times n}$ given noisy measurement data $E^{\text{scat}} \in \mathbb{C}^{N \times N}$ according to the observation model [17], [18]

$$E^{\text{scat}} = \mathscr{F}(\epsilon_r) + \xi \tag{6}$$

where ξ denotes the additive measurement noise component. Herein, the unknown parameter and noise terms are considered mutually independent. Note that the unknown parameter and the measurement data are complex quantities and denoted by $\mathbb{C}$. In this article, the real and imaginary parts are treated separately as real-valued random variables for the real-valued optimization problem. They are separated into real and imaginary parts and concatenated in the 2-D vector form as

$$E^{\text{scat}} = \begin{pmatrix} \mathbb{R}\{E^{\text{scat}}\} \\ \mathbb{I}\{E^{\text{scat}}\} \end{pmatrix}_{2S \times 1} \tag{7}$$

and

$$\epsilon_r = \begin{pmatrix} \{\epsilon_{r_i'}\} \\ \{\epsilon_{r_i''}\} \end{pmatrix}_{2N_n \times 1}, \quad i = 1, 2, \ldots, N_n \tag{8}$$

where $S = N \times N$ and $N_n = m \times n$ are the total number of measurements and the total number of unknowns, respectively.

In statistical inversion, we treat the unknown parameters as random variables, and information about them is expressed in terms of probability densities. The inverse problem can then be expressed as given the measurement data, and the task is to find the conditional probability density $\pi(\epsilon_r \mid E^{\text{scat}})$ for the unknown parameter ϵ_r. The conditional probability density is

constructed using Bayes' theorem as

$$\pi(\epsilon_r \mid E^{\text{scat}}) = \frac{\pi(E^{\text{scat}} \mid \epsilon_r)\pi(\epsilon_r)}{\pi(E^{\text{scat}})}$$
$$\propto \pi(E^{\text{scat}} \mid \epsilon_r)\pi(\epsilon_r) \tag{9}$$

where $\pi(\epsilon_r \mid E^{\text{scat}})$ is the posterior density, $\pi(E^{\text{scat}} \mid \epsilon_r)$ is the likelihood density that represents the distribution of the measured data if ϵ_r is known, and $\pi(\epsilon_r)$ is the prior density that contains the prior information available for unknown ϵ_r. The denominator is the marginal density of the measured data and plays the role of normalization constant. It is often ignored since it requires integration over all possible ϵ_r space. In the next step, we construct the likelihood and prior density terms and obtain the posterior density.

Let the joint prior model of the unknowns and noise be $\pi(E^{\text{scat}}, \epsilon_r, \xi)$. Using Bayes' theorem repeatedly, the joint distribution of all associated random variables can be decomposed as

$$\pi(E^{\text{scat}}, \epsilon_r, \xi) = \pi(E^{\text{scat}} \mid \epsilon_r, \xi)\pi(\xi \mid \epsilon_r)\pi(\epsilon_r)$$
$$= \pi(E^{\text{scat}}, \xi \mid \epsilon_r)\pi(\epsilon_r). \tag{10}$$

In the case that both ϵ_r and ξ are fixed, the measurement in the model (6) is completely specified, so the conditional density $\pi(E^{\text{scat}} \mid \epsilon_r, \xi)$ is formally given by

$$\pi(E^{\text{scat}} \mid \epsilon_r, \xi) = \delta(E^{\text{scat}} - \mathscr{F}(\epsilon_r) - \xi) \tag{11}$$

where δ is the Dirac delta distribution. Using (9)–(11), we get the likelihood model as

$$\pi(E^{\text{scat}} \mid \epsilon_r) = \int \pi(E^{\text{scat}}, \xi \mid \epsilon_r)d\xi$$
$$= \int \pi(E^{\text{scat}} \mid \epsilon_r, \xi)\pi(\xi \mid \epsilon_r)d\xi$$
$$= \int \delta(E^{\text{scat}} - \mathscr{F}(\epsilon_r) - \xi)\pi(\xi \mid \epsilon_r)d\xi$$
$$= \pi_{\xi\mid\epsilon_r}((E^{\text{scat}} - \mathscr{F}(\epsilon_r)) \mid \epsilon_r). \tag{12}$$

In the quite common case of mutually independent ϵ_r and ξ, we have $\pi_{\xi\mid\epsilon_r}(\xi \mid \epsilon_r) = \pi_\xi(\xi)$, where $\pi_\xi(\cdot)$ denotes the distribution of noise. Furthermore, if the noise is assumed to be additive Gaussian with zero mean and covariance matrix Γ_ξ, the likelihood density can be written as

$$\pi(E^{\text{scat}} \mid \epsilon_r) \propto \exp\left\{-\frac{1}{2}(E^{\text{scat}} - \mathscr{F}(\epsilon_r))^\top \Gamma_\xi^{-1} \right.$$
$$\left. \times (E^{\text{scat}} - \mathscr{F}(\epsilon_r))\right\} \tag{13}$$

where $(\cdot)^\top$ denotes the transpose operator. Furthermore

$$\pi(E^{\text{scat}} \mid \epsilon_r) \propto \exp\left\{-\frac{1}{2}(E^{\text{scat}} - \mathscr{F}(\epsilon_r))^\top L_\xi^\top L_\xi \right.$$
$$\left. \times (E^{\text{scat}} - \mathscr{F}(\epsilon_r))\right\} \tag{14}$$

which can then be written in the norm form as

$$\pi(E^{\text{scat}} \mid \epsilon_r) \propto \exp\left\{-\frac{1}{2}\|L_\xi(E^{\text{scat}} - \mathscr{F}(\epsilon_r))\|^2\right\} \tag{15}$$

where L_ξ is the Cholesky factor of the inverse of the noise covariance matrix. As a prior information, it is first assumed that the moisture variation is smooth inside the foam. Such an assumption can be encoded using a Gaussian density with mean η_{ϵ_r} and covariance Γ_{ϵ_r} as

$$\pi\left(\epsilon_r\right) \propto \exp\left\{-\frac{1}{2}\left(\epsilon_r - \eta_{\epsilon_r}\right)^\top \Gamma_{\epsilon_r}^{-1}\left(\epsilon_r - \eta_{\epsilon_r}\right)\right\}$$
$$= \exp\left\{-\frac{1}{2}\left\|L_{\epsilon_r}\left(\epsilon_r - \eta_{\epsilon_r}\right)\right\|^2\right\}. \tag{16}$$

Here, L_{ϵ_r} is the Cholesky factor of the inverse of the prior covariance matrix Γ_{ϵ_r}. The prior covariance matrix encodes the spatial smoothness knowledge of the unknowns. After multiplying the expressions in (15) and (16) and ignoring the normalization constant in (9), posterior density is obtained that contains the complete solution of the inverse problem in the Bayesian framework and can be expressed by point estimates. One of the most common point estimates in tomographic imaging problems is the *maximum a posteriori* (MAP). The MAP estimate can be computed from the posterior as

$$\widehat{\epsilon_{r_{\text{MAP}}}} = \arg\max_{\epsilon_r} \pi\left(\epsilon_r \mid E^{\text{scat}}\right). \tag{17}$$

This problem is equivalent to the minimization problem

$$\widehat{\epsilon_{r_{\text{MAP}}}} = \arg\min_{\epsilon_r}\left\{\left\|L_\xi\left(E^{\text{scat}} - \mathscr{F}(\epsilon_r)\right)\right\|^2 + \left\|L_{\epsilon_r}\left(\epsilon_r - \eta_{\epsilon_r}\right)\right\|^2\right\} \tag{18}$$

which is a regularized nonlinear least-square (LS) problem. In (18), the prior norm term acts as a regularization term, and it shares close links to generalized Tikhonov regularization. This minimization problem can be formally solved using the gradient-based optimization method. In the Newton-type method, the minimum point is found iteratively by linearizing the forward model, resulting in a linear LS solution in each iteration as

$$\epsilon_{r_{\ell+1}} = \epsilon_{r_\ell} + \alpha_\ell A^{-1} B \tag{19}$$

with

$$A = \left(J_\ell^T \Gamma_\xi^{-1} J_\ell + \Gamma_{\epsilon_r}^{-1}\right)$$
$$B = \left(J_\ell^T \Gamma_\xi^{-1}\left(E^{\text{scat}} - \mathscr{F}(\epsilon_{r_\ell})\right) - \Gamma_{\epsilon_r}^{-1}\left(\epsilon_{r_\ell} - \eta_{\epsilon_r}\right)\right)$$

where α_ℓ is the step length parameter, index ℓ is the iteration number, and J_ℓ is a Jacobian matrix (its derivation can be found in [33]), which is decomposed in real ($J_\mathbb{R}$) and imaginary ($J_\mathbb{I}$) parts as

$$J = \begin{bmatrix} J_\mathbb{R} & J_\mathbb{I} \\ -J_\mathbb{I} & J_\mathbb{R} \end{bmatrix}_{2S \times 2N_n}.$$

The approximate covariance of the posterior density Γ_{post} is given as

$$\Gamma_{\text{post}} = \left(J_\ell^T \Gamma_\xi^{-1} J_\ell + \Gamma_{\epsilon_r}^{-1}\right)^{-1}. \tag{20}$$

This approximate posterior indicates the uncertainty associated with the ill-posedness of the solution.

A. Noise Model

Let us denote the noise standard deviations (STD) of the real and imaginary parts of the complex-valued scattered electric field data to be $\sigma_\mathbb{R}$ and $\sigma_\mathbb{I}$, respectively. Under the assumption that noise between measurement points is independent and not correlated, the noise covariance is then given as

$$\Gamma_\xi = \begin{bmatrix} \sigma_\mathbb{R}^2 I_S & 0_S \\ 0_S & \sigma_\mathbb{I}^2 I_S \end{bmatrix} \tag{21}$$

where I_S is an $S \times S$ identity matrix and 0_S is an $S \times S$ zero matrix. In the case of real measurements, the noise covariance can be estimated by performing repeated measurements.

IV. PRIOR MODELING

In Section III, we defined the general expression for the prior density in (16). Since the unknown complex-valued dielectric constant is treated as a real-valued random variable, the prior density in (16) can be further expressed [34], [35] as

$$\pi\left(\begin{bmatrix} \epsilon_r' \\ \epsilon_r'' \end{bmatrix}\right) \propto \exp\left\{-\frac{1}{2}\begin{pmatrix} \epsilon_r' - \eta_{\epsilon_r'} \\ \epsilon_r'' - \eta_{\epsilon_r''} \end{pmatrix}^\top \begin{pmatrix} \Gamma_{\epsilon_r'} & \Gamma_{\epsilon_r'\epsilon_r''} \\ \Gamma_{\epsilon_r''\epsilon_r'} & \Gamma_{\epsilon_r''} \end{pmatrix}^{-1}\right.$$
$$\left. \times \begin{pmatrix} \epsilon_r' - \eta_{\epsilon_r'} \\ \epsilon_r'' - \eta_{\epsilon_r''} \end{pmatrix}\right\}. \tag{22}$$

The terms $\eta_{\epsilon_r'}$ and $\eta_{\epsilon_r''}$ denote the mean values of the real and imaginary parts of the dielectric constant, respectively. The matrices $\Gamma_{\epsilon_r'} \in R^{N_n \times N_n}$ and $\Gamma_{\epsilon_r''} \in R^{N_n \times N_n}$ are the marginal covariance matrices. $\Gamma_{\epsilon_r'\epsilon_r''} \in R^{N_n \times N_n}$ and $\Gamma_{\epsilon_r''\epsilon_r'} \in R^{N_n \times N_n}$ are the cross-covariance matrices of real and imaginary parts of dielectric constant, which embeds their correlation. The covariance $\Gamma_{\epsilon_r} \in R^{2N_n \times 2N_n}$, assumed to be a positive definite matrix, is given as

$$\Gamma_{\epsilon_r} = \begin{pmatrix} \Gamma_{\epsilon_r'} & \Gamma_{\epsilon_r'\epsilon_r''} \\ \Gamma_{\epsilon_r''\epsilon_r'} & \Gamma_{\epsilon_r''} \end{pmatrix}_{2N_n \times 2N_n}. \tag{23}$$

1) Uncorrelated Real and Imaginary Parts: If real and imaginary parts of the dielectric constant are treated as statistically uncorrelated, i.e., $\Gamma_{\epsilon_r'\epsilon_r''} = \Gamma_{\epsilon_r''\epsilon_r'} = 0$, then the prior covariance matrix can be written as

$$\Gamma_{\epsilon_r} = \begin{pmatrix} \Gamma_{\epsilon_r'} & 0_{N_n} \\ 0_{N_n} & \Gamma_{\epsilon_r''} \end{pmatrix}_{2N_n \times 2N_n} \tag{24}$$

where 0_{N_n} is an $N_n \times N_n$ zero matrix. The moisture field variation inside the foam is assumed to be smooth. Here, such a random field [36] can be generated using squared-exponential (SE) covariance function [37], which can account for the inhomogeneities. In general, the SE structure in 2-D is defined as

$$C_{ij} = \exp\left(-\frac{1}{2}\left(\frac{\|x_i - x_j\|^2}{c_x^2} + \frac{\|y_i - y_j\|^2}{c_y^2}\right)\right) \tag{25}$$

where c_x and c_y are characteristic length components and $i, j = 1, \ldots, N_n$. In practice, the characteristic lengths affect the moisture distribution (smoothness) in the x and y directions, respectively, Thus, (24) becomes

$$\Gamma_{\epsilon_r} = \begin{pmatrix} \sigma_{\epsilon_r'}^2 C & 0_{N_n} \\ 0_{N_n} & \sigma_{\epsilon_r''}^2 C \end{pmatrix}_{2N_n \times 2N_n} \tag{26}$$

where $\sigma_{\epsilon'_r}$ and $\sigma_{\epsilon''_r}$ are the standard deviations for the real and imaginary parts of the dielectric constant, respectively. These standard deviation values are multiplied with the SE covariance function, so as to control its overall amplitude variation. The values are chosen based on what knowledge of the unknown parameters is available prior to any measurements.

2) Correlated Real and Imaginary Parts: Consider that the real and imaginary parts of the dielectric constant are assumed statistically correlated. This implies that the cross-covariance terms $\Gamma_{\epsilon'_r \epsilon''_r} \neq 0$ and $\Gamma_{\epsilon''_r \epsilon'_r} \neq 0$ are required to form the covariance structure in (23). However, to find cross-variances matrices, dependence between the two random variables should be known. Herein, to establish the correlation between the random variables and form the prior covariance structure, we use sample-based densities.

In sample-based densities, we make use of a large set of previously/numerically obtained samples of the random variable in question. These datasets are known as samples. Assume that $\pi = \pi(\epsilon_r)$ is the probability density of a random variable ϵ_r, and we have a large database χ of size K and contain realizations of ϵ_r

$$\chi = \left\{ \begin{pmatrix} \epsilon'_r \\ \epsilon''_r \end{pmatrix}_1, \begin{pmatrix} \epsilon'_r \\ \epsilon''_r \end{pmatrix}_2, \begin{pmatrix} \epsilon'_r \\ \epsilon''_r \end{pmatrix}_3, \ldots, \begin{pmatrix} \epsilon'_r \\ \epsilon''_r \end{pmatrix}_K \right\} \quad (27)$$

where K is the total number of samples. The aim is to approximate $\pi(\epsilon_r)$ based on the χ. For this, we calculate the sample mean

$$\eta_{\epsilon_r} = \begin{pmatrix} \eta_{\epsilon'_r} \\ \eta_{\epsilon''_r} \end{pmatrix} \approx \frac{1}{K} \sum_{j=1}^{K} \begin{pmatrix} \epsilon'_r \\ \epsilon''_r \end{pmatrix}_j \quad (28)$$

and sample covariance

$$\Gamma_{\epsilon_r} \approx \frac{1}{K} \sum_{j=1}^{K} \begin{pmatrix} \epsilon'_r \\ \epsilon''_r \end{pmatrix}_j \begin{pmatrix} \epsilon'_r \\ \epsilon''_r \end{pmatrix}_j^T - \begin{pmatrix} \eta_{\epsilon'_r} \\ \eta_{\epsilon''_r} \end{pmatrix} \begin{pmatrix} \eta_{\epsilon'_r} \\ \eta_{\epsilon''_r} \end{pmatrix}^T. \quad (29)$$

The dielectric constant values for the samples are generated numerically using the data from the dielectric characterization of the polymer foam in the laboratory environment. In the dielectric characterization, a small cylindrical shape volume of the foam is characterized using a cavity perturbation technique at room temperature to obtain the complex dielectric value for different levels of moisture content. The developed dielectric measurement system is shown in Fig. 2. The foam sample is located in a quartz tube to have a stable position inside the cavity. Both sides of the cavity are terminated to a small iris of 10 mm width and the same height as the WR340 waveguides [38]. The moisture content is calculated based on the wet basis, that is,

$$M = \frac{W_m - W_d}{W_m} \times 100 \quad (30)$$

where M is the moisture percentage, W_m is the weight of the foam sample after adding the water, and W_d is the weight of the dry sample. At the first step, we obtained the dielectric constant associated with the 0% moisture level. Then, a certain amount of water is added manually, and the dielectric constant is recorded in each level. The real part of relative dielectric constant was found to be in the range of 1.164 and 3.255,
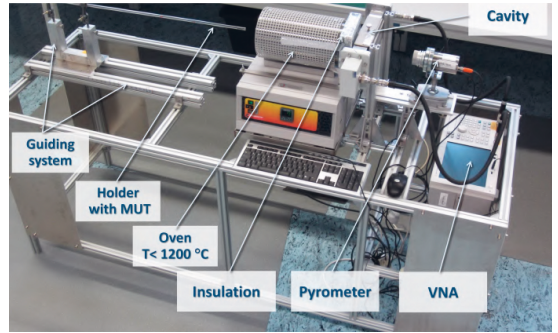

Fig. 2.　Experimental setup of the cavity-perturbation [38] method for dielectric characterization of the foam.

TABLE I
MATERIAL MODEL PARAMETERS

	$\bar{a}_\theta$	δ_{a_θ}	$\bar{b}_\theta$	δ_{b_θ}
ϵ'_r	1.085	0.01591	0.01256	0.00062
ϵ''_r	0.03021	0.0025	0.02249	0.0009

and the imaginary part varying between 0.017–0.276 for *wet basis* moisture content from 0% to 80%, respectively. After the characterization, the relationship between the *wet-basis* moisture content M_{meas} and its corresponding dielectric value is obtained using curve fitting and is given as [10], [39]

$$\theta = \bar{a}_\theta \exp\left(\bar{b}_\theta M_{\text{meas}}\right) \quad (31)$$

where $\theta = \{\epsilon'_r, \epsilon''_r\}$ denotes the material parameters. The values for the mean terms $\bar{a}_\theta$ and $\bar{b}_\theta$ are provided in Table I. The variables δ_{a_θ} and δ_{b_θ} are the standard deviation terms and denote the uncertainties in the curve fitting.

In order to create the dataset χ containing different moisture content realizations, the experimentally obtained mapping $M_{\text{meas}} \rightarrow \{\epsilon'_r, \epsilon''_r\}$ is applied. To generate simulated moisture samples, the uncertainties in the dielectric characterization is also considered, and hence, (31) is replaced as

$$\theta = a_\theta \exp\left(b_\theta M\right) \quad (32)$$

where a_θ and b_θ are random variables such that $a_\theta \sim \mathcal{U}(\bar{a}_\theta - \delta_{a_\theta}, \bar{a}_\theta + \delta_{a_\theta})$ and $b_\theta \sim \mathcal{U}(\bar{b}_\theta - \delta_{b_\theta}, \bar{b}_\theta + \delta_{b_\theta})$, where the variable are sample from the uniform distribution $\mathcal{U}$. Numerical values for δ_{a_θ} and δ_{b_θ} are given in Table I. The moisture content distribution in each sample M can be expressed as

$$M = M^* \mathbb{1} + \delta_M L Z \quad (33)$$

where $\mathbb{1}$ is an all-ones vector, M^* and δ_M are the mean and standard deviation of the moisture content field, respectively, L is the lower triangular matrix of the Cholesky factorization of the covariance C, and Z is a standard normal random vector.

Using (32) and (33), a dataset χ with $K = 5000$ random moisture samples is created. For each sample, moisture mean and standard deviation are chosen randomly. Also, the characteristic lengths in each sample were randomized.
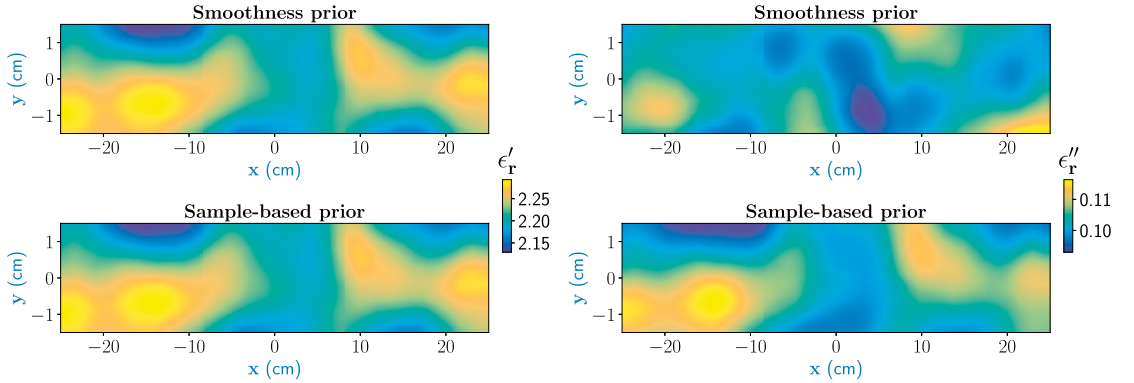
Fig. 3. Real (left) and imaginary (right) parts of the dielectric constant for samples drawn from uncorrelated smoothness and sample-based prior models.

Algorithm 1 Steps for Generating Samples for the Correlated Sample-Based Prior Model. Note That, to Ensure the Positive Definiteness for Matrix C, a Small Diagonal Component Is Added

1: $M^* \sim \mathcal{U}(0, 80)$ %, $\delta_M \sim \mathcal{U}(2, 20)$ %
2: $c_x \sim \mathcal{U}(x_{min}, x_{max})$, $c_y \sim \mathcal{U}(y_{min}, y_{max})$
3: Evaluate $C =$ Covariance(c_x, c_y, x, y) using (25)
4: $L =$ Cholesky(C)
5: $M = M^*$ ones$(N_n) + \delta_M L$ randn(N_n)
6: Calculate ϵ_r', ϵ_r'' using (32)

A pseudocode for generating a sample is given in the following, where the terms $x_{min} = 0$ cm, $x_{max} = 50$ cm, $y_{min} = 0$ cm, and $y_{max} = 3$ cm denote the minimum and maximum dimensions in the x and y directions of the foam domain, respectively.

Using the dataset, in which each sample is stacked in a vector form [see (8)], we calculated (28) and (29) using MATLAB built-in mean and covariance functions. The new prior covariance structure, from here on, is known as the sample-based prior model. The samples (or realization) from this prior density can be generated as

$$\epsilon_r = \eta_{\epsilon_r} + L_{\epsilon_r} Z. \qquad (34)$$

A randomized draw from the sample-based prior model is shown in Fig. 3 (right). Also, the same sample when we ignore the cross-covariance terms is shown in Fig. 3 (left). It is evident that, with the sample-based prior model, similar spatial variations are seen in the real and imaginary parts. However, with the neglected cross-covariance matrices, real and imaginary parts show different variations. In the next section, we present numerical examples that show how the choice of two priors affects the MAP estimation and overall estimation accuracy. It should be emphasized that, to evaluate the MAP estimate with uncorrelated parameters, we have used (26) instead of sample-based prior covariance with cross-covariance terms treated as zero.

V. NUMERICAL RESULTS

In this section, we evaluate the performance of the MAP estimates with the smoothness prior and sample-based prior for different moisture scenarios and levels. The imaging algorithm is tested with three cases where a high moisture distribution is tested in the first case. In the second case, it is assumed that moisture distribution is piecewise constant. For the third case, considering practical interest, the foam top surface geometry is assumed rough instead of the planar, and the moisture is modeled as a hot spot (has more moisture than the surrounding area). To generate the numerical measurement data from the MWT setup shown in Fig. 1, a finite element method (FEM)-based COMSOL simulation tool is chosen. The scattered electric field data are generated at a frequency of 8.3 GHz and stored in a matrix of size 12×12. Also, we added noise of 3% of the peak value of the numerical scattered field to the data. Note that the lower frequency point is chosen from X-band as it presents low degree of nonlinearity for the inverse scattering problem [40], [41] and computational efficiency.

As for the observation model $\mathscr{F}(\epsilon_r)$, we choose the method of moment (MoM) computation [42] with a pulse basis and point-matching testing function. For the MoM computation at 8.3 GHz, we assume that the imaging domain Ω_{foam} is discretized into 80×20 uniform rectangular pixels along the x and y directions, respectively. Here, the pixel size is chosen to be of size $\lambda/6$, so as to achieve sufficient numerical accuracy for the MoM solver (in comparison to the COMSOL solver). Thus, the total number of unknowns in the imaging domain, i.e., the real and imaginary part of the dielectric constant, for estimation becomes 3200. Note that a different solver is chosen for synthetic data generation to ignore "inverse crime," [12], i.e., the use of the same grid settings or numerical model for data generation and observation model. Otherwise, the same grid setting or the numerical model may potentially lead to a situation where severe modeling errors are ignored, hence giving a false impression on the accuracy of the estimates.

To calculate the MAP estimates with the smoothness prior, we set prior $\sigma_{\epsilon_r'} = 1$, and $\sigma_{\epsilon_r''} = 0.1$. The mean value η_{ϵ_r} in the prior is set to dielectric constant of the dry foam,
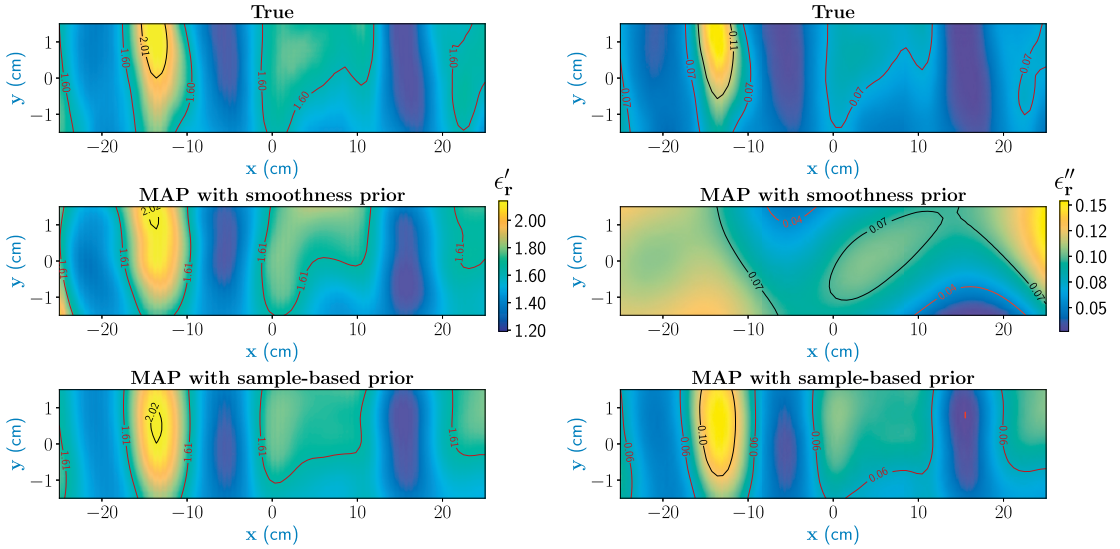
Fig. 4. High moisture case: MAP estimates with smoothness prior and sample-based prior model with real part (left) and imaginary part (right) of the dielectric constant. To highlight the dielectric constant values, contour is added.

i.e., $1.16 - j0.01$. For the sample-based prior, the prior covariance structure evaluated from the database is directly used to calculate the MAP estimates. For our simulation study, $\sigma_{\mathbb{R}}$ and $\sigma_{\mathbb{I}}$ are set to 3% of the peak value of the numerical scattered field data. To start the iteration, the value of ϵ_{r_0} is set to the dielectric constant of the dry foam, i.e., $\epsilon_{r_0} = 1.16 - 0.01i$ and $\alpha = 0.25$ are sets of all the reconstructions. The iterations are terminated, following the stopping criteria $Q(\epsilon_{r_{\ell+1}}) < Q(\epsilon_{r_\ell})$, where $Q(\epsilon_{r_\ell})$ is the norm term defined in (18). The reconstruction algorithm is implemented in MATLAB 2018b and takes approximately or less than 1 min per image. All computations were performed on a local computer with the configuration of 32 GB access memory, Intel Core(TM) i7-7820HQ central processing unit, and Nvidia Quadro M2200 graphics processing unit.

A. Smooth Moisture Variation

In the first set of experiments, numerical scattered electric field measurement data for a high moisture scenario are generated using (32) and (33). The MAP estimation with smoothness prior model and sample-based prior model is shown in Fig. 4. It can be seen that, with both the priors, the real part is estimated fairly well. However, the estimation of the imaginary part is much more accurate with the sample-based prior model with certain moisture regions being clearly indicated.

Post reconstruction, we also plotted the MAP estimate for a fixed value y = 0 cm along the cross section of the foam with ± 3 posterior standard deviation and compared it against the respective true cases for both the real and imaginary parts, as shown in Fig. 5. Especially, for the imaginary part, the uncertainty bound is higher when using just smoothness prior. However, this uncertainty bound is reduced for the case with

TABLE II
HIGH MOISTURE CASE

Prior	Smoothness		Sample-based	
Dielectric	ϵ_r'	ϵ_r''	ϵ_r'	ϵ_r''
RMSE (%)	1.84	31.91	1.79	8.21
RC	0.9752	0.3490	0.9771	0.9610

sample-based prior. To quantitatively evaluate the accuracy of the reconstruction, we compared the true and estimated profile by using root mean square error (RMSE) and resemblance coefficient (RC) performance metrics. The RC parameter is calculated as

$$RC_{\epsilon_r} = \frac{\int\int_{\Omega_{\text{foam}}} \overline{\epsilon_r^{\text{MAP}}} \overline{\epsilon_r^{\text{True}}} dxdy}{\sqrt{\int\int_{\Omega_{\text{foam}}} \left(\overline{\epsilon_r^{\text{MAP}}}\right)^2 dxdy}\sqrt{\int\int_{\Omega_{\text{foam}}} \left(\overline{\epsilon_r^{\text{True}}}\right)^2 dxdy}} \quad (35)$$

where $\overline{\epsilon_r^{\text{MAP}}} = \epsilon_r^{\text{MAP}} - \langle\epsilon_r^{\text{MAP}}\rangle$, $\overline{\epsilon_r^{\text{True}}} = \epsilon_r^{\text{True}} - \langle\epsilon_r^{\text{True}}\rangle$, and $\langle\cdot\rangle$ is the mean operator. For the RC, its values vary between 0 and 1. As the RC gets closer to 1, the MAP estimation is closer to the true profile. The RMSE and RC are calculated separately for the real and imaginary parts of the dielectric constant. Note that, to calculate these metrics, the number of pixels in the true profile is interpolated corresponding to the pixels in the estimated profile. The performance metric values for high moisture cases are shown in Table II. They are compared separately for the real and imaginary parts for the two prior models. It is clear from RC and RMSE values that the overall accuracy of the MAP estimate has improved with the sample-based prior model in both cases.
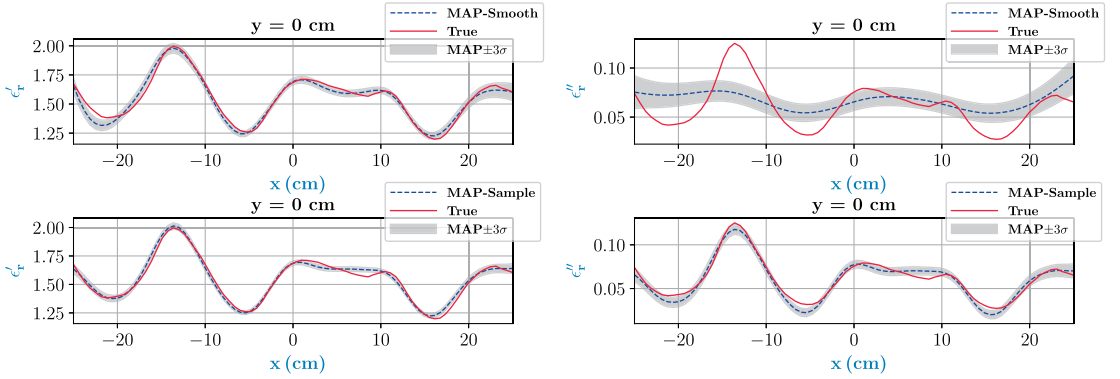
Fig. 5. Comparison between the true profile and MAP estimate for a high moisture case along the cross section of the foam y = 0 cm. The real part (left) and imaginary part (right) of the estimates are compared for smooth (top) and sample based prior (bottom), respectively. The light gray color denotes ±3 posterior standard deviation, denoted as σ.
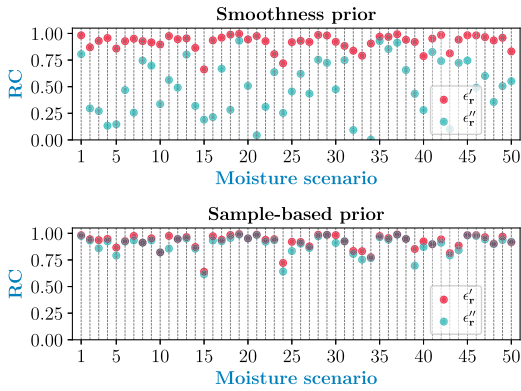

Fig. 6. Representation of RC evaluated for reconstructed distribution with smoothness prior (top) and sample-based prior (bottom) for 50 moisture scenarios. The vertical dashed lines indicate the serial number for the moisture scenario.

Furthermore, we also tested the two prior models on 50 different smoothly distributed moisture scenarios and evaluated the corresponding RC parameter, as shown in Fig. 6. Note that the RC metric is chosen for better representation purposes only. For most of the selected scenarios, significant improvement can be seen in RC with the sample-based prior model.

B. Piecewise Homogeneous Moisture Distribution

In this case, the moisture distribution is assumed piecewise homogeneous in the foam. The moisture area is given the value $\epsilon_{r_{\text{moisture}}} = 1.557 - j0.05$, and the rest of the foam is assumed dry with $\epsilon_{r_{\text{dry}}} = 1.16 - j0.01$. It should be emphasized that the primary goal is not to estimate the exact shape of the moisture area. This special case is taken considering practical interest where the moisture is sometimes located in bulk in one portion of the foam. Also, this case will test the generalization capabilities of the algorithm. As it breaks the smoothness assumption, which is otherwise present in the dataset of
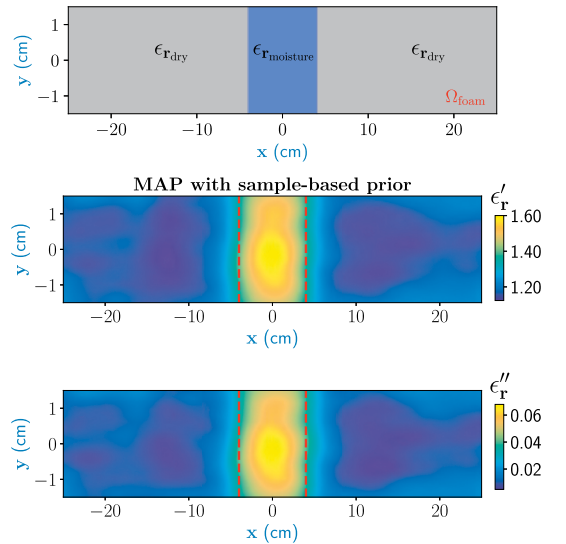

Fig. 7. MAP estimates for the piecewise homogeneous moisture scenario (top) with sample-based prior with real (middle) and imaginary parts (bottom) of the dielectric constant. The red dashed lines indicate the true boundary of the moisture profile.

samples used to build the sample-based prior covariance structure, the MAP estimates from the sample-based prior model are shown in Fig. 7 along with the true moisture distribution. We observe that both the estimated real and imaginary parts of the dielectric constant indicate the same presence of moisture and are well-estimated. This is also evident from the performance metrics shown in Table III. In the MAP estimates with smoothness-based prior, the imaginary part showed the wrong location of the moisture and hence not shown.

C. Random Rough Surface

So far, the foam with a planar surface is considered for moisture detection during an industrial process. However, it
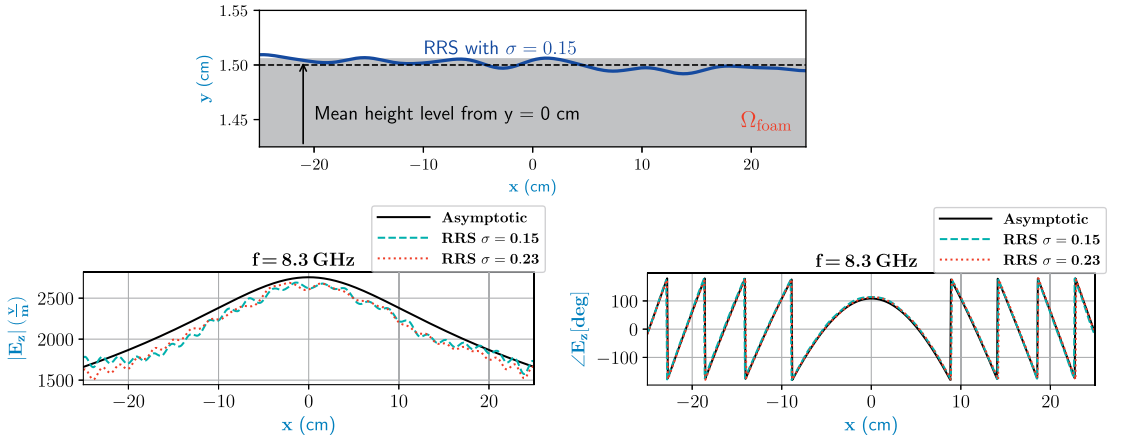
Fig. 8. Top figure shows the top surface of the foam with considered roughness and its mean height. Asymptotic electric fields magnitude (bottom left) and phase (bottom right) compared with the FEM results of a rough surface with an σ of 0.15 and 0.23 are probed at y = −0.5 cm and −25 cm ≤ x ≤ 25 cm with shown for the line source number 4 located at y = 11.5 cm.

TABLE III

PIECEWISE HOMOGENEOUS CASE

Prior	Smoothness		Sample-based	
Dielectric	ϵ'_r	ϵ''_r	ϵ'_r	ϵ''_r
RMSE (%)	5.2	67.82	4.0582	22.83
RC	0.9017	0.5637	0.9398	0.9362

has been observed that dielectric foam as a porous material can also have some uncertainty on the surface. In order to investigate the effect of the roughness of the surface, we consider a dielectric foam with a randomly rough surface (RRS) at the top. The random roughness is modeled [43] as follows:

$$y(x) = \sum_{m=-M}^{M} m^{-\beta} G_m \cos(2\pi m x + U_m) \quad (36)$$

where m is the integer number representing the spatial frequency, β denotes the spectral exponent, $G_m \sim \mathcal{N}(0, \sigma)$ is sampled from a Gaussian distribution, and $U_m \sim \mathcal{U}(0, 2\pi)$ is sampled from the uniform distribution. The random rough surface is characterized here by the following parameters: $\sigma = 0.15$ and $\beta = 0.8$. To obtain the scattered field, a hot-spot with 40% moisture ($1.3785 - j0.0432$) with radius 1 cm at position (15 cm, 0 cm) is considered inside the foam with permittivity $1.16 - j0.01$ and a moderate rough surface with mentioned parameters.

In Fig. 8, for one sample frequency, i.e., f = 8.3 GHz, the real and imaginary parts of the electric field of FEM and asymptotic fields are compared [44] for a dry foam with two different degrees of roughness. It should be noted, in order to obtain the asymptotic expression for the rough media, it is assumed that the fluctuation in the top surface is zero (i.e. root mean square (rms) height). Moreover, in the forward model, the top surface is given the average distance from each antennas to the top surface of the foam, i.e., $h = \langle h_i \rangle$ and

$i = 1, 2, \ldots, N/2$. The distance from the bottom antennas to the bottom surface of the foam is considered unique (has only one value). We observed that, in the MAP estimate, as shown in Fig. 9, with the smoothness prior, the imaginary part is indicating the presence of a strong artifact. However, in the estimated imaginary part with sample-based prior, strong presences of only one-hot spot is favorable. However, with both prior models, the shadow image due to the roughness of the surface is also visible.

VI. EXPERIMENTAL RESULTS

In this section, the sample-based prior model is tested on the scattering electric field data from our experimental MWT data for a wet-spot moisture case in a planar foam of size $50 \times 7.6 \times 75$ cm. The MWT experimental prototype shown in Fig. 10 consists of 12 WR90 open-ended waveguide antennas (with a VSWR 1.03 : 1). The distance of the top and bottom antenna to the top and bottom surface of the polymer foam is 8 cm, and the center-to-center distance between two adjacent antennas is 5 cm. The top and bottom antennas are resided in free-space from −12.5 cm to +12.5 cm along the x-axis. For data acquisition, antennas are connected to the Agilent N5224A vector network analyzer (VNA) via a P9164C 2×16 USB solid-state switch matrix with the maximum power level of 5 dBm. It should be noted that a waveguide calibration is performed to remove the unwanted reflections. Moreover, the MWT setup is surrounded by absorbers to increase the signal-to-noise ratio. Phase stable cables (offering phase stability of 3° at the maximum frequency) are used for the connections between the measurement devices and the antennas. Communication between the controlling computer, VNA, and the switch is provided using the Ethernet cable. The data acquisition process is entirely automated using MATLAB R2018b. For each foam sample, 12×12 data points (S-parameter measurements) were collected at 8.3 GHz using
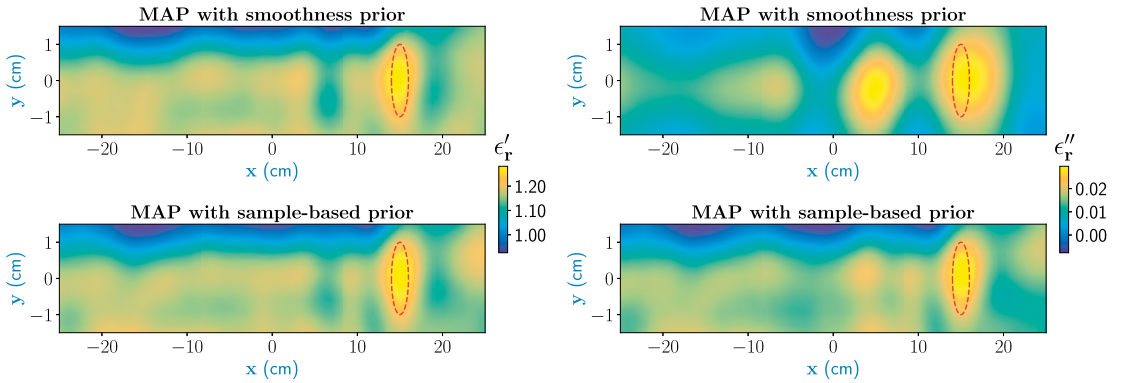
Fig. 9. Reconstructions with smoothness prior (first row) and sample-based prior (second row) of a hot-spot area embedded inside the foam with an assumed rough top surface with $\sigma = 0.15$.
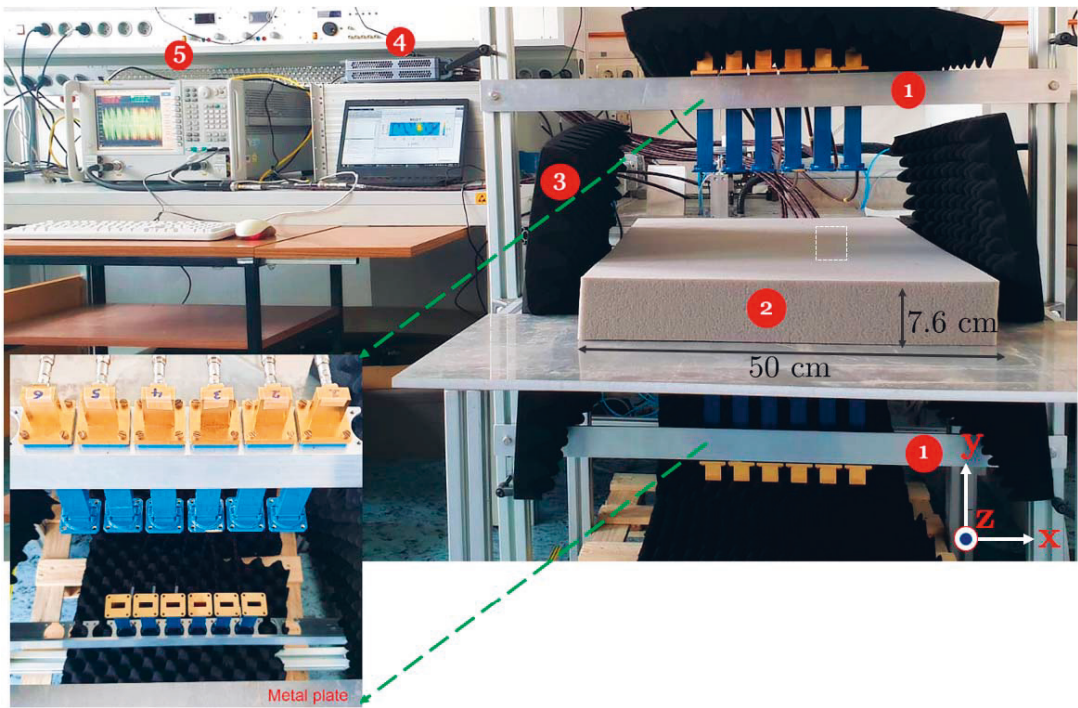

Fig. 10. Experimental setup of the MWT system prototype at the KIT Laboratory, Germany. The MWT system consists of X-band open-ended waveguide antennas as sensors and is indicated by number Tag 1. The alignments of the top and bottom antennas are shown in the bottom left by the green arrow, and the portion of the metal plate is removed to enable wave propagation between the top and bottom antennas. The polymer foam is shown by number Tag 2 and surrounded by absorbers, as shown by number Tag 3. The measurement data acquisition setup consists of the solid switch and VNA that are denoted by number Tags 4 and 5, respectively. The location plane of the test target is shown in right by white dash lines.

an IF bandwidth of 500 Hz. The approximate time for data acquisition was about 40 sec.

To create the wet-spot moisture target, a spherical foam of diameter 2.5 ± 0.1 cm and with 46% wet-basis moisture level ($\epsilon_r \approx 2.0 - 0.085i$) is chosen. An approximate location of the

target inside the foam is centered at $(-9$ cm, 1.55 cm, 0 cm$)$. We follow similar steps described in Section V to obtain the MAP estimates from the measurement data. Only the standard deviations of the measurement noise [see (21)] need to be changed and are calculated for 8.3 GHz frequency point
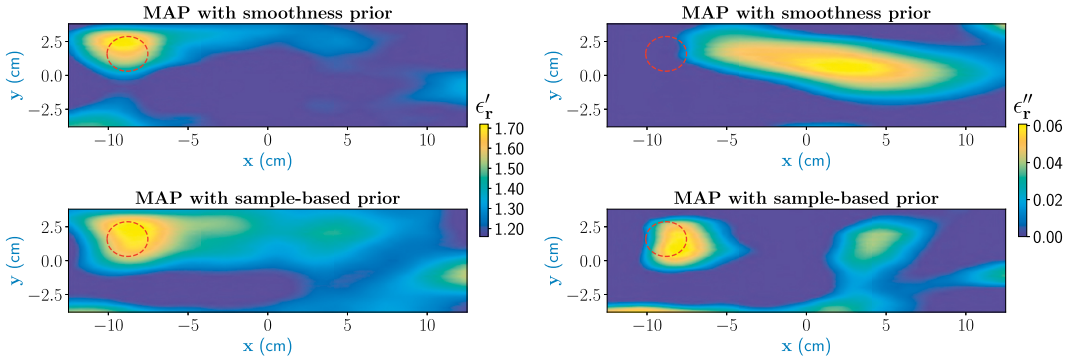
Fig. 11.   Reconstructions with smoothness prior (left) and sample-based prior (right) of a wet-spot area embedded inside the foam. The red dashed line indicates the true mean location of the target.

following the approach used in [45]. In the forward model, the antennas are modeled as line sources, and the electric field data E_{MoM} are converted to equivalent scattering matrix (in terms of S-parameter) S_{MoM} through calibration with respect to dry foam response $S_{\mathrm{scat_{dry}}}$ as

$$S_{\mathrm{MoM}} = \frac{S_{\mathrm{scat_{dry}}}}{E_{\mathrm{MoM_{dry}}}} \odot E_{\mathrm{MoM}}. \tag{37}$$

The MAP estimate with the smoothness prior and sample-based prior is shown in Fig. 11 for the selected x-y plane at z = 0 cm. With the smoothness model, the location of the target and its value are satisfactorily estimated in the real part. However, the imaginary part shows completely different spatial variations of the moisture distribution in the foam. With the sample-based prior, a significant improvement in the MAP estimation is observed. It is clear that, with this sample-based prior approach, the obtained MAP estimates offer a good reconstruction accuracy in comparison to the smoothness prior model.

VII. CONCLUSION AND DISCUSSION

In this work, we used microwave tomography to estimate the moisture distribution (as dielectric constant) in a polymer foam using the Bayesian inversion framework. The imaging modality will be integrated to derive intelligent control approach for an industrial microwave drying system. It is shown that, when real and imaginary parts are treated uncorrelated in the smoothness-based prior model, obtained dielectric values can be conflicting and incorrect i.e., there is some imbalance between the real and imaginary parts of the dielectric constant. Thus, we proposed a sample-based prior model to correctly reconstruct both the real and imaginary parts of the dielectric constant and the corresponding correlation between them. To construct the sample-based prior model, we use a large dataset consisting of simulated moisture samples to evaluate the prior mean and build the prior covariance structure. In each sample, moisture values are chosen based on the parametric model obtained from the dielectric characterization of the foam. The proposed approach is tested with 2-D numerical

microwave tomography data obtained in the X-band frequency for the considered moisture scenarios. The results presented show that a significant improvement in the estimation result is achieved with the sample-based prior model in comparison to the smoothness prior model. Also, two performance metrics, namely, the RC and RMSE, clearly highlight the effectiveness of the sample-based prior model on the reconstruction accuracy. Furthermore, the developed algorithm is tested on the MWT experimental prototype data. The results obtained with sample-based prior indicate that the estimated moisture distribution is very close to the true moisture scenarios considered in comparison to the smoothness prior.

We observed that the real and imaginary parts in the MAP estimation are slightly underestimated, which may be caused due to the modeling errors. Together with the source modeling error, this discrepancy might be caused due to the 2-D versus 3-D Green's function mismatch when the geometry of the target is no longer independent of the z-coordinates. In essence, these errors are very significant for the case when spherical geometries are assumed for the wet spots in comparison to infinite extended scatterer cases (where the general performance of the 2-D forward model with line sources is good). A detailed discussion was provided in [46] for medical imaging applications but is equally applicable for our application as well. Nonetheless, the source model errors remain persistent in our study. Thus, one way to improve the reconstructions is by using the Bayesian inversion approach in conjunction with the approximation error scheme [4], which can accommodate statistics of these errors resulting in better estimates. Therefore, a Bayesian approximation error [47] scheme will be employed to further improve the microwave tomography estimation. In the industrial drying system, the foam temperature will be higher than the room temperature at the exit. Therefore, dielectric characterization of the foam with wet-basis moisture levels at different temperatures is our next task. In this article, the real measurements are done with the static case where the influence of the conveyor belt is not considered. Therefore, future work will be related to doing dynamic measurements where the foam will be under

movement, and the estimated moisture information will be utilized in the feedforward loop of the intelligent control block of the industrial drying system. To further reduce the data acquisition time from MWT sensor setup and build fast controllers, limited-view MWT setup with statistical inversion framework has been in the testing phase.

ACKNOWLEDGMENT

REFERENCES

[1] J. A. T. Vasquez *et al.*, "Noninvasive inline food inspection via microwave imaging technology: An application example in the food industry," *IEEE Antennas Propag. Mag.*, vol. 62, no. 5, pp. 18–32, Oct. 2020.

[2] Z. Wu and H. Wang, "Microwave tomography for industrial process imaging: Example applications and experimental results," *IEEE Antennas Propag. Mag.*, vol. 59, no. 5, pp. 61–71, Oct. 2017.

[3] F. Becker *et al.*, "From visual spectrum to millimeter wave: A broad spectrum of solutions for food inspection," *IEEE Antennas Propag. Mag.*, vol. 62, no. 5, pp. 55–63, Oct. 2020.

[4] A. C. Metaxas and R. J. Meredith, "Industrial microwave heating," in *Power and Energy*. London, U.K.: Institution of Engineering and Technology, 1988. [Online]. Available: https://digital-library.theiet.org/content/books/po/pbpo004e

[5] Y. Sun, "Adaptive and intelligent temperature control of microwave heating systems with multiple sources," Ph.D. dissertation, KIT Dept. Elect. Eng. Inf. Technol., KIT Sci. Publishing, Karlsruhe, Germany, 2016.

[6] Y. V. Bykov, K. I. Rybakov, and V. E. Semenov, "High-temperature microwave processing of materials," *J. Phys. D, Appl. Phys.*, vol. 34, no. 13, pp. R55–R75, Jul. 2001, doi: 10.1088/0022-3727/34/13/201.

[7] G. Link and V. Ramopoulos, "Simple analytical approach for industrial microwave applicator design," *Chem. Eng. Process. Process Intensification*, vol. 125, pp. 334–342, Mar. 2018.

[8] M. Hosseini, A. Kaasinen, G. Link, T. Lähivaara, and M. Vauhkonen, "LQR control of moisture distribution in microwave drying process based on a finite element model of parabolic PDEs," *IFAC-PapersOnLine*, vol. 53, no. 2, pp. 11470–11476, 2020. [Online]. Available: https://www.sciencedirect.com/science/article/pii/S2405896320308879

[9] A. Omrani, R. Yadav, G. Link, T. Lähivaara, M. Vauhkonen, and J. Jelonnek, "An electromagnetic time-reversal imaging algorithm for moisture detection in polymer foam in an industrial microwave drying system," *Sensors*, vol. 21, no. 21, p. 7409, Nov. 2021. [Online]. Available: https://www.mdpi.com/1424-8220/21/21/7409

[10] R. Yadav, A. Omrani, G. Link, M. Vauhkonen, and T. Lähivaara, "Microwave tomography using neural networks for its application in an industrial microwave drying system," *Sensors*, vol. 21, no. 20, p. 6919, Oct. 2021. [Online]. Available: https://www.mdpi.com/1424-8220/21/20/6919

[11] A. Omrani, G. Link, and J. Jelonnek, "A multistatic uniform diffraction tomographic algorithm for real-time moisture detection," in *Proc. IEEE Asia–Pacific Microw. Conf. (APMC)*, Dec. 2020, pp. 437–439.

[12] J. Kaipio and E. Somersalo, *Statistical and Computational Inverse Problems*. Cham, Switzerland: Springer, 2005.

[13] M. K. Nguyen and A. Mohammad-Djafari, "Bayesian approach with the maximum entropy principle in image reconstruction from microwave scattered field data," *IEEE Trans. Med. Imag.*, vol. 13, no. 2, pp. 254–262, Jun. 1994.

[14] Y. Chen, J. Li, J. Zhuo, F. Han, and Q. H. Liu, "Fast multiparametric electromagnetic full-wave inversion via solving contracting scattering data equations optimized by the 3-D MRF model," *IEEE Trans. Microw. Theory Techn.*, vol. 68, no. 11, pp. 4515–4527, Nov. 2020.

[15] S. Caorsi, G. L. Gragnani, S. Medicina, M. Pastorino, and G. Zunino, "Microwave imaging based on a Markov random field model," *IEEE Trans. Antennas Propag.*, vol. 42, no. 3, pp. 293–303, Mar. 1994.

[16] R. Guo *et al.*, "Pixel- and model-based microwave inversion with supervised descent method for dielectric targets," *IEEE Trans. Antennas Propag.*, vol. 68, no. 12, pp. 8114–8126, Dec. 2020.

[17] R. Yadav, A. Omrani, M. Vauhkonen, G. Link, and T. Lahivaara, "Microwave tomography for moisture level estimation using Bayesian framework," in *Proc. 15th Eur. Conf. Antennas Propag. (EuCAP)*, Mar. 2021, pp. 1–5.

[18] A. Omrani, R. Yadav, G. Link, M. Vauhkonen, T. Lahivaara, and J. Jelonnek, "A combined microwave imaging algorithm for localization and moisture level estimation in multilayered media," in *Proc. 15th Eur. Conf. Antennas Propag. (EuCAP)*, Mar. 2021, pp. 1–5.

[19] G. Ferraiuolo and V. Pascazio, "The effect of modified Markov random fields on the local minima occurrence in microwave imaging," *IEEE Trans. Geosci. Remote Sens.*, vol. 41, no. 5, pp. 1043–1055, May 2003.

[20] R. Autieri, G. Ferraiuolo, and V. Pascazio, "Bayesian regularization in nonlinear imaging: Reconstructions from experimental data in nonlinearized microwave tomography," *IEEE Trans. Geosci. Remote Sens.*, vol. 49, no. 2, pp. 801–813, Feb. 2011.

[21] A. P. Dempster, N. M. Laird, and D. B. Rubin, "Maximum likelihood from incomplete data via the EM algorithm," *J. Roy. Statist. Soc., B Methodol.*, vol. 39, no. 1, pp. 1–38, 1977. [Online]. Available: http://www.jstor.org/stable/2984875

[22] M. A. Islam, A. Kiourti, and J. L. Volakis, "A novel method to mitigate real–imaginary image imbalance in microwave tomography," *IEEE Trans. Biomed. Eng.*, vol. 67, no. 5, pp. 1328–1337, May 2020.

[23] M. Ostadrahimi, P. Mojabi, A. Zakaria, J. LoVetri, and L. Shafai, "Enhancement of Gauss–Newton inversion method for biological tissue imaging," *IEEE Trans. Microw. Theory Techn.*, vol. 61, no. 9, pp. 3424–3434, Sep. 2013.

[24] P. Mojabi and J. LoVetri, "A prescaled multiplicative regularized Gauss–Newton inversion," *IEEE Trans. Antennas Propag.*, vol. 59, no. 8, pp. 2954–2963, Aug. 2011.

[25] R. Yadav, A. Omrani, M. Vauhkonen, G. Link, and T. Lähivaara, "Complex-permittivity estimation of a polymer foam using microwave tomography for the application of microwave drying," in *Proc. AMPERE 8th Int. Conf. Microw. High Freq. Appl.*, Sep. 2021, pp. 42–47.

[26] J. Richmond, "Scattering by a dielectric cylinder of arbitrary cross section shape," *IEEE Trans. Antennas Propag.*, vol. AP-13, no. 3, pp. 334–341, May 1965.

[27] S. Caorsi, G. L. Gragnani, and M. Pastorino, "Two-dimensional microwave imaging by a numerical inverse scattering solution," *IEEE Trans. Microw. Theory Techn.*, vol. 38, no. 8, pp. 980–981, Aug. 1990.

[28] N. Joachimowicz, C. Pichot, and J. P. Hugonin, "Inverse scattering: An iterative numerical method for electromagnetic imaging," *IEEE Trans. Antennas Propag.*, vol. 39, no. 12, pp. 1742–1753, Dec. 1991.

[29] X. Chen, *Computational Methods for Electromagnetic Inverse Scattering*. Singapore: Wiley, 2018.

[30] M. Ostadrahimi *et al.*, "Analysis of incident field modeling and incident/scattered field calibration techniques in microwave tomography," *IEEE Antennas Wireless Propag. Lett.*, vol. 10, pp. 900–903, 2011.

[31] M. Haynes and M. Moghaddam, "Multipole and S-parameter antenna and propagation model," *IEEE Trans. Antennas Propag.*, vol. 59, no. 1, pp. 225–235, Nov. 2011.

[32] D. Colton and R. Kress, *Inverse Acoustic and Electromagnetic Scattering Theory*. Berlin, Germany: Springer=, 1998.

[33] A. Franchois and C. Pichot, "Microwave imaging-complex permittivity reconstruction with a Levenberg–Marquardt method," *IEEE Trans. Antennas Propag.*, vol. 45, no. 2, pp. 203–215, Feb. 1997.

[34] S. M. Kay, *Fundamentals of Statistical Signal Processing: Estimation Theory*. Upper Saddle River, NJ, USA: Prentice-Hall, 1993.

[35] B. Picinbono, "Second-order complex random vectors and normal distributions," *IEEE Trans. Signal Process.*, vol. 44, no. 10, pp. 2637–2640, Oct. 1996.

[36] H. Rue and L. Held, *Gaussian Markov Random Fields: Theory and Applications (Monographs on Statistics and Applied Probability)*. London, U.K.: Chapman & Hall, 2005.

[37] C. Rasmussen and C. Williams, *Gaussian Processes for Machine Learning*. Cambridge, MA, USA: MIT Press, 2006.

[38] S. Soldatov, T. Kayser, G. Link, T. Seitz, S. Layer, and J. Jelonnek, "Microwave cavity perturbation technique for high-temperature dielectric measurements," in *IEEE MTT-S Int. Microw. Symp. Dig.*, Jun. 2013, pp. 1–4.

[39] T. Lahivaara, R. Yadav, G. Link, and M. Vauhkonen, "Estimation of moisture content distribution in porous foam using microwave tomography with neural networks," *IEEE Trans. Comput. Imag.*, vol. 6, pp. 1351–1361, 2020.

[40] O. M. Bucci, N. Cardace, L. Crocco, and T. Isernia, "Degree of nonlinearity and a new solution procedure in scalar two-dimensional inverse scattering problems," *J. Opt. Soc. Amer. A, Opt. Image Sci.*, vol. 18, no. 8, pp. 1832–1843, 2001.

[41] M. T. Bevacqua and T. Isernia, "An effective rewriting of the inverse scattering equations via Green's function decomposition," *IEEE Trans. Antennas Propag.*, vol. 69, no. 8, pp. 4883–4893, Aug. 2021.

[42] R. F. Harrington, *Field Computation by Moment Methods*. Hoboken, NJ, USA: Wiley, 1993.

[43] H.-O. Peitgen and D. Saupe, Eds., *The Science of Fractal Images*. Berlin, Germany: Springer, 1988.

[44] S. M. Moghadasi, M. Dehmollaian, and J. Rashed-Mohassel, "Time reversal imaging of deeply buried targets under moderately rough surfaces using approximate transmitted fields," *IEEE Trans. Geosci. Remote Sens.*, vol. 53, no. 7, pp. 3897–3905, Jul. 2015.

[45] C. Eyraud, A. Litman, A. Hérique, and W. Kofman, "Microwave imaging from experimental data within a Bayesian framework with realistic random noise," *Inverse Problems*, vol. 25, no. 2, Feb. 2009, Art. no. 024005, doi: 10.1088/0266-5611/25/2/024005.

[46] P. M. Meaney, K. D. Paulsen, S. D. Geimer, S. A. Haider, and M. W. Fanning, "Quantification of 3-D field effects during 2-D microwave imaging," *IEEE Trans. Biomed. Eng.*, vol. 49, no. 7, pp. 708–720, Jul. 2002.

[47] J. P. Kaipio, T. Huttunen, T. Luostari, T. Lähivaara, and P. B. Monk, "A Bayesian approach to improving the born approximation for inverse scattering with high-contrast materials," *Inverse Problems*, vol. 35, no. 8, Aug. 2019, Art. no. 084001, doi: 10.1088/1361-6420/ab15f3.

Rahul Yadav received the M.E. degree in electronics and communication engineering with a specialization in microwave engineering from the Birla Institute of Technology, Ranchi, India, in 2014. He is currently pursuing the Ph.D. degree with the Department of Applied Physics, University of Eastern Finland, Kuopio, Finland. His Ph.D. research involves the development of fast reconstruction algorithms for microwave tomography for industrial applications.

His research interests include computational electromagnetics and inverse problems.

Adel Omrani was born in Iran in 1991. He received the B.Sc. degree in electrical engineering from the University of Babol, Babol, Iran, in 2014, and the M.Sc. degree in electrical engineering from the University of Tehran, Tehran, Iran, in 2017. He is currently pursuing the Ph.D. degree in electrical engineering and information technology with the Karlsruhe Institute of Technology (KIT), Karlsruhe, Germany.

His current research interests include microwave imaging, antennas, numerical methods in electromagnetics, applied electromagnetic, and microwave engineering.

Guido Link received the Dipl.-Phys. and Dr.rer.nat. degrees in physics from the Technical University Karlsruhe, Karlsruhe, Germany, in 1990 and 1993, respectively. His diploma thesis and graduate research were devoted to the frequency and temperature-dependent dielectric characterization of low-loss ceramics and ionic crystals.

Since 1993, he has been working with the Karlsruhe Institute of Technology, Karlsruhe, in the field of high power microwave and millimeter-wave processing of materials as a Team Leader with the Institute for Pulsed Power and Microwave Technology. He authored or coauthored more than 200 contributed articles to international scientific conferences and more than 30 articles in scientific journals. He holds eight patents. His research interest includes dielectric measurements, design and simulation of microwave systems and processes, microwave-assisted sintering, curing of polymer composites, additive manufacturing, and plasma chemistry.

Marko Vauhkonen received the Ph.D. degree in physics from the University of Kuopio, Kuopio, Finland, in 1997.

He worked as a Researcher and Research Director with the University of Kuopio, until moving to Germany in 2006. He worked as a Marie-Curie Research Fellow for two years with Philips Research GmbH, Aachen, Germany. From 2008 to 2009, he worked as a CTO with a Spin-off Company Numcore Ltd. until starting as a Professor with the University of Kuopio (currently University of Eastern Finland), Department of Applied Physics, in 2009. He has published more than 100 scientific journal articles. His research interests include inverse problems, time-varying reconstruction, process tomography, and medical imaging, such as PET, SPECT, and MRI.

Timo Lähivaara received the M.Sc. degree from the University of Kuopio, Kuopio, Finland, in 2006, and the Ph.D. degree from the University of Eastern Finland, Kuopio, in 2010.

He is currently a Senior Researcher with the Department of Applied Physics, University of Eastern Finland. His research interests include computational wave problems and remote sensing.

Paper **III**

A. Omrani, R.Yadav, G. Link, T. Lähivaara,
M. Vauhkonen, and J. Jelonnek,
**"Multistatic Uniform Diffraction Tomography Derived
Structural-Prior in Bayesian Inversion Framework for
Microwave Tomography"**
IEEE Transactions on Computational Imaging,
2022, vol. 8, pp. 986-995.

RAHUL YADAV

In this thesis, microwave tomography (MWT) is applied for industrial process imaging related to microwave drying process. Specifically, algorithms based on the neural network approach and Bayesian inversion framework with correlated sample-based prior and structural prior are developed. The reconstruction algorithms are tested with simulated and experimental data from the developed MWT experimental sensor prototype. The developed methods can be extended for the applications of through-the-wall radar imaging, ground penetrating radar, and microwave based medical imaging.

UNIVERSITY OF
EASTERN FINLAND

uef.fi